

Electrically Thin Lenses and Reflectors

by

Miguel Ruphuy

A thesis
presented to the University of Waterloo
in fulfillment of the
thesis requirement for the degree of
Doctor of Philosophy
in
Electrical and Computer Engineering

Waterloo, Ontario, Canada, 2016

© Miguel Ruphuy 2016

I hereby declare that I am the sole author of this thesis. This is a true copy of the thesis, including any required final revisions, as accepted by my examiners.

I understand that my thesis may be made electronically available to the public.

Abstract

In physics, specially in optics, ray models are commonly used to simplify problems and further design devices for a diverse variety of applications. This diversity runs from mass-oriented products, such as cameras, to more sophisticated needs, such as wireless communications. Ray models frequently make use of Snell law to describe the rays' trajectories. Snell law is omnipresent practically in all optics applications; however, its applicability is limited to homogeneous half space.

Nowadays, advanced materials could further improve the characteristics of current devices and expand the applications by using inhomogeneous media. Designers and scientists typically avoid working with inhomogeneous media due to difficulties in predicting wave behaviour. In this thesis, I present a general and simple formulation to predict refraction from inhomogeneous electrically-thin media. This formulation can accurately describe refraction from inhomogeneous slabs just as Snell law predicts the refracted ray in a half space system.

Naturally, the first application that comes to mind are lenses used to form images and concentrate energy. Similarly, parabolic reflectors could potentially be substituted by inhomogeneous media devices with planar geometries. In this work, the models and concepts usually applied in optics are implemented and adjusted to electrically smaller devices for microwave applications. Based on ray models, an electrically-thin flat lens and reflector are introduced. The lens and reflector are designed to exhibit a refractive index gradient which results in a phase shift profile at the exiting face of the device. The concept of phase shifting to converge rays is validated with a case study at 10 GHz with a lens and a reflector having a diameter of 8λ . High contrast in the fields within the proximity of the focal point demonstrates the performance of the lens. Additionally, the lens has appreciably low spherical aberration. To obtain this characteristic, in the proposed design methodology, the electrical thinness of the lens is crucial. A complete analysis of monochromatic spherical aberration is performed and compared to classical gradient index rods.

Given the costly computation burden of large structures when using full-wave simulations, an analytic model is proposed to model 2D (constant refractive index in one direction) inhomogeneous electrically-thin media. For 3D lenses (radially varying refractive index in two dimensions), the analogous analytic model is developed using infinitesimal dipoles. This model exhibits good agreement with full-wave simulations and requires lower computation resources than that of numerical simulations.

In addition to lenses and reflectors, there are important applications for electrically-thin

inhomogeneous films. For instance, monostatic cloaking to conceal objects from radars is introduced here. An important decrease in the radar cross-section ratio is demonstrated.

Acknowledgements

I would like the opportunity to express my deepest gratitude to my supervisor Prof. Omar Ramahi. Before coming to Canada I probably sent about 200 emails enquiring about graduate studies and research opportunities all over the globe. From the few replies I received, Prof. Omar's was the most sincere, thoughtful and receptive of all. Sometimes your country of origin and many cultural differences are a barriers for many, this was not the case with Prof. Omar. He welcomed me to his research group and I always found the door open for numerous scientific, philosophic and even religious discussions which, I most say, helped me to develop myself not only as a professional but also as a person.

I am thankful to my committee members, Prof. Strickland, Prof. Mansour and Prof. Khandani. I have learned from all. In particular, Professor Strickland who opened the world of optics for me through Fourier Optics. Prof. Mansour who taught me microwave engineering, and Prof. Khandani who taught me information theory and was very kind for allowing me to use his computational facilities to accelerate my thesis work. Sincere thanks to all! Last, but not least, I am grateful to my external committee member Prof. Yablonovich for accepting the invitation to be the external examiner for my thesis defence.

I would also like to acknowledge my dear family. My mother who has always supported me in everything I do. A pillar in my everyday efforts to contribute to society. My father that no longer is physically here but his strong ethics will be a lesson that I will always carry close to my mind and heart. My sisters that always have been there for anything I need.

My warmest thanks to my wife who joined me in this adventure from the very beginning. I have definitely enjoyed and learned much more with her by my side.

Special thanks to my colleagues in our group for their friendship, support and discussions, Zhao Ren, Babak Alavikia, Mohammed AlShareef, Ali Albishi, Thamer Almoneef, Ahmed Ashoor, Abdulbased Ali, Faruk Erkmen, Mohamed El Badawi, Seyed Hossein, Mohammed Saeed, Maged Al-Dhaeebi, Abdulaziz Ali, Khawla Alzoubi, Humayra Naosaba, Hugo Sun, Li Li, Bing Hu, Vahid Nayyeri, Omar Siddiqui and many others who I had the opportunity to know.

Finally, thanks to the University of Costa Rica that financially supported me in this journey.

Dedication

To my supporting wife and parents. And to all people that are trying to make the world a better place.

Table of Contents

List of Tables	x
List of Figures	xi
1 Introduction	1
1.1 Motivation	1
1.2 Snell law	2
1.3 Background	6
1.4 Outline of the thesis	9
2 Law of refraction for inhomogeneous electrically-thin media	11
2.1 Introduction	11
2.2 Theory	12
2.3 Design for refraction at inhomogeneous electrically-thin media	13
2.4 Formulation: refraction from electrically-thin inhomogeneous media	15
2.5 Validation	18
2.6 Conclusion	21
3 Electrically-thin lenses and reflectors	22
3.1 Introduction	22
3.2 Flat lens	23

3.3	Flat reflector	28
3.4	Fabrication and experimental results	31
3.5	Electrically-thin lens and reflector for an enhanced dipole directivity	39
3.6	Conclusion	40
4	Analytical model of electrically-thin inhomogeneous media	42
4.1	Introduction	42
4.2	Theory	43
4.3	Model for 2D lenses and reflectors	46
4.4	Model for 3D lenses and reflectors	54
4.5	Conclusion	59
5	Spherical aberration in inhomogeneous lenses	60
5.1	Introduction	60
5.2	Classical gradient index rods	61
5.3	Spherical aberration	65
5.3.1	Optical path difference (OPD) analysis	68
5.3.2	Third-order aberration	70
5.4	Conclusions	75
6	Monostatic cloaking	76
6.1	Introduction	76
6.2	Design methodology	78
6.3	2D reflector	79
6.4	3D reflector	82
6.5	Conclusion	84
7	Conclusions	85
7.1	Contributions	85

8 Future directions	88
References	89
APPENDICES	100
A MATLAB Script to model the Electromagnetic fields of a flat 2D lens with infinite current lines	101

List of Tables

5.1	Optical Path Difference relationship with WAV_{RMS} and Energy percentage in the Airy disk[67]	68
-----	---	----

List of Figures

1.1	Boundary between two different media. An imaginary small rectangular frame is shown at a discontinuous interface on the left side of the figure and an imaginary thin pillbox at the interface is shown on the right side of the figure. \hat{n} is the normal unit vector (normal to the surface) and \hat{t} is the tangential unit vector.	3
1.2	Snell law. Incident ray reflecting and refracting from a homogeneous flat interface between two homogeneous media.	5
1.3	Snell law applied to electrically large convex lenses. Arrows represent localized wavefronts.	6
2.1	Understanding reflection using Huygens principle model (a). Refraction between two homogeneous half-space materials (b). Diagram of diffraction explained by Huygens principle (c).	13
2.2	Side view of an inhomogeneous refractive lens (a). Side view of an inhomogeneous refractive reflector (b).	15
2.3	Refraction in inhomogeneous media.	16
2.4	Study case. Schematic of a 30° angle refraction from a perpendicularly incident plane wave over a flat reflector.	19
2.5	Numerically simulated scattered electric field from a 4- λ reflector designed to produce 30° reflection.	20
2.6	Operation of the electrically-thin lens made of inhomogeneous slabs illuminated by a plane wave. Yellow lines represent the phase front of the wave and the brown arrows represent the direction of propagation.	20
3.1	Cross section view of the lens in the z=0 plane.	24

3.2	Cross section view of the lens in $x=0$ plane.	24
3.3	The refractive index profile along the radial direction for a lens with $d = \lambda_o/10$ and $4\lambda_o$ radius.	26
3.4	Magnitude of the total electric field over the $x=0$ plane. Color scale extends from -6.85 V/m (deep blue) to 6.85 V/m (deep red) (a). Magnitude of the z -directed Poynting vector over the $x=0$ plane. Color scale extends from 0 VA/m ² (green) to 0.202 VA/m ² (deep red) (b).	26
3.5	Magnitude of the normalized z -directed Poynting vector over the $z = 4\lambda_o$ plane.	27
3.6	Cross section view at the center of a classical paraboloid reflector (a). Cross section view of a flat focusing reflector proposed in this paper (b).	29
3.7	Cross section schematic of the reflector in the $x=0$ plane.	29
3.8	Magnitude of the scattered electric field over the $x=0$ plane. Color scale extends from -5.11 V/m (deep blue) to 5.11 V/m (deep red) (a). Magnitude of the z -directed Poynting vector over the $x=0$ plane. Color scale extends from 0 VA/m ² (green) to 0.239 VA/m ² (deep red) (b).	30
3.9	Relative permittivity for the electrically-thin flat lens as obtained from the design equation. Inset shows the absolute error (designed refractive index values minus dielectric used).	31
3.10	Magnitude of the simulated z -directed Poynting vector over the $y - z$ plane. Linear color scale extends from -0.00687 VA/m ² (deep blue) to 0.00687 VA/m ² (deep red).	32
3.11	Magnitude of the simulated x -directed total electric field over the $y - z$ plane for a 6λ 2D lens and a focal point designed at 9λ . Linear color scale extends from -1.91 V/m (deep blue) to 1.91 V/m (deep red).	33
3.12	Magnitude of the simulated z -directed Poynting vector over the focal point axis for a 6λ 2D lens and a focal point designed at 9λ	33
3.13	The 2D electrically-thin lens implemented by stacking dielectric layers (a). The lens placed in a Styrofoam frame (b).	34
3.14	Diagram of lens (a) and reflector (b) focusing experiment. The lens and reflector were framed using Styrofoam. In the case of the lens, an electrically-small sensor was placed on the back of the lens and a horn antenna was placed in front of the lens. In the case of the reflector, the horn antenna and the sensor were placed on the same side (front of the reflector).	36

3.15	Received power measurement system. The lens was framed with Styro-foam. On one side of the lens an electrically small sensor was placed over a plexiglass moving fixture for power sweeping. Over the other side of the lens, a signal generator with a horn antenna at an electrically-long distance provided plane wave illumination.	37
3.16	Normalized power of the electrically-thin flat lens across the focal point axis ($z = 9\lambda$, see Fig 3.2) obtained using simulation (green solid curve) and measurements (blue dash-dotted curve).	37
3.17	Relative permittivity for the electrically-thin flat reflector as obtained from the design equation. Inset shows the absolute error (designed refractive index values minus dielectric used).	38
3.18	Normalized power of the electrically-thin flat reflector across the focal point axis ($x = 4.1\lambda$) simulation (green solid curve) and measurements (blue dash-dotted curve).	38
3.19	Simulation results for the far field pattern of a dipole antenna (solid black curve), with an electrically-thin lens (dashed red curve) and an electrically-thin reflector (dash-dotted green curve).	39
4.1	Electrically-thin inhomogeneous slab illuminated by a plane wave (a). Infinite current line model (b).	47
4.2	Randomly chosen refractive index profile of the dielectric layers comprising a flat slab.	49
4.3	Two-dimensional distribution of the electric field on the right-hand-side of a 6λ inhomogeneous slab with a refractive index profile shown in figure 4.2 obtained using full-wave simulation (a), current line model without additional current line sources (b), and current line model with additional current line sources (c).	49
4.4	Refractive index design profile.	50
4.5	Two-dimensional distribution in the x-y plane of the electric field for a 6λ lens obtained using full-wave simulation (a) and the current line model (b).	51
4.6	One-dimensional distribution of the normalized magnitude and phase of the electric field for a 6λ lens along a line parallel to the x-axis and at $y=4\lambda$ obtained using full-wave simulation (solid line), current line model employing 60 line currents (dotted lines) and current line model employing 120 uniformly distributed line currents (dashed-dotted lines).	51

4.7	One-dimensional distribution of the normalized magnitude and phase of the electric field for a 6λ lens along a line parallel to the x-axis and at $z=4\lambda$, where $z=0$ is at the exiting side of the lens, for thickness of 1λ (a) and 2λ (b). Full-wave simulation (solid line), current line model employing 120 uniformly distributed line currents (dashed-dotted lines).	52
4.8	Off-axis flat reflector schematic.	53
4.9	Two-dimensional distribution of the scattered electric field from a 6λ off-axis reflector obtained using full-wave simulation (a) and the current line model (b).	54
4.10	Electrically-thin lens illuminated by a plane wave (a). Infinitesimally electric dipole model (dipoles are shown for the m^{th} layer only) (b).	55
4.11	One-dimensional distribution of the normalized magnitude and phase of the electric field for a 8λ lens along a line parallel to the x-axis and at $x=3.1\lambda$ obtained using full wave simulation (solid line), dipole model employing 903 dipoles (dotted lines) and dipole model employing 4515 dipoles (dashed-dotted lines).	57
4.12	The z-polarized electric field for an 8λ electrically-thin 3D lens in the xy plane obtained using full-wave simulation (a) and the 3D infinitesimal dipoles model (b).	58
4.13	Magnitude of the normalized z-directed Poynting vector over the $x = 4\lambda_0$ plane. Using full-wave simulation (a), and using the 3D infinitesimal dipoles model (b).	58
5.1	Gradient index (GRIN) lenses schematic.	63
5.2	Spherical aberration definition schematic.	65
5.3	Longitudinal and transverse aberrations.	66
5.4	Optical path difference (OPD) in spherical aberration. M is the marginal focal point and LA is the longitudinal aberration.	67
5.5	Normalized resolution schematic of Raileigh criterion. The individual images are depicted by the dashed orange lines. Solid blue line indicates the interference of the combined diffraction pattern. N.A. stands for Numerical Aperture and represents the ratio of the focal length over the diameter of the lens.	68

5.6	Solid line design of the refractive index for the electrically-thin lens, and dashed line the classical gradient index rod.	69
5.7	Cross section of the electric field (isoline format) of the electrically-thin lens. The lens wavefront is shown in solid lines and the reference spherical wavefront in dotted line.	71
5.8	Cross section of the electric field (isoline format) of the rod. The lens wavefront is shown in solid lines and the reference spherical wavefront in dotted line.	71
5.9	Optical path difference (OPD) as a function of the distance from the center of the lens. The solid line corresponds to the electrically-thin lens. The dashed line corresponds to the GRIN rod. (To extract the OPD, the phase in the proximity of the first zero phase wavefront immediately after the lens was computed from the numerical simulation. Since the discretized values were not exactly zero, the values were rounded and selected by a Matlab code that classified the rounded zero phase coordinates of every point on the zero phase wavefront.)	72
5.10	Y as a function of the longitudinal aberration (LA). Solid blue line corresponds to the electrically-thin lens. Dashed green line corresponds to the GRIN rod.	74
5.11	Third-order OPD with defocusing (a). Third order LA with defocusing (b). Solid blue line corresponds to the electrically-thin lens. Dashed green line corresponds to the GRIN rod. The plots were produced using the format used in [67].	74
6.1	Constructive interference for an angled-refracted exiting wave over the electrically-thin flat reflector.	79
6.2	Design of the refractive index profile for a 2D cloaking device. The linear refractive index profile was designed for $+/- 80^\circ$ angle refraction.	80
6.3	Scattered electric field for $+/- 80^\circ$ angle refraction design of a 2D reflector. The plane wave is polarized in the \hat{x} direction. Color scale extends from $-10.7 V/m$ (deep blue) to $10.7 V/m$ (deep red).	80
6.4	Poynting vector of the total field. The incident plane wave propagates from left to right. The left most arrows are almost perfectly horizontal. Although the scattered field is strong close to the reflector, the Poynting vector shows low reflections in the direction of the source.	81

6.5	Electrically-thin flat reflector schematic front view (a). Side view (b). . . .	82
6.6	Total electric field of a 10 GHz plane wave perpendicularly incident to a PEC object (Color scale extends from $-2.59 V/m$ (deep blue) to $2.59 V/m$ (deep red)) (a). Total electric field of a plane wave perpendicularly incident to an electrically-thin cloaking (reflector) device concealing a PEC object (Color scale extends from $-20.5 V/m$ (deep blue) to $20.5 V/m$ (deep red)) (b).	83
6.7	Monostatic radar cross section (RCS) of a PEC object with a cloaking device (solid blue line) and without a cloaking device (green dashed line).	84

Chapter 1

Introduction

1.1 Motivation

Tailoring electromagnetic (EM) waves at convenience is highly desired in applications like imaging systems, cloaking, energy concentrators for communication or even for energy harvesting, among others. Nowadays, there are variety of technologies available for such applications. Dielectric lenses, parabolic reflectors, prisms, metamaterials, and gradient index (GRIN) rods are some examples of devices used to reshape electromagnetic waves. Most of these technologies are based on Snell law to refract rays, or rely on phase discontinuities to bend the rays [1, 2, 3, 4]. In particular, commercially available devices for reshaping a wavefront into a focal point are typically bulky and heavy such as dielectric lenses and parabolic reflectors. Such devices involve complex geometrical designs. Parabolic reflectors, commonly used in high-gain radar and antenna applications, are expensive relative to the cost of the radar system. However, their transportation logistics are very expensive, especially for satellite applications.

Lenses have been used for centuries [5, 6]. Curved lenses are commonly used in optics to concentrate light onto a focal point. These curved lenses have been the subject of a myriad of studies and optimization processes that aim to decrease monochromatic aberrations [7, 8], which is a type of deformation of the image. Aberration is caused by the geometry of the lenses and its analysis is mostly based on ray path models. Blurred or distorted images are the main effect of aberrations.

Based on ray optics, designers use Snell law to follow the refraction paths of the rays to design and optimize curved lenses. The usefulness and importance of this millennial

law is not in doubt. Snell law applies to the case where a ray (or wave) travels from one homogeneous material to another through a flat interface, or locally flat interface. However, Snell law is not applicable to interfaces involving inhomogeneous media. An exception was made for GRIN rods but only due to the slowly varying index material. Therefore, GRIN rods had been considered locally homogeneous for design purposes [9]. Other formulations like the Generalized Snell law [2, 10] were proposed to explain refraction due to sudden phase jumps. However, this formulation does not apply to inhomogeneous media.

Besides the scientific curiosity behind developing a formulation for inhomogeneous media, there remains the question of whether focusing can be achieved by using inhomogeneous media and whether is it possible to predict refraction at a particular location from the known parameters of an inhomogeneous lens.

In this thesis, a formulation to predict refraction from electrically-thin inhomogeneous media is presented. The limitation of the electrical thinness comes from the coupling phenomena between adjacent materials as will be discussed later. An electrically-thin flat lens as well as a reflector are presented here as applications of the new formulation for refraction from inhomogeneous electrically-thin media. Furthermore, the lens is proven to have insignificant spherical aberration. An analytical formulation is also presented to help reduce design time for electrically-thin lenses and reflectors. In addition, a monostatic cloaking device is presented based on the same concept. In the following sections of this chapter an overview of previous research and outline of the thesis are presented.

1.2 Snell law

Snell law has been the foundation for prediction and designing lenses for centuries. Snell law originates from applying boundary conditions (BC) that require the continuity of the tangential field components. The boundary conditions are as important as Maxwell equations are to electromagnetic problem. Without them a problem cannot be defined completely and a unique solution cannot be obtained. In order to deal with problems effectively, understanding boundary conditions is essential. BCs are derived from the integral form of Maxwell equations, given that the differential form is suitable for continuous medium only. In order to find the boundary conditions of the tangential fields at the interface between two homogeneous materials, first, I recall Maxwell-Ampere law and Faraday's law given by

$$\oint_c \mathcal{H} \cdot d\mathbf{l} = \frac{d}{dt} \iint_S \mathcal{D} \cdot d\mathbf{S} + \iint_S \mathcal{J} \cdot d\mathbf{S} \quad (1.1)$$

$$\oint_c \mathcal{E} \cdot d\mathbf{l} = -\frac{d}{dt} \iint_S \mathcal{B} \cdot d\mathbf{S} - \iint_S \mathcal{M} \cdot d\mathbf{S} \quad (1.2)$$

where \mathcal{H} is the magnetic field intensity, \mathcal{D} is the electric flux density, \mathcal{J} is the electric current density, \mathcal{E} is the electric field intensity, \mathcal{B} is the magnetic flux density, and \mathcal{M} is the magnetic current density. An imaginary small rectangular frame can be constructed at the interface of two materials with one of its sides in medium n_1 and the other in medium n_2 (see figure 1.1). The length is Δl and the width is Δt which is considered vanishingly small ($\Delta t \rightarrow 0$). Calculating the line integral on the left side of equation 1.1 and considering that $\Delta t \rightarrow 0$, the boundary conditions are found as follows,

$$\hat{n} \times (\mathcal{H}_2 - \mathcal{H}_1) = \mathcal{J}_s \quad (1.3)$$

$$\hat{n} \times (\mathcal{E}_2 - \mathcal{E}_1) = -\mathcal{M}_s \quad (1.4)$$

where \mathcal{J}_s is the current surface density, \mathcal{M}_s is the magnetic surface density, the subscripts 1 and 2 corresponds to the fields at the materials n_1 and n_2 , respectively (on each side of the interface).

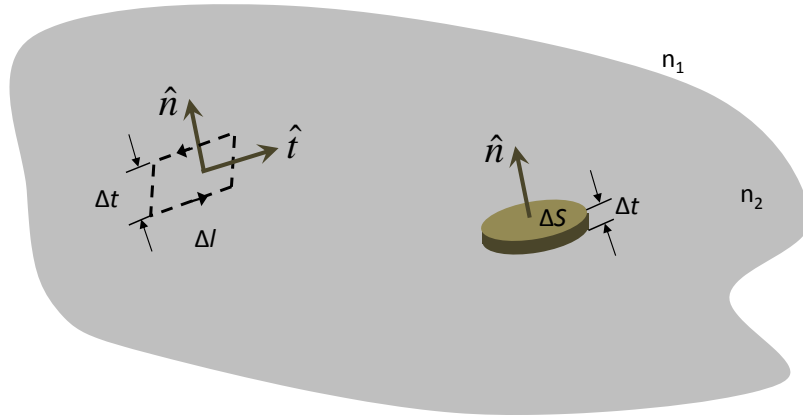


Figure 1.1: Boundary between two different media. An imaginary small rectangular frame is shown at a discontinuous interface on the left side of the figure and an imaginary thin pillbox at the interface is shown on the right side of the figure. \hat{n} is the normal unit vector (normal to the surface) and \hat{t} is the tangential unit vector.

Equations (1.3) and (1.4) show discontinuity in the tangential components of both electric and magnetic fields. However, as the magnetic current does not exist, the tangential component of the electric field is always continuous. Thus,

$$\hat{n} \times (\mathcal{E}_2 - \mathcal{E}_1) = 0 \quad (1.5)$$

In order to find the boundary conditions for the normal components, let's recall Gauss law

$$\oiint_S \mathcal{D} \cdot d\mathbf{S} = \iiint_V \rho_e dV \quad (1.6)$$

$$\oiint_S \mathcal{B} \cdot d\mathbf{S} = 0 \quad (1.7)$$

where ρ_e is the electric charge density. Similarly, applying Gauss law to a pillbox over a boundary where $\Delta t \rightarrow 0$ (see figure 1.1), the normal components are found as,

$$\hat{n} \cdot (\mathcal{D}_2 - \mathcal{D}_1) = \rho_{e,s} \quad (1.8)$$

$$\hat{n} \cdot (\mathcal{B}_2 - \mathcal{B}_1) = 0 \quad (1.9)$$

where $\rho_{e,s}$ is the surface electric charge density

In order to find Snell law a plane wave (or ray) illuminating an interface between two half-spaces with an arbitrary angle of incidence is considered. Notice that a wave can be modelled by rays propagating perpendicularly to the phase front of the wave. For illustration, the case of E-polarization where the incident field has an electric field component polarized in the x-direction is considered as shown in figure (1.2). The total tangential electric field on the left side of the interface equals the total tangential electric field on the right side of the interface, as dictated by equation (1.5). Therefore, the boundary condition leads to,

$$e^{-j\beta_1(y \sin \theta_i + z \cos \theta_i)} + R e^{-j\beta_1(y \sin \theta_r - z \cos \theta_r)} = T e^{-j\beta_2(y \sin \theta_t + z \cos \theta_t)} \quad (1.10)$$

where β_1 is the wavenumber in medium 1 (where the wave is coming from), β_2 is the wavenumber in medium 2 (to the right of the interface), θ_i is the incident angle of the ray, θ_r is the reflected angle of the ray, θ_t is the transmitted angle of the ray, R is the index of reflection, T is the index of transmission, y and z are values of the coordinate system. While equation (1.10) is valid only at the interface $z = 0$, the variable z is intentionally

kept in the equation for reasons that will become clear in Chapter 2. Matching the phase at $z = 0$ leads to,

$$\beta_1(y \sin \theta_i + z \cos \theta_i) = \beta_2(y \sin \theta_t + z \cos \theta_t) \quad (1.11)$$

which when enforced at $z = 0$ results in the statement of Snell law:

$$\beta_1 \sin \theta_i = \beta_2 \sin \theta_t \quad (1.12)$$

Note that in the case of lossy media only the real part of the wavenumbers is included for phase matching because the loss factors out on the phase exponential as attenuation. Therefore, there is no effect in the phase term.

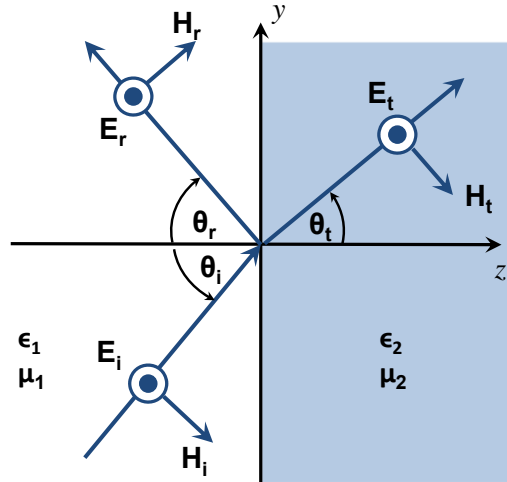


Figure 1.2: Snell law. Incident ray reflecting and refracting from a homogeneous flat interface between two homogeneous media.

It is worth noting that Snell law was derived considering an infinitely large interface. In other words, the formulation (equation (1.12)) is meant for a plane wave (which exists everywhere in space) and illuminates the infinite interface. From figure 1.2 it can be concluded that the flat interface leads to an invariant system in \hat{y} due to its homogeneity. Consequently, equation (1.12) is valid for any y . Evidently, the same equation is not applicable if one of the materials was inhomogeneous ($\epsilon(y)$ and/or $\mu(y)$) given that equation (1.12) has no dependence on y . Therefore, Snell law is valid for planar (locally flat) interfaces of homogeneous materials. In optics, a lens is locally flat (see figure 1.3)

because of its electrically large dimensions ($\lambda \ll D$), where D is the diameter of a lens and it is usually several orders of magnitude larger than the wavelength. As a result, the localized wavefronts at the interface of a lens impinge an approximately flat interface. For this reason, the local waves can still be modelled as rays in the optical regime. Hence, Snell law can be used for analysis, prediction and design of optical lenses.

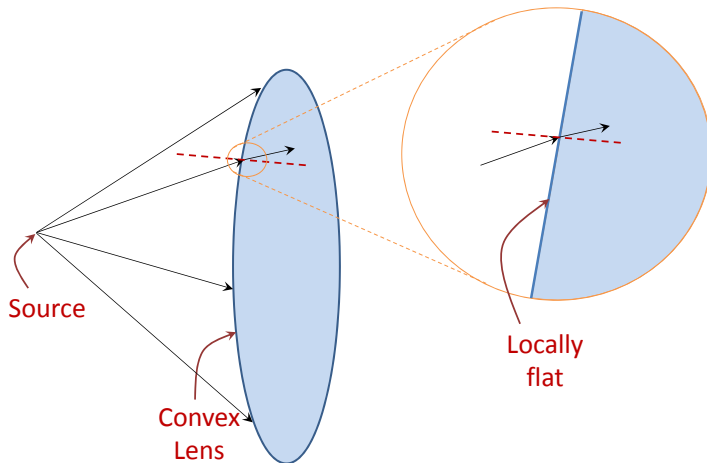


Figure 1.3: Snell law applied to electrically large convex lenses. Arrows represent localized wavefronts.

1.3 Background

Refraction, reflection and even diffraction are often used to form an image or reshape a wave. The desired quality of the image, power concentration, fabrication complexity, costs and application, all dictate which is the most convenient physics to be used. Market competitiveness has increased the expectation for smaller and more efficient devices. Reliability and transportability of devices are two features that typically have lower interest amongst engineers and scientists in general. Convex lenses and parabolic reflectors used nowadays have not evolved significantly over the past hundred years aside from refined fabrication processes and improved polishing techniques. Lenses, which have been the subject of fascination and study for centuries remain complex in shape requiring three-dimensional fabrication techniques. Convex and concave geometries result in images with aberration, which means that the images become blurry and distorted [7, 8]. Although, Snell law

and ray tracing analysis are used to decrease aberrations, the topic remains a challenge. Lenses, in general, are relatively very expensive to fabricate in comparison to the cost of an imaging system such as a camera or a telescope. Fresnel lens, which is a thinner version of convex lenses have been used to concentrate energy for solar applications and to collimate rays for light houses. This lens has the same properties of a convex lens, in terms of concentrating the rays; however, with the inconvenience of a more intricate geometry and losses related to such geometry [11, 12, 13, 14, 15, 16]. Parabolic reflectors, which are very common in high-gain radar and antenna applications, are relatively very inexpensive in comparison to the cost of the radar system, however, they are awkward and expensive to transport, especially for satellite applications. Another energy concentrator is the Fresnel zone plates. This plates make use of the interference phenomenon by reflecting part of the wave and letting the other part of the wave pass [17, 18, 19, 20]. At the focal point the half of the cycle that passed through the plates interfere constructively. However, the power of other half of the cycle is lost. In addition, the resulting image is aberrated. [17]

In an attempt to mitigate aberration in convex lenses, Pendry proposed a flat lens [21, 22, 23, 24, 25, 26, 27]. Unlike the classical lenses, Pendry's "perfect lens" use a negative refractive index metamaterial and a flat surface such that rays impinging refract rays with negative angle following Snell law. The unique property of Pendry lens is its ability to reconstruct not only the propagating harmonics but also the evanescent ones. Pendry's lens is able to reproduce the source's original travelling and evanescent spectra as long as the source is sufficiently electrically-close to the lens. Rudolph and Grbic [28] fabricated a 3D version of Pendry lens, thus overcoming the challenges that over a decade questioned its realizability. The major limitation of Pendry lens, nevertheless, is its inherent inability to work in the far field, requiring the source to be in the close proximity of the lens. This fundamental limitation precludes Pendry lens from imaging distant objects. Jacob et al. and Liu et al. [29, 30], introduced a new lens design concept referred to as a superlens, where the evanescent spatial harmonics are converted into propagating waves suitable for electrically-long transmission. The superlens is positioned at a close proximity of the source, thus making it more suitable for information transmission rather than imaging of electrically distant objects. Transformation optics had been introduced in recent years to bend electromagnetic fields using an anisotropic medium [31, 32, 33, 34]. However, the implementation of such designs becomes very restrictive and complex due to the requirements of artificial media having anisotropic properties. Additionally, the flat lenses designs using transformation optics are electrically thick.

In recent years, the interest in designing flat lenses has gained significant momentum. The advantages of a flat lens are fabrication cost and transportability. In [1, 2, 3], thin flat lenses were made of resonating metallic inclusions where very low aberration was

achieved. These flat lenses were based on creating a phase discontinuity through the use of resonant metallic inclusions. In this case, the classical Snell law is not applicable. For this reason, the generalized Snell law which is a formulation based on differential calculus and Snell law was introduced in [2]. According to this formulation, the phase jumps are responsible for refraction over the flat lenses. The authors in [2] subtract the phase term of two infinitesimally close paths and equates it to zero, the phase jump term allows the difference between two different paths to be zero. Impedance mismatch and resonance, both contributed to the low efficiency and narrow bandwidth, respectively. Others have used metamaterials with impedance matching layers [35]. However, the lenses are still limited by the resonance disadvantages including narrow bandwidth and losses.

In the 19th century, Maxwell, proposed a spherical gradient refractive index (GRIN) lens [36]. The resolution and quality of this lens continues to be debated [37]. In 1905, Wood presented the first design for a flat GRIN lens [9]. Wood’s flat electrically-thick lens bends rays through a gradient index material similar to the ray bending in the desert mirage phenomenon. Such a lens is subject to aberration due to high coupling between the different materials of the lens, which in turn causes image distortion. Wood’s design was based on several approximations and assumptions that constrain its applicability to sources and images very far from the lens, including the use of Snell’s law (locally) in a slowly varying inhomogeneous interface [9]. In recent years, advances in materials and fabrication techniques lead to a renewed interest in GRIN lenses [38, 39, 40, 41, 42, 43]. Metamaterial GRIN lenses were introduced using designs based on optics transformation resulting in anisotropic space-dependent permittivity and permeability material [31, 32, 33, 34, 44, 45]. Unlike most lenses, the design of this metamaterial lens is not based on Snell law, instead the design requires of a much more complicated calculation to find the characteristics of the lens. In addition, the implementation of such metamaterials is very restrictive due to design complexity and lens size. Although, discretization of the gradient index metamaterials to simplify the design has been proposed [46, 47], the anisotropy of the material and high losses represent an appreciable challenge. In [48], a gradient index metamaterial obtained by etching the dielectric around the SRRs at different depths was reported.

In summary, the most remarkable techniques used to reshape waves include positive and negative refractive index materials (Snell law), parabolic reflectors (reflection), phase discontinuities (generalized Snell law), anisotropic materials (transformation optics), Fresnel zone plates (diffraction) and slowly varying gradient index lenses (Snell law). In contrast to the physics used to design those devices, in this manuscript I propose a new formulation to predict refraction and design devices made of electrically-thin inhomogeneous media. The recent development of new materials and fabrication techniques allows to customize solutions to tailor electromagnetic waves at convenience. The most widely used, hence

attractive solution, are energy concentrators such as lenses and reflectors. In this work, I present electrically-thin lenses and reflectors based on refraction from inhomogeneous media. A simple design methodology is developed and validated through numerical examples and experimental work. In addition an analytical model is presented as a tool to verify and optimize designs time effectively with a significant reduction in time compared to numerical simulations. Furthermore, the lens is proven to have minimal spherical aberration. Besides the classical examples of lenses and reflectors to reshape waves, a monostatic cloaking device is designed and numerically validated.

1.4 Outline of the thesis

Chapter 1 consists of the introduction. The state of art for several design techniques, energy concentrators and lenses are presented. These techniques include refraction between homogeneous materials, reflection, diffraction, phase discontinuities and Optical Transformation. Given that this work presents a refraction formulation for inhomogeneous media, essential theoretical background material on Snell law was included.

In Chapter 2, Huygens principle is explained in detailed, including examples when applied to reflection, refraction and diffraction phenomena. Furthermore, the formulation for refraction at electrically-thin inhomogeneous slabs is derived and discussed based on Huygens principle model and boundary conditions. An example is shown to validate the law of refraction for inhomogeneous electrically-thin media at microwave frequencies.

Chapter 3 includes two application examples: an electrically-thin flat lens and a reflector at microwave frequencies. A design methodology is developed and reduced to a simple equation for the profile of the lens and reflector. Experimental results of 2D lenses and reflectors are presented. Also, far-field patterns are presented for the case when the lens and reflector operate as collimators.

In Chapter 4, an analytical model for the lens and reflector is introduced. This analytical model aims to reduce design's validation time. The model is compared to the full-wave numerical simulation that embodies all the electromagnetic phenomena.

In Chapter 5 a complete analysis and evaluation of the spherical monochromatic aberration of the electrically-thin flat lens is given. This lens is compared to the classical GRIN lens.

Chapter 6 includes an introduction to cloaking devices for microwave frequencies. A monostatic cloaking device is proposed. The device is presented as a module, such that it may be used repeatedly over large areas.

Finally, Chapters 7 and 8 present the contribution of the thesis and future research directions.

Chapter 2

Law of refraction for inhomogeneous electrically-thin media

2.1 Introduction

The most widely known law of refraction is Snell law. Recently a group [2] proposed the generalized Snell law based on Fermat principle, differential calculus and the conventional Snell law. The objective behind the generalized Snell law was to explain refraction from ultra-thin flat lenses made of metallic inclusions [2]. The classical formulation is based on phase matching to ensure the phase continuity, whereas the generalization pertained to the case of phase discontinuity along an interface created by the metallic resonant structures. Yu et al. [2] considered two infinitesimally close paths and equated the phase difference of those paths to zero. By following these the rays' trajectories, it was found that the distance between the rays at the interface lead to a gradient phase discontinuity.

Refraction, as will be shown in this chapter, can also be created by linear gradient index materials. This new formulation for refraction can be used to design new devices such as flat electrically-thin lenses and reflectors as will be shown in the next chapter. The refraction of a perpendicularly incident plane wave at a planar interface is physically explained through the phase advance of the rays within the medium. Huygens principle is then used to construct the refracted wavefront. The formulation is validated using numerical full-wave simulation for an example where the refractive angle is predicted with good accuracy. Furthermore, the formulation gives a physical insight to the phenomenon of refraction from electrically-thin inhomogeneous media.

2.2 Theory

In order to derive the formulation for inhomogeneous media, some wave propagation concepts are necessary. First, to characterize a wave, it is necessary to have an analytical model. One of the classical models to analytically characterize a wave is a plane wave. For example, an electric field propagating in the \hat{z} direction can be given by,

$$\mathbf{E} = \mathbf{E}_0 e^{j\omega t - \beta \cdot \mathbf{z}} \quad (2.1)$$

where \mathbf{E}_0 is the electric field vector, t corresponds to time, ω is the radian frequency, β is the wave vector and \mathbf{z} is the distance vector.

This equation gives fundamental information about the wave such as the wave velocity. Phase velocity is defined as the rate at which the phase of a wave propagates in a medium. In a dispersive material, the phase velocity for each frequency component travels at a different speed according to the refractive index of the corresponding frequency. The phase velocity is given by,

$$v_p = \frac{\omega}{\beta} \quad (2.2)$$

where ω is the frequency in radians and β is the wave number.

In 1678, Christiaan Huygens proposed that wave-fronts in light can be modeled using wavelets. A wave propagating in a medium is equivalent to allocating point sources along the wave-front and finding the contribution of all secondary spherical wave-fronts as they propagate outward. Each point source has an infinitesimal amplitude. The sources interfere forming a new wave-front formed by tangential lines joining equi-phase points of the wavelets' phase-fronts (see figure 2.1). The substitution of the wave-front can be performed by a step-by-step process, progressively advancing the phase and position of the wave. [49]

Figure 2.1(a) shows the reflection of a ray from a perfectly reflecting surface in terms of Huygens principle model. The ray is shown with arrows, whereas the incident phase-fronts are shown with blue lines. The reflected wave-front (green lines) is formed by a group of point sources' wavelets (orange spherical wave-fronts). Notice that different phase-fronts arrive at the reflecting surface at different times. For this reason the point sources at the surface have different phases. Figure 2.1(b) shows the refraction of rays in terms of Huygens principle over infinite half-planes of two different materials with refractive index n_1 and n_2 . The refracted wave is formed by a set of spherical wave-fronts originating at the interface.

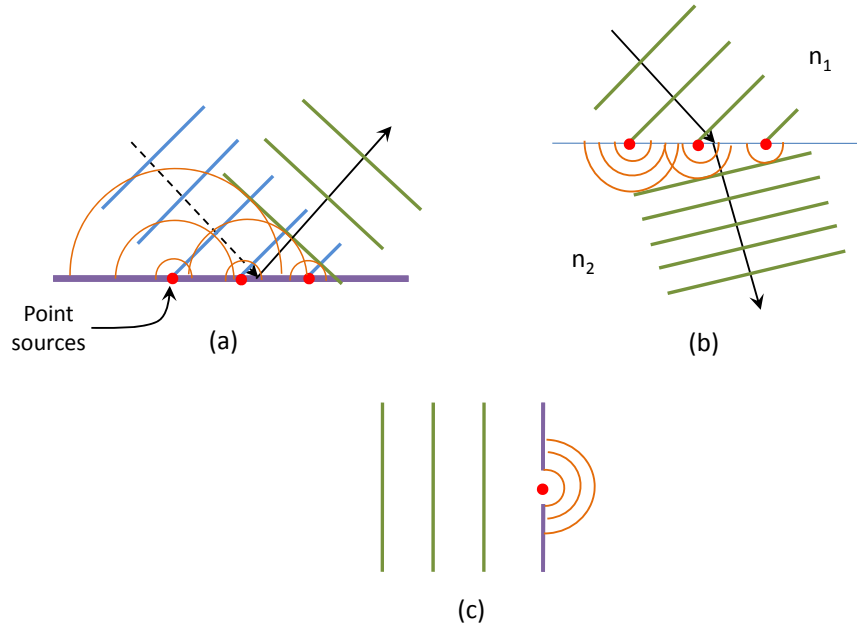


Figure 2.1: Understanding reflection using Huygens principle model (a). Refraction between two homogeneous half-space materials (b). Diagram of diffraction explained by Huygens principle (c).

Huygens principle can also be used to explain the phenomenon of diffraction. Diffraction is defined as the spreading of the wave due to an obstacle or when part of the wave is removed by an aperture [49]. Figure 2.1(c) shows the Huygens principle for diffraction.

2.3 Design for refraction at inhomogeneous electrically-thin media

In order to evaluate refraction from inhomogeneous electrically-thin materials, a design of a flat lens and reflector is proposed here. The lens is composed of slabs of different materials in two-dimensional space that refracts the wave with a specific angle. The reflector has additionally a perfect electric conductor in the back of the slabs. Figure 2.2 shows a thin slab of inhomogeneous material illuminated by a plane wave that is incident normally on the flat surfaces. The phase of the incident plane wave at the left side of the slab is uniform.

For the lens case, as the incident wave propagates through each layer, it experiences a phase shift proportional to the refractive index of each layer. These phase shifts translate into proportional delays in time domain. In other words, the peak of the wave exits different layers at different times. This phase difference is the one responsible to refract the incident wave. The same concept is used in the reflector except that the wave have to travel twice the distance within the media. Once when it is incident and once when it reflects back.

The slab depth (or thickness) d is considered to be much smaller than the wavelength ($d \ll \lambda$) of the incident field. This assumption implies minimal coupling between the dielectric layers, which indicates that the emerging incident field from each dielectric layer can be considered as an independent source in a manner similar to the application of Huygen's theory to the problem of scattering from electrically-small apertures.

To obtain an angled wave-front, the optical paths of all rays traversing the lens to a desired phase-front are equated. Notice that the phase-front is not unique but the angle the phase front makes with the y-axis is unique. This leads to

$$e^{-jk_M d - jh_M k_0} = e^{-jk_m d - jh_m k_0} \quad (2.3)$$

where k_0 is the wavenumber of vacuum, k_m is the wavenumber at the m^{th} layer, k_M is the wavenumber at the M-layer, d is the thickness of the lens, h_m is the distance from the m^{th} layer to the wavefront and h_M is the distance from the M-layer to the wavefront (see figure 2.2). The equation (2.3) may be simplified as follows,

$$n_M d + h_M n_0 = n_m d + h_m n_0 \quad (2.4)$$

where n_0 is the refractive index of vacuum, n_m is the refractive index of the m^{th} layer, and n_M is the refractive index of the M-layer.

In section 2.5, the scattered fields of a design following equation 2.4 will be compared to the refraction formulation for inhomogeneous media presented in the following section.

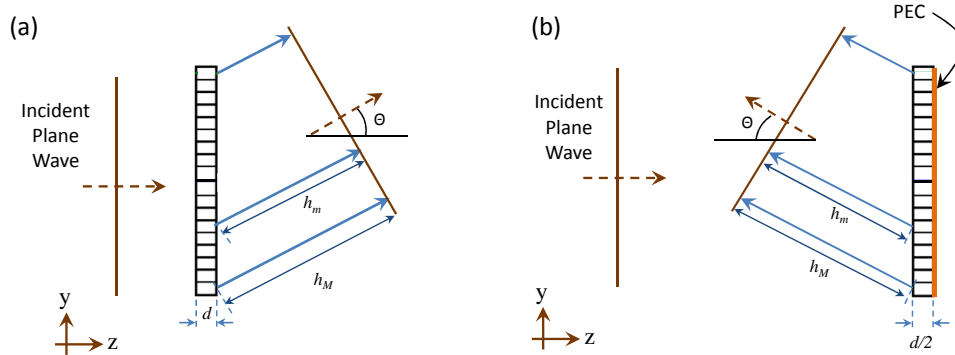


Figure 2.2: Side view of an inhomogeneous refractive lens (a). Side view of an inhomogeneous refractive reflector (b).

2.4 Formulation: refraction from electrically-thin inhomogeneous media

Snell law is a powerful formulation. However, the considerations mentioned in section 1.2 bound the designs to the classical two-media optical systems. Nowadays, the advances in material science provide an additional degree of freedom to alternative solutions. It is worth noticing that inhomogeneous materials has not been the greatest interest for electromagnetic applications in the past. Mainly because of its lack of simple formulations to predict its behaviour. Here, a simple formulation to predict such behaviour is presented.

Figure 2.3 shows the designed (see equation 2.4) lens highlighting the rays' trajectories as they propagate through the lens layers. Considering each individual ray, Snell law would predict a perpendicular outgoing ray. In ray theory, rays represent the direction of propagation which is perpendicular to the phase front of the plane waves. The dashed lines in figure 2.3 show a uniform phase front on the right side of the lens. Considering the first two slabs formed with ϵ_1 and ϵ_2 , it is clear that by the time the phase of the ray entering at $y_1, z = 0$ reaches $z = d$, the ray that entered at $y_2, z = 0$ has already exited the lens. In a gradient index material varying linearly with respect to y , the red dashed line would represent the phase front of a wave. Therefore, the ray or direction of propagation according to ray theory corresponds to a vector pointing perpendicularly to this phase front as shown in figure 2.3. The delay of a wave in one medium with respect to the other one results in an angled phase front that changes the direction of propagation. This steered ray is formed by constructive interference between rays emerging from each slab. Notice that each slab produces multiple rays in accordance with Huygens principle. Figure 2.3 highlights only

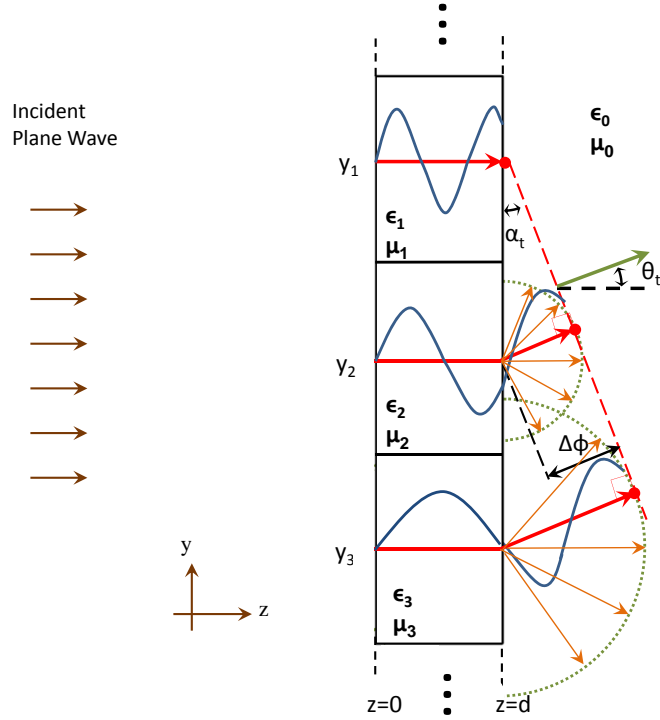


Figure 2.3: Refraction in inhomogeneous media.

the multiple rays emerging from the slab with material ϵ_2 . The phase front is constructed by tangentially joining equi-phase points of the spherically propagating point sources given by Huygens principle. This approximation holds for layers of electrically small height and width. The third layer (y_3) can be designed as well to provide the appropriate phase to achieve an angled phase front. In order for a wave to be discernible it requires that locally a few layers of material share identical gradient. The layers can then create a beam or wave refracting as a function of their gradient.

The formulation derived here phase matches the rays at layers y_1 and y_2 . Based on the boundary conditions previously discussed (section 1.2), equation (1.11) is rewritten here for convenience,

$$\beta_1(y \sin \theta_i + z \cos \theta_i) = \beta_2(y \sin \theta_t + z \cos \theta_t) \quad (2.5)$$

Considering y_1 as the reference (see Fig 2.3). Equation (2.5) is subsequently evaluated at $y = y_1$ and $z = d$,

$$\beta_1(y_1 \sin \theta_i + d \cos \theta_i) = \beta_0(y_1 \sin \theta_t + d \cos \theta_t) \quad (2.6)$$

where θ_i is the incident angle which is perpendicular to the second interface for the case presented in figure 2.3. Therefore, for both layers $\theta_i = 0$.

Typically, equation (2.6) would be simplified by setting $z = 0$ and generalized for all y . However, in this case, the same boundary conditions enforced at the second interface are formulated where z cannot be zero for all y because the phase of each ray would have propagated through the inhomogeneous slab of thickness d . Additionally, fields are dependent on y .

For the second layer (material ϵ_2) evaluating equation 2.5 at $y = y_2$ and $z = d$ gives

$$\beta_2(y_2 \sin \theta_i + d \cos \theta_i) = \beta_0(y_2 \sin \theta_t + d \cos \theta_t) \quad (2.7)$$

The left terms of equations (2.6) and (2.7) correspond to the phase of the rays at the right side of the respective slab. Comparing the left terms (left to the equal sign) of equations (2.6) and (2.7), it can be noticed that for $\theta_i = 0$ there is a difference in phase between them which can be represented as $\Delta\phi$ (see figure 2.3). Thus, for the rays to emerge from the right side of the lens and create a wavefront, the left term of equation (2.7) plus a phase difference $\Delta\phi$ need to equal the right term of equation (2.6):

$$\beta_2(y_2 \sin \theta_i + d \cos \theta_i) + \Delta\phi = \beta_0(y_1 \sin \theta_t + d \cos \theta_t) \quad (2.8)$$

$\Delta\phi = \beta_0(y_1 - y_2) \sin(\alpha_t)$ represents the desired (designed) phase difference between the two rays on the right side of the slab (see figure 2.3).

By comparing the right term of equations equation (2.6) and equation (2.8) it is clear that each term (left and right to the equal sign) are the same for both equations. Equating the left side of equations equation (2.6) and equation (2.8) and evaluating at $\theta_i = 0$ to account for the perpendicular incidence,

$$\beta_2 d + \beta_0(y_1 - y_2) \sin(90 - \theta_t) = \beta_1 d \quad (2.9)$$

where $\Delta\phi$ was substituted by $\beta_0(y_1 - y_2) \sin(\alpha_t)$ and $\alpha_t = 90 - \theta_t$ (see Fig 2.3). In the case of oblique incidence, each ray incident on a dielectric segment will have, at the lens entry point, a phase difference from a ray that is incident on the adjacent dielectric segment. The phase difference between the two rays at the entry plane (which is oblique to the plane of the incident wave) will translate into the same phase difference at the exit side of the lens unless the two dielectric segments have different dielectric constants. This is because

Huygens principle remains applicable irrespective of the wave incidence angle. Therefore, the formulation remains valid for oblique incidence. This specific formulation applies to a refracted wavefront having the angle θ_t as shown in figure 2.3. Also notice that each ray entering any slab will emerge from the right side in full accordance with Huygens principle. Only the rays that have the proper angle (dictated by the design equation) will contribute to a uniform phase front corresponding to that particular angle.

Unlike classical Snell law where the angle of incidence and the refractive index of the materials are sufficient to determine the refracted wave angle, here, additional parameters are required to predict the refracted wave (such as the distance between the center of the layers, thickness of the slab and refractive index of the materials). Additionally, the Snell law version for inhomogeneous media presented here includes dimension terms to account for the gradient of the refractive medium where the contrast and location of the refractive index among adjacent layers are important.

The extension to linear gradient index materials such that the relation between each adjacent material slabs leads to the same refractive angle is direct. The equation for such lens is given by (see Fig 2.3),

$$\beta_M d + \beta_0(y_m - y_M) \sin(90 - \theta_t) = \beta_m d \quad (2.10)$$

where β_M is chosen to be the reference and β_m is calculated for each m-th layer.

2.5 Validation

In order to validate the formulation, a case study is proposed in figure 2.4 where a 2D reflector (layers infinite in the y-direction) composed of 40-layers is designed to produce a 30° refracted wave. Each layer is chosen to be $\lambda/10$ height and the thickness $d/2 = \lambda/20$. The thickness is represented as $d/2$ because the wave propagates through the material two times, once when it is incident and once when it is reflected back.

Figure 2.5 shows the numerical solution of the scattered electric field given by the reflector. Both, the design and the Law of Refraction for inhomogeneous electrically-thin media (equation (2.10)) agree with the full wave simulation. All numerical simulations in this work were performed using CST MICROWAVE STUDIO ®(CST MWS) [50].

In the example shown previously, the design of the refractor was meant to redirect the plane wave to one fixed angle by varying linearly the refractive index (fixed gradient). The significance of such result leads to question whether it is possible or not to tailor the rays

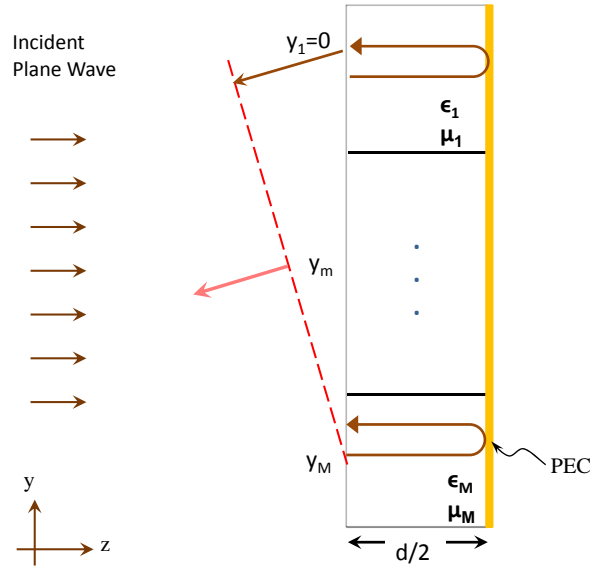


Figure 2.4: Study case. Schematic of a 30° angle refraction from a perpendicularly incident plane wave over a flat reflector.

to focus at one spot. In order to do so, the refractive gradient index must vary along the inhomogeneous media (variable gradient). Notice that locally every few slabs refract a ray that points towards the focal point (see Fig 2.6). The behaviour of such lens, could not be explained using Snell law locally or even the generalized Snell law.

In the next chapter a design methodology for an electrically-thin flat lens and reflector are proposed.

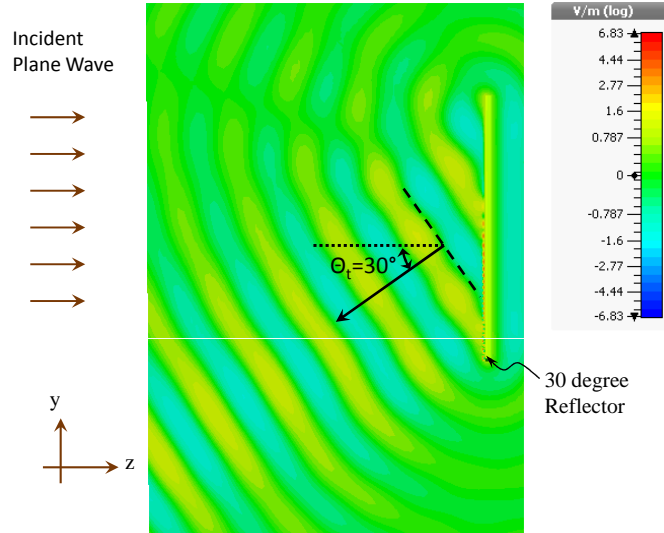


Figure 2.5: Numerically simulated scattered electric field from a $4\text{-}\lambda$ reflector designed to produce 30° reflection.

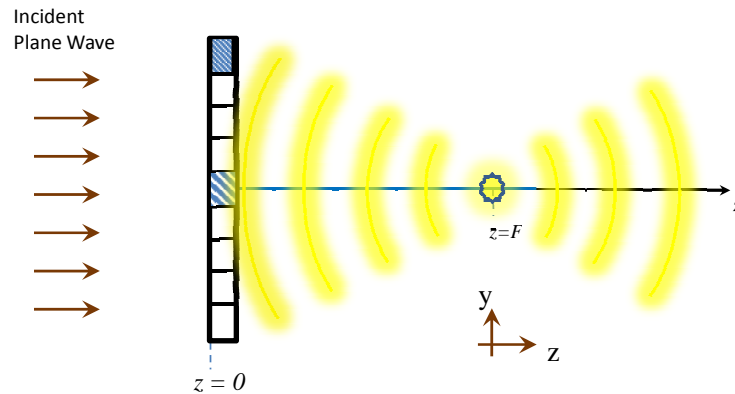


Figure 2.6: Operation of the electrically-thin lens made of inhomogeneous slabs illuminated by a plane wave. Yellow lines represent the phase front of the wave and the brown arrows represent the direction of propagation.

2.6 Conclusion

A new formulation to predict the refracted angles from electrically-thin lenses and reflectors was presented. In such lenses, Snell law cannot be used as it is applicable only when plane waves are incident on planar homogeneous slabs. In the case of electrically-thin inhomogeneous media, reflection and refraction analysis using plane waves cannot be applicable. By modeling the incident electromagnetic energy locally as a ray and invoking Huygens principle, a foundation for the generalization of refraction at inhomogeneous media is provided. The generalization presented in this chapter provides physical insight into refraction from electrically-thin inhomogeneous media that might appear as counterintuitive, particularly in the case of refraction with a specific angle from a flat reflector. An example to show the validity of this formulation and the compatibility of the ray model approach with full-wave numerical simulations embodying all physical interaction between waves and media were presented.

Chapter 3

Electrically-thin lenses and reflectors

3.1 Introduction

The focusing in a conventional convex lens is achieved by physically fabricating curved air-dielectric interfaces such that the incoming collimated rays are refracted towards the focal point of the lens. The interest in constructing a perfect lens perhaps dates back centuries ago when lenses were first invented or even possibly when the laws of refraction were first conceived [5, 6]. The definition of a perfect lens, in fact, remains elusive. Clearly, reflection, refraction, diffraction, coordinates transformation and resonance were all exploited in the quest for the ultimate focusing (see Section 1.3). In this work, theoretical findings are presented behind a focusing technique that is based on inhomogeneous media refraction. The designs here are limited to far-field focusing (i.e., focusing of an incident plane wave arriving from infinity onto a specific focal point in the proximity of the lens).

A flat lens design that provides focusing with no aberration is presented in this chapter. By profiling the refractive index of the lens to generate a converging spherical wavefront at the exit side of the lens, the transmitted fields concentrate at a specified focal point. Numerical examples show that focusing without aberration can be achieved at a specific frequency and that focusing is possible over a band of frequencies provided minimal dispersion. Additionally, the same principle used to design the lens can be used to design flat reflectors with a focal point.

The fabrication, testing, experimental setup and results of a 2D electrically-thin lens and reflector are presented in this chapter. Focusing at 9.45 GHz is demonstrated using a lens fabricated with commercially available dielectric materials. In addition to focusing,

the flat lens proposed here demonstrates relatively high power gain at the focal point. I also present a flat reflector based on the same concept. I believe that the proposed dielectric lens and reflector are strong candidates to replace heavy metallic dishes and reflectors used in a variety of applications especially satellites.

3.2 Flat lens

The flat lens proposed here consists of multiple concentric annular rings with a radial refractive index profile (see figure 3.1). The refractive index can be realized using a dielectric or magneto-dielectric material [51, 52]. Consider figure 3.2 where the lens is positioned in the $x - y$ plane. A plane wave is assumed incident on the lens from the left hand side with a propagation vector in the $+z$ direction. The incident plane wave propagates parallel to the normal of the lens with a uniform phase front at $z=0$. To achieve focusing, i.e., ray convergence at a specified focal point, labeled as F in figure 3.2, the two ray trajectories ABF and CDF are required to have equivalent optical paths. In other words, the two rays impinging on A and C must experience identical phase shift from the instant they enter the plate ($z=0$) to the instant they arrive at F such that the interference of the rays be constructive (see figure 3.2). Notice that the propagation vector of the incident wave is in the $+z$ direction which is parallel to the boundaries of the dielectric rings, while the exiting rays propagate towards the focal point.

Continuing on with the ray model for the incident plane wave, each ray traveling through each ring experiences a phase shift of $n_m k_0 d$, where n_m is the refractive index of the m^{th} ring given by $\sqrt{\epsilon_m \mu_m}$ and k_0 is the free space wave number. m designates the ring number starting with $m=1$ corresponding to the center disk at $x=y=z=0$ and finalizing with $m=M$ corresponding to the outermost ring (see figure 3.1). Setting the phase shift of the two paths ABF and CDF to be identical gives:

$$n_1 k_0 d + k_0 F = n_m k_0 d + k_0 h_m \quad (3.1)$$

where h_m is the distance from the focal point to the middle of the m^{th} ring (see figure 3.2).

The first term in equation (3.1) is the phase shift the incident wave experiences as it travels across the center ring and through free space to the focal point F . The second term corresponds to the phase shift across the m^{th} ring and to the focal point.

Eliminating k_0 from both sides of equation (3.1), it becomes,

$$n_1 d + F = n_m d + h_m \quad (3.2)$$

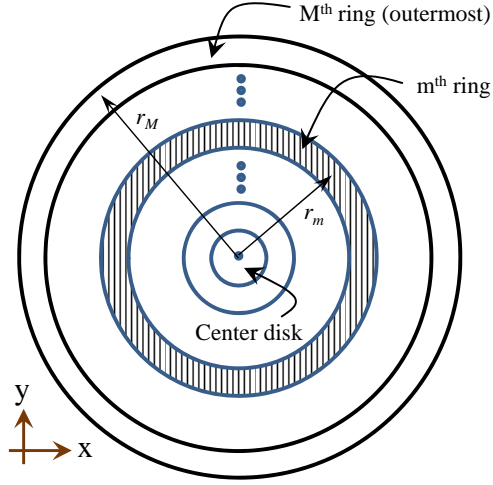


Figure 3.1: Cross section view of the lens in the $z=0$ plane.

which gives the design equation for n_m in terms of n_1 or vice versa.

By selecting the refractive index of any of the M-ring, the refractive index of all other rings is fixed via equation (3.2). Expressed in terms of the angle α_m ,

$$n_1 = n_m + \frac{F}{d} \left(\frac{1}{\cos(\alpha_m)} - 1 \right) \quad (3.3)$$

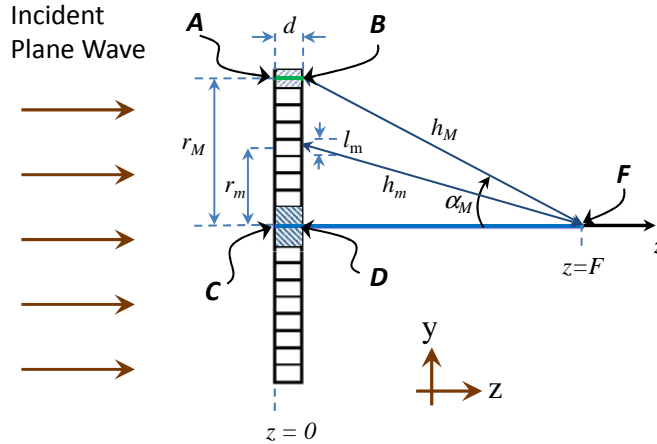


Figure 3.2: Cross section view of the lens in the $x=0$ plane.

Once n_M and n_1 are fixed, the refractive indexes of the remaining rings will be selected according to equation (3.3). The number of rings M will only dictate the resolution of the lens.

If the dielectric material used has low dependence on frequency, at least over a specific frequency range, equation (3.3), similarly, will have low dependence on the frequency over the same frequency range.

In earlier works [35, 53, 54], it was demonstrated that a gradient index microwave lens can increase the gain of horn antennas by focusing the beam. In fact, equation (9) of [54] reduces to equation (3.3) above. It is interesting that reference [54] arrived at this equation using a different approach involving differential calculus, whereas the derivation here was based on convergence of rays and equivalence of optical paths. It is worth noticing that in equation (9) of [54], the authors do not consider multiple reflections inside the lens. Their thick lens creates actual cavities which generates modes and unpredicted behaviors. Additionally, there is a coupling effect between adjacent layers which is not negligible for lenses comparable or thicker than a wavelength as the case presented in [54]. In this chapter, however, the derivation was based on building an electrically-thin lens. This design criteria allows to assume reasonably that the waves at each layer are confined and will not reflect on the interface between layers, thus achieving zero monochromatic aberration, characteristic that could not be achieved with the methodology in [54]. Furthermore, to account for the diffraction given by the lens edges, the refractive index at layer M is chosen equal to be 1 ($n_M = 1$). This means that vacuum is actually accounted as a layer.

To test the validity of equation (3.2), consider as an example, a lens with a radius and focal length of $4\lambda_0$. These two parameters are considered as the primary design parameters. The remaining lens parameters such as the thickness of the lens, d , the width of the dielectric rings, l_m and the lens dielectric medium parameters, can all be chosen with some flexibility. To start, the lens depth d needs to be electrically small in order to preserve the ray-like behavior of the incident field as it penetrates the lens. For the example chosen here, $d = \lambda_0/10$, where λ_0 is the free-space wavelength. Figure 3.3 shows the calculated refractive index profile along the y axis (or the radial) of the $\lambda_0/10$ thick lens for three different focal lengths.

Notice that the design equation provide a degree of flexibility in terms of the profile of the refractive index and also the selection for the relative permittivity and permeability for each annular ring. In fact, such flexibility allow for choosing the permeability and permittivity equal to achieve impedance matching for the incident wave and eliminate reflections which in turn helps increase the focusing efficiency considerably. This design flexibility that allows for the possibility of impedance matching can be viewed as a contrast

to previous flat lens designs that necessitated the use of thin film to minimize reflections which in turn confine the lens operation to a narrow frequency band.

Full-wave electromagnetic simulation tool CST was used to simulate the performance of the lens. Figure 3.4 (a) shows the total electric field magnitude distribution over the

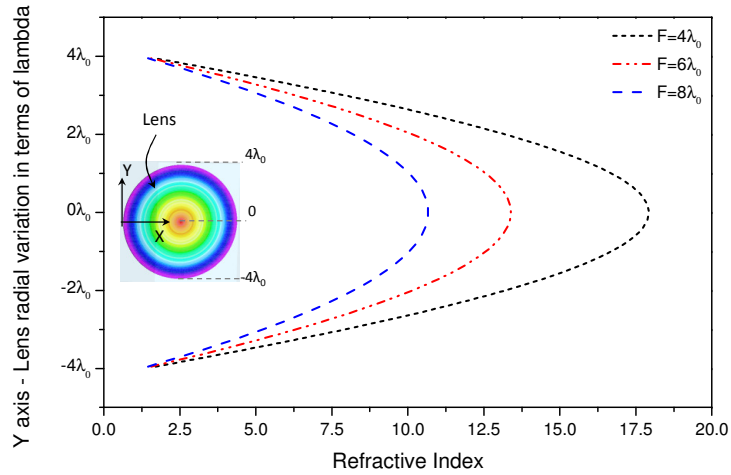


Figure 3.3: The refractive index profile along the radial direction for a lens with $d = \lambda_o/10$ and $4\lambda_o$ radius.

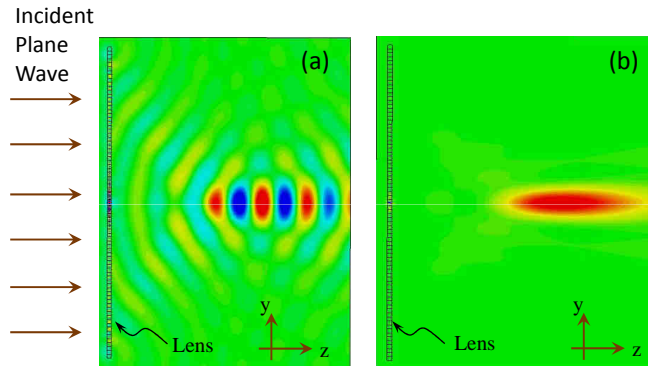


Figure 3.4: Magnitude of the total electric field over the $x=0$ plane. Color scale extends from -6.85 V/m (deep blue) to 6.85 V/m (deep red) (a). Magnitude of the z -directed Poynting vector over the $x=0$ plane. Color scale extends from 0 VA/m^2 (green) to 0.202 VA/m^2 (deep red) (b).

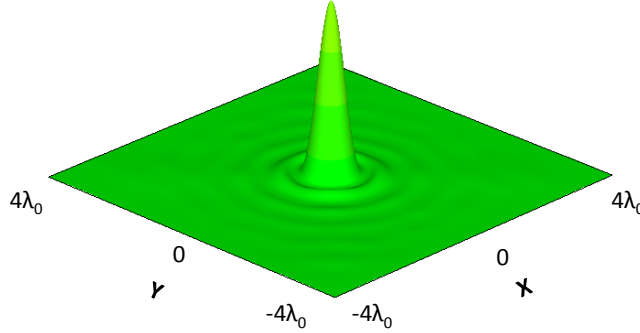


Figure 3.5: Magnitude of the normalized z -directed Poynting vector over the $z = 4\lambda_0$ plane.

$x=0$ plane for a plane wave incident from $z = -\infty$ and for a fixed instant in time. Clearly visible in the figure the spherical wavefronts generated on the right-hand side of the lens on both sides of the focal point as the waves converge and then start diverging as they leave the focal point. Figure 3.4 (b), shows the magnitude of the z -directed Poynting vector, demonstrating high power concentration within close proximity of the focal point. Figure 3.5 shows a normalized contour plot of the Poynting vector at the focal point plane ($z = 4\lambda_0$).

Note that equation (3.2) indicates that the rings' design, and consequently the focusing depended slightly on the frequency as long as the refractive indexes of the rings used to construct the lens varied slightly with frequency. This design, namely equation (3.2), was based on the assumption that a ray enters each of the annular rings and experiences a phase shift as it propagates through the lens along the $+z$ direction. If the thickness of the lens is increased, or alternately, is no longer electrically small, coupling is expected to take place between adjacent rings in a manner highly similar to coupling between closely spaced transmission lines [55, 56]. If the lens width increases, then the coupling can increase to sufficiently disturb the phase profile that was designed for at the exit side of the lens at $z=d$. From an optical point of view, the longer the path d , the larger the spreading of the wave, and hence the higher coupling between adjacent rings. If the coupling between adjacent layers increases, which would be the case when the thickness of the lens increases, the phase profile on the right-hand-side ($z=0$ in figure 3.2) would be different from what it is designed for, thus leading to a type of aberration or de-focusing. Therefore, even under the assumption that *each* ring has minimal or even zero dispersion, it should be kept in mind that the design equation was based on the assumption that each ray entering a ring

is confined to that ring until its exit. While a theoretical analysis to gauge the effect of the coupling cannot be foreseen at this time, the effect of such coupling, if needed, can be gauged numerically.

3.3 Flat reflector

The same strategy for inducing a scattered field that focuses at a specific point can be used to design a reflector that would focus the field at a specific focal point. Such reflector would perform the function of a paraboloid (dish reflector) as shown in figure 3.6. The reflector can be designed using the same principle of requiring the rays of an incident field that arrive normal to the reflector to scatter at different angles and converge at a focal point. The primary difference from the lens, however, is that the dielectric rings are now backed by a perfectly conducting sheet (at $z=d/2$) as shown in figure 3.7, thus forcing the incident ray to traverse the lens twice. Since the thickness of the reflector is chosen to be $d/2$, the design equation remains the same as the one for the lens (equation 3.2).

To validate the reflector design, consider a reflector disk with a radius and focal length of $4\lambda_0$. The thickness of the reflector would be half that of the lens designed earlier ($d/2=\lambda_0/20$). A perfectly conducting plate is positioned behind the dielectric multi-ring disk. Similar to the lens case, the incident plane wave arrives at the surface of the lens with uniform phase, it then propagates through the lens a round trip exiting with a phase profile designed to achieve convergence at the focal length. Figure 3.8-a shows the scattered electric field distribution on the $x=0$ plane. The profile of a spherical wavefront imploding at the focal point is visible. Figure 3.8-b shows the z -directed Poynting vector on the same plane of $x=0$; again showing strong concentration of the scattered field.

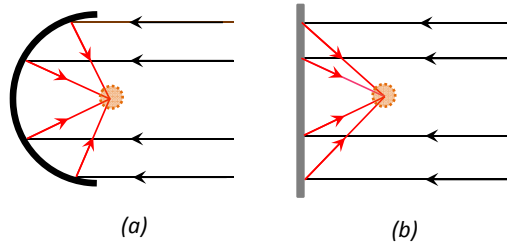


Figure 3.6: Cross section view at the center of a classical paraboloid reflector (a). Cross section view of a flat focusing reflector proposed in this paper (b).

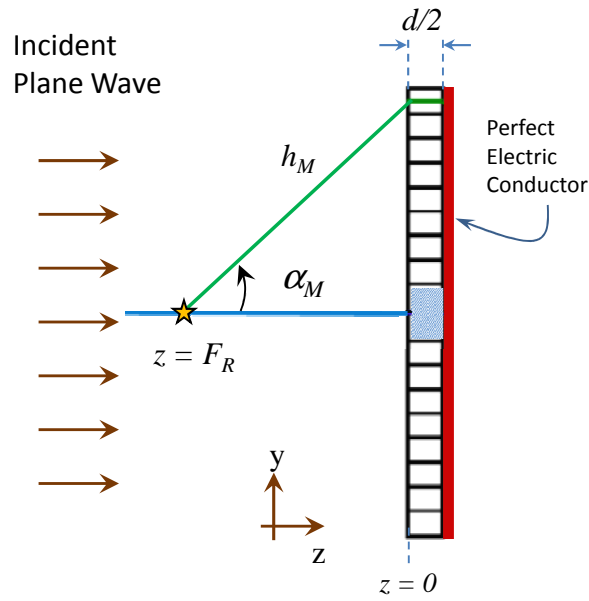


Figure 3.7: Cross section schematic of the reflector in the $x=0$ plane.

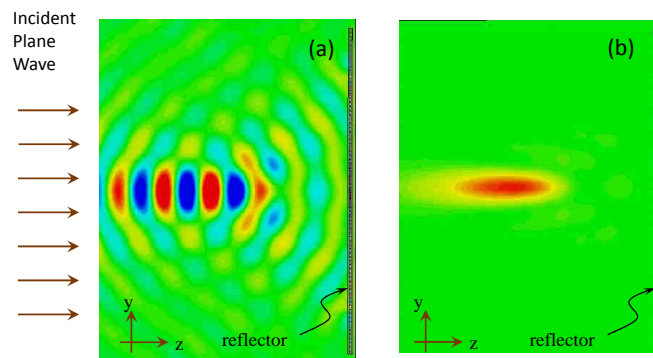


Figure 3.8: Magnitude of the scattered electric field over the $x=0$ plane. Color scale extends from -5.11V/m (deep blue) to 5.11V/m (deep red) (a). Magnitude of the z -directed Poynting vector over the $x=0$ plane. Color scale extends from 0 VA/m^2 (green) to 0.239 VA/m^2 (deep red) (b).

3.4 Fabrication and experimental results

A 2D lens and reflector were fabricated, tested and compared to numerical simulations. In contrast to the 3D lenses and reflectors presented in the previous section, the 2D concentrators are comprised of slabs of dielectric material infinite in the x direction instead of the concentric annular rings presented earlier. The design equation (equation (3.2)) remains the same. The difference here is that the focusing is over a focal axis instead of a focal point and the refractive index variation of the 2D devices is over the y direction. The 2D structures are used due to the building simplicity given that all building components are flat. On the other hand, the disadvantage is that the device is sensible to polarization on the incident wave.

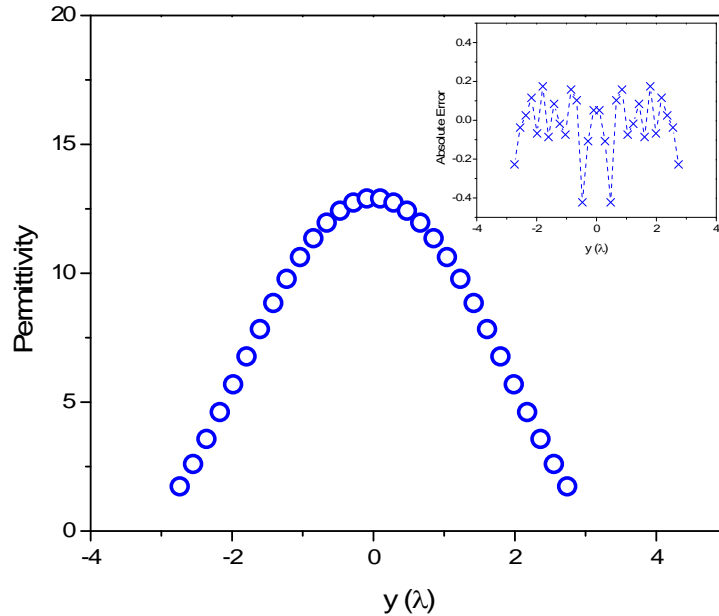


Figure 3.9: Relative permittivity for the electrically-thin flat lens as obtained from the design equation. Inset shows the absolute error (designed refractive index values minus dielectric used).

A flat lens was designed measuring 6λ in height and $d = \lambda/5$ in thickness. The lens consisted of 30 layers each $\lambda/5$ in height. A focal length of 9λ is chosen to obtain a dielectric profile that can be implemented with commercially available material. The refractive index profile of the design had a slight deviation from the fabricated lens due to difficulty in

finding dielectric material corresponding perfectly to the design values (see figure 3.9). For each lens' layer, the material was selected from dielectric laminates available from Rogers Corporation. Under the assumption that the layer thickness is electrically small ($d \ll \lambda$), during the fabrication of the final prototype, if a close dielectric match was not found in the available Rogers products, two dielectric layers were connected together to achieve an effective phase shift of $k_0 n_m d = k_0 \sqrt{\epsilon_{eff}} d$. For such layer, the effective permittivity ϵ_{eff} is calculated by using two available permittivities ϵ_1 and ϵ_2 as follows:

$$\epsilon_{eff} = \left(\frac{\sqrt{\epsilon_1} \Delta z + \sqrt{\epsilon_2} (d - \Delta z)}{d} \right)^2 \quad (3.4)$$

where d is the thickness of the layer and Δz is adjusted to achieve the desired ϵ_{eff} . Therefore, the electric field of the plane wave have to be selected in the \hat{x} direction.

The lens was simulated using the commercially available CST full-wave electromagnetic simulation tool [50]. Figs 3.10 and 3.11 show the Poynting and total electric field vectors in the $y - z$ plane simulated at 9.45 Ghz. Field concentration is clearly visible in and around the focal point which is 9λ from the surface of the lens. The bandwidth of the lens is mainly affected by the bandwidth of the dielectric materials. Figure 3.12 shows the \hat{x} directed electric field along the focal point axis for the $f=9.45$ Ghz (central frequency) and for $\pm 20\%$, $\pm 10\%$ and $\pm 5\%$ of the central frequency. The gain (equation 3.5) of the simulated frequencies remains within 4.1 dB and 4.5 dB for all cases.

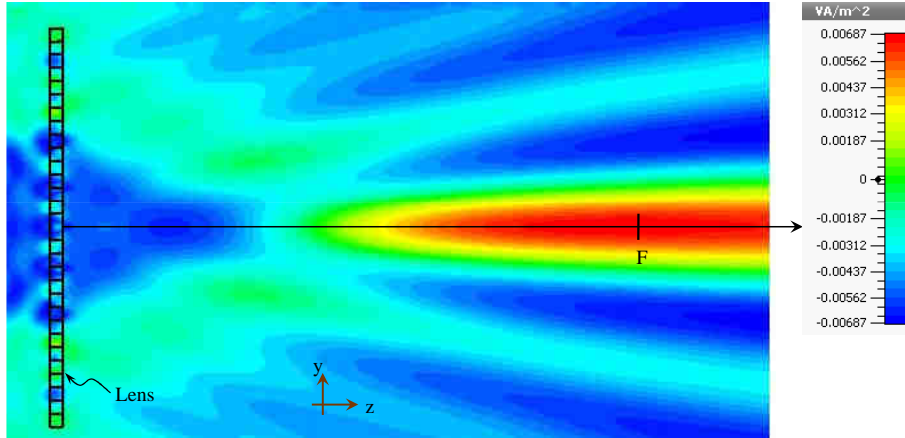


Figure 3.10: Magnitude of the simulated z -directed Poynting vector over the $y - z$ plane. Linear color scale extends from -0.00687 VA/m^2 (deep blue) to 0.00687 VA/m^2 (deep red).

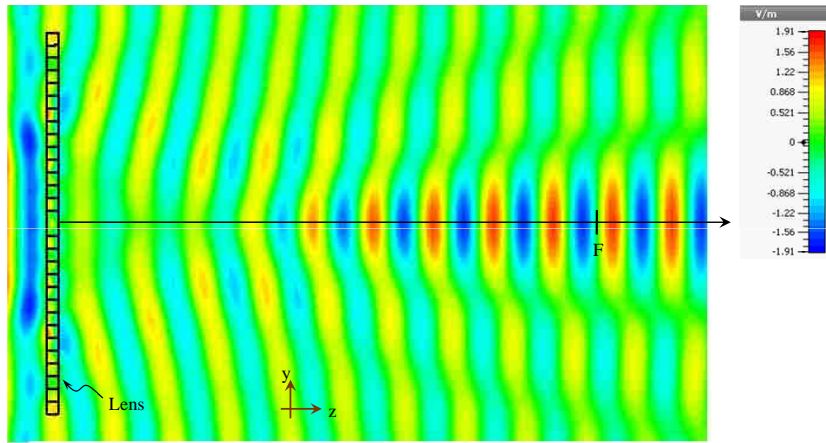


Figure 3.11: Magnitude of the simulated x -directed total electric field over the $y - z$ plane for a 6λ 2D lens and a focal point designed at 9λ . Linear color scale extends from -1.91 V/m (deep blue) to 1.91 V/m (deep red).

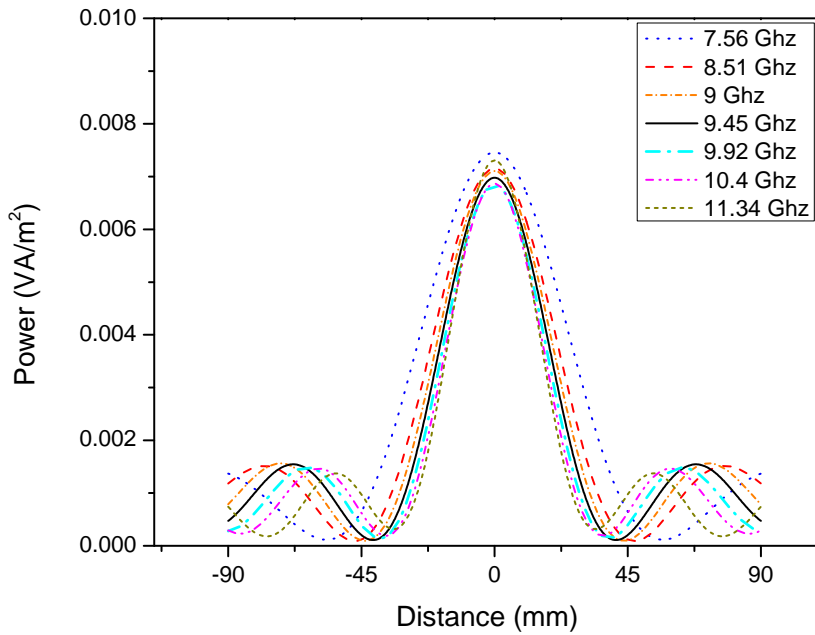


Figure 3.12: Magnitude of the simulated z -directed Poynting vector over the focal point axis for a 6λ 2D lens and a focal point designed at 9λ .

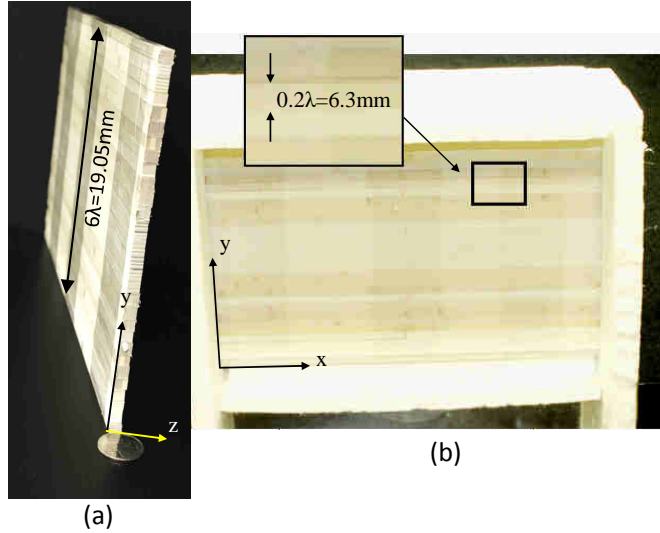


Figure 3.13: The 2D electrically-thin lens implemented by stacking dielectric layers (a). The lens placed in a Styrofoam frame (b).

Figure 3.13 shows the fabricated lens. Figures 3.14 and 3.15 show the experimental setup where an Agilent E8257D signal generator at 9.45 GHz was used as the microwave source along with a high gain horn antenna to generate a plane wave at the surface of the lens. The horn was placed at an electrically far distance (approximately 45λ from the lens) such that the lens experienced a plane wave. The received power was measured along the focal axis ($x = 9\lambda$ for the lens and $x = 4.1\lambda$ for the reflector) by an electrically-small probe positioned on a movable plexiglass fixture. Figure 3.14 (a) shows the schematic diagram of the lens focusing experiment.

Figure 3.16 shows the normalized detected power across the focal point axis (y -axis at $x = 9\lambda$). The normalization is made with respect to the highest power magnitude. The full-wave simulations and measurements show strong agreement in the vicinity of the focal point except for a slight vertical shift in the focal point due to possible misalignment between the probe's path and the y -axis of the lens. Possibly, the side lobes of the simulated patterns were not fully captured by the measurement probe due to potential multiple factors that include the probe's sensitivity and dynamic range and wave reflections in the laboratory environment. The numerical simulations assumed a perfect detection system with a probe having no dimensions and operated under negligible impedance loading.

Given that the lens was made of unmatched dielectric slabs of material, the efficiency is an important feature to consider. The definition used for this case was the ratio of the

Poynting vector integration along the focal axis (with the lens) over the Poynting vector integration over the same line without lens. The total efficiency calculated from simulation data was 77%.

Furthermore, to characterize the focusing effect and hence to demonstrate the power enhancement, the power gain of the lens can be defined in terms of the incident and the focused fields according to the following definition [45],

$$Gain = 20\log_{10}(|E_f|/|E_i|) \quad (3.5)$$

where E_f is the electric field at the focal point in the presence of the lens and E_i is the electric field of the incident plane wave at the focal point in absence of the lens. The power gain was measured to be approximately 4.2 dB. The gain calculated by CST full-wave simulator at the central frequency was 4.29 dB.

For the case of the reflector, the focal point is chosen such that the same lens is used. From equation (3.2), when the thickness of the dielectric slabs is doubled, the focal point distance F_R would be approximately half of the one for the lens. The approximation comes from the fact that the distance between the center of the reflector and the m^{th} layer (h_m) remains the same. Therefore, the implemented values are best fitted to a reflector's design having a focal point of 4.1λ . The absolute error between design and fabrication is shown in figure 3.17.

The reflector was constructed by using the same lens but placing an aluminum sheet on one side as discussed above. Figure 3.14 (b) shows the schematic diagram of the reflector focusing experiment. The normalized power at the focal axis of the reflector ($z = -4.1\lambda$) is shown in figure 3.18. The power gain of the reflector was also measured using the same definition as in [45] and was found to be 7.7 dB. The theoretical gain was calculated by the CST full-wave simulator to be 10.19 dB. Clearly, both the lens and reflector provide considerable enhancement of power even considering that the layers were not matched to free space.

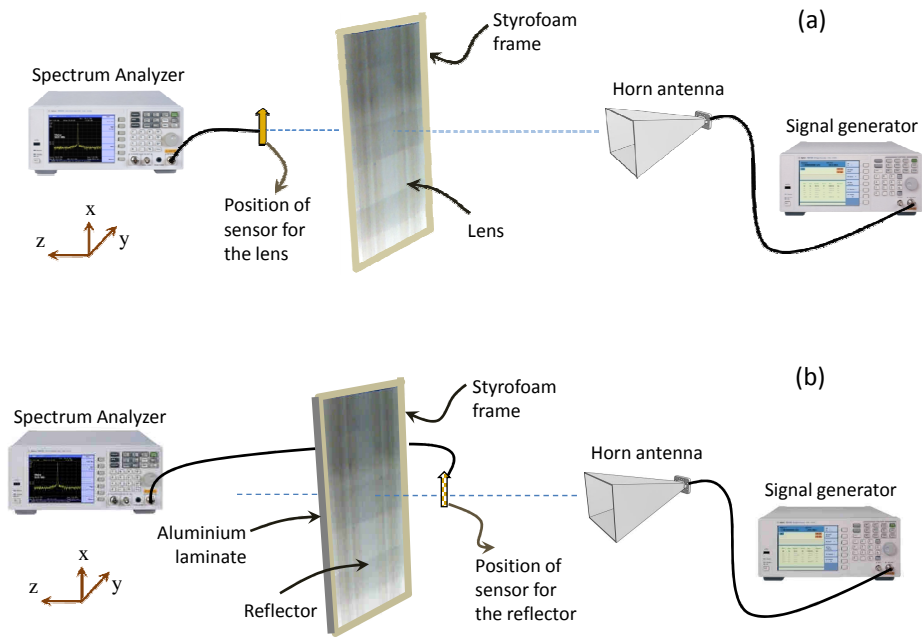


Figure 3.14: Diagram of lens (a) and reflector (b) focusing experiment. The lens and reflector were framed using Styrofoam. In the case of the lens, an electrically-small sensor was placed on the back of the lens and a horn antenna was placed in front of the lens. In the case of the reflector, the horn antenna and the sensor were placed on the same side (front of the reflector).

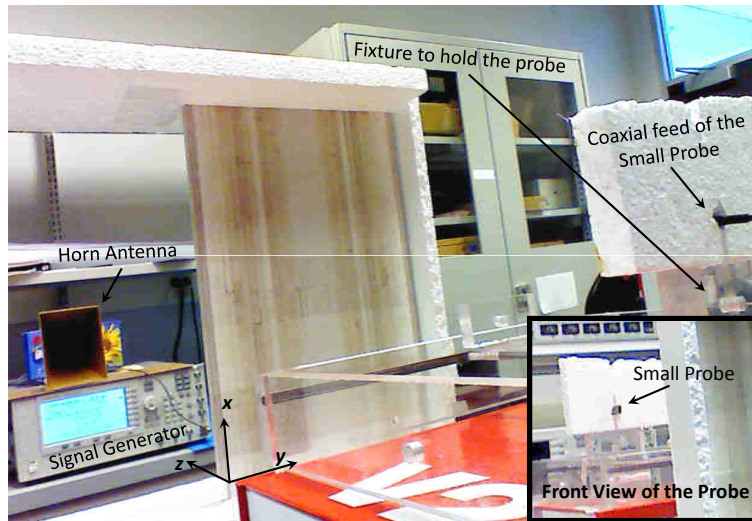


Figure 3.15: Received power measurement system. The lens was framed with Styrofoam. On one side of the lens an electrically small sensor was placed over a plexiglass moving fixture for power sweeping. Over the other side of the lens, a signal generator with a horn antenna at an electrically-long distance provided plane wave illumination.

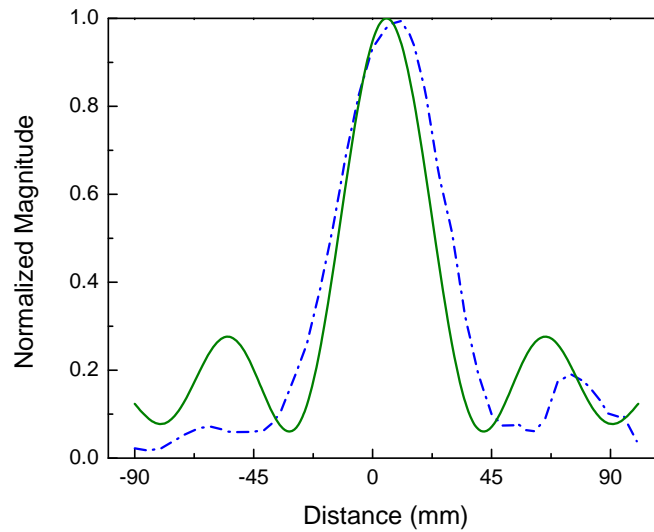


Figure 3.16: Normalized power of the electrically-thin flat lens across the focal point axis ($z = 9\lambda$, see Fig 3.2) obtained using simulation (green solid curve) and measurements (blue dash-dotted curve).

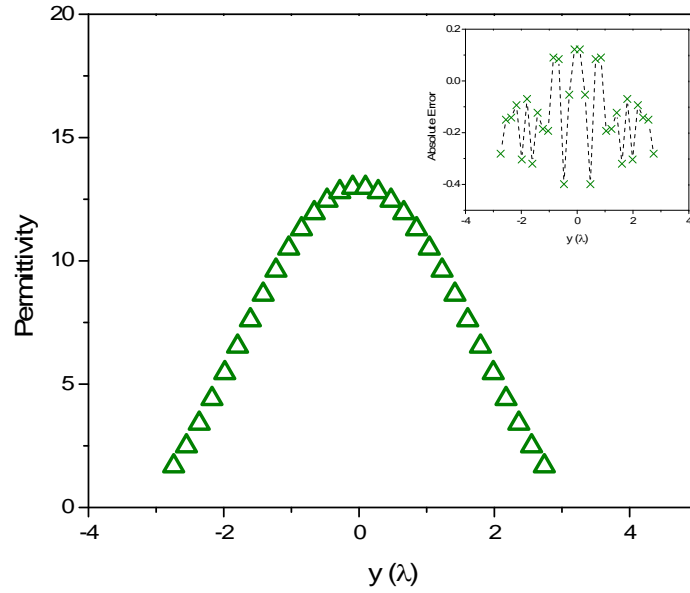


Figure 3.17: Relative permittivity for the electrically-thin flat reflector as obtained from the design equation. Inset shows the absolute error (designed refractive index values minus dielectric used).

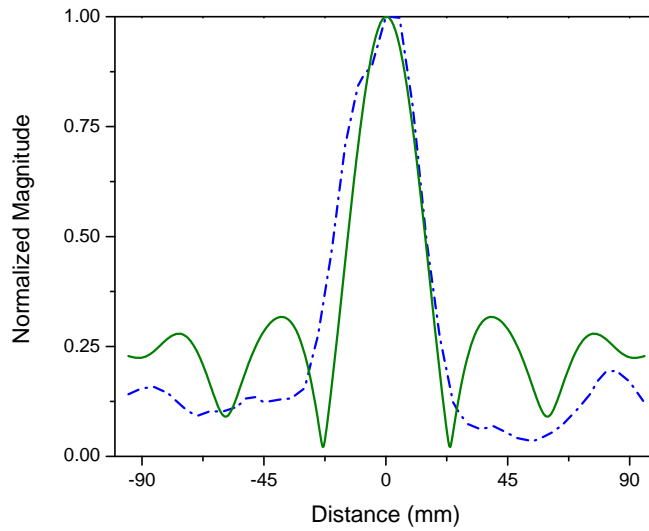


Figure 3.18: Normalized power of the electrically-thin flat reflector across the focal point axis ($x = 4.1\lambda$) simulation (green solid curve) and measurements (blue dash-dotted curve).

3.5 Electrically-thin lens and reflector for an enhanced dipole directivity

The electrically-thin lens and reflector can be used as collimators. The electrically-thin lens and reflector were designed such that a plane wave focuses at a single point. Strictly, the electromagnetic reciprocity theorem cannot be used to generate a plane wave from a point source since a plane wave can only be generated by a source of infinite current sheet or a line source placed at infinity. Nevertheless, significant (but not perfect) collimation can be achieved as demonstrated here. In fact, using a dipole fed by a finite current would approximate the field at a focal point obtained for the incident plane wave focusing scenario.

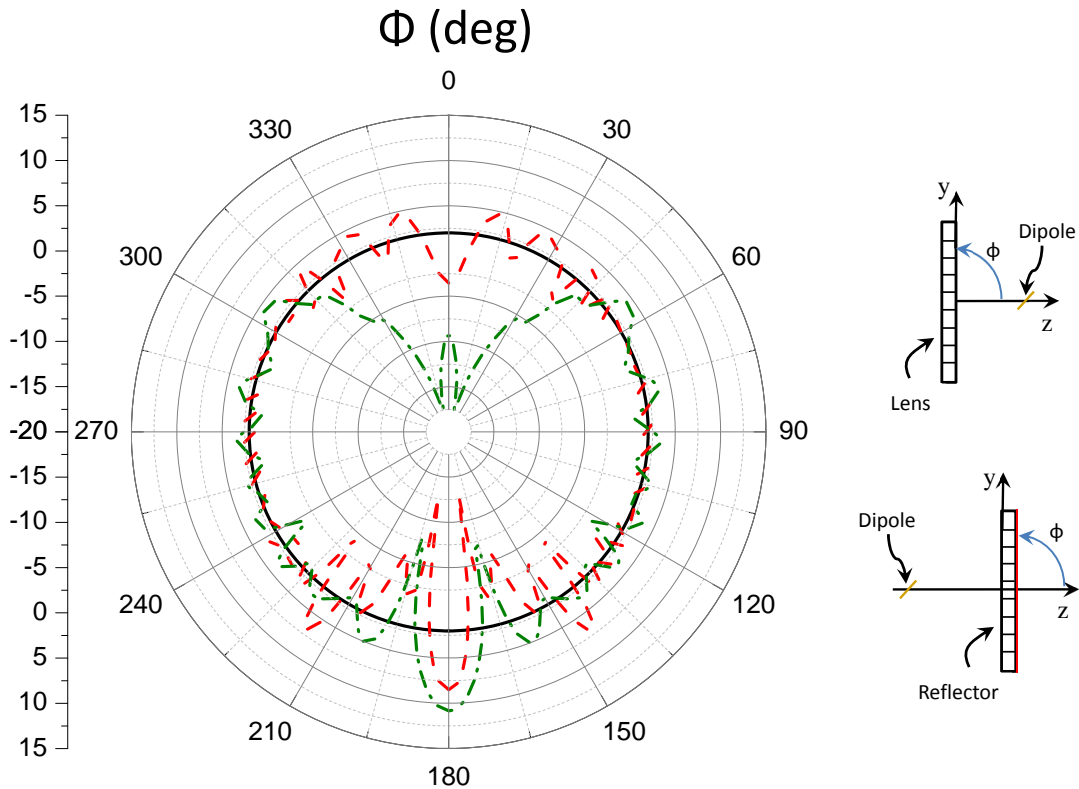


Figure 3.19: Simulation results for the far field pattern of a dipole antenna (solid black curve), with an electrically-thin lens (dashed red curve) and an electrically-thin reflector (dash-dotted green curve).

To determine the potential of the lens or reflector for increasing the directivity of antennas, I used an electrically-small printed dipole (total length of 8 mm) miniaturized with one 1 nH inductor on each arm. Figure 3.19 shows the directivity enhancement for a lens and a reflector. The directivity of the dipole is 2 dBi, whereas the directivity of the lens and reflector is 8.5 dBi and 10.8 dBi, respectively. Of course, the presence of a lens or reflector increased the radiation aperture size of the new radiator (i.e., the dipole and the lens/reflector), the advantage of employing the lens or reflector for increased directivity is cost, power efficiency and simplicity when compared to a typical large aperture radiator that would employ a more complex feeding circuitry and topology. I also observe that the performance of the reflector was better than the lens (by 2.3 dB) which can be attributed to the mismatching taking place at the lens interface.

3.6 Conclusion

In conclusion, a thin flat lens based on designing the refractive index to achieve a phase profile sufficient for ray convergence at a specified focal point was presented. The design is based on the assumption that the lens is electrically-thin, thus being fundamentally different from gradient-index techniques which bend the rays *within* an electrically-thick lens [9]. A numerical example was presented where aberration-free focusing was achieved at a specific focal point. The design provides the flexibility of not requiring the focal point to be in the far field.

Because of the ray behavior assumption of the field interaction with the dielectric layers of the lens, the design is most suitable for large aperture lenses. Furthermore, using the same methodology presented here for lens design, a flat reflector can be designed with a focal point. The results for the 3D lenses and reflectors presented in this chapter were purely based on full-wave electromagnetic simulation. For the examples presented, the dielectric material needed for building the lens and reflector requires the availability of a material with refractive index ranging from 1 to 18. To minimize reflection, the permeability and permittivity can be chosen to be equal to the refractive index.

Furthermore, a 2D electrically-thin flat lens and reflector were designed and constructed using available printed circuit board dielectrics. The designs for the lens and reflector were implemented with the available materials which in some cases lead to a combination of thinner slabs of different dielectric constants that achieved the effective permittivities desired. The designs and formulations of sections (3.2) and (3.3) were validated through experimentation by proving the concentration of energy in a focal point for the implemented lens and reflector. Even though mismatching existed between the dielectric layers

comprising either the lens or reflector and free space, both, the lens and reflector showed an appreciable gain enhancement at the focal point compared to the incident wave with no concentrator. Additionally, numerical simulation demonstrated that the reflector can be effective collimators. Both showed a significant improvement in directivity. Overall, the reflector with a dipole showed the best performance. The experimental lens and reflector can be improved further by using matched materials which are not commercially available. However, closely matched materials have been subject of study and have been successfully fabricated [52]. The authors in [52] presented a variety of materials with similar permittivity and permeability values, and relatively high refractive indexes. These materials may be used to substitute the circuit boards such that matching with free space is improved and the reflections minimized.

Chapter 4

Analytical model of electrically-thin inhomogeneous media

4.1 Introduction

This chapter presents analytical models for two-dimensional (2D) and three-dimensional (3D) electrically-thin lenses and reflectors. The 2D formulation is based on infinite current line sources, whereas the 3D formulation is based on electrically-small dipoles. These models emulate the energy convergence of an electrically-thin flat lens and reflector when illuminated by a plane wave with specific polarization. The advantages of these models are twofold: first, prediction of the performance of electrically-thin flat lenses and reflectors can be made significantly faster than full-wave simulators, and second, providing insight on the performance of these electrically-thin devices. The analytic models were validated by comparison with full-wave simulation for several interesting examples. The validation results show that the focal point of the electrically-thin flat lenses and reflectors can be accurately predicted through a design that assumes low coupling between different layers of an inhomogeneous media.

Full-wave electromagnetic simulation gives high accuracy that encompasses the full "spectrum" of wave phenomena including reflection, refraction and even diffraction. The only drawback from using full-wave simulation is its high computational cost (computer memory and time). For the type of problems encountered in flat lenses and reflectors, the desired focal point might fall within the near or far field, which necessitates the inclusion of relatively large space in the computational domain. This makes the solution very time consuming and memory intensive, especially for optimization and design. The

models presented here are not restricted to lenses and reflectors but can be used for general inhomogeneous slabs.

4.2 Theory

An analytical model aims to reproduce the physics of a problem accurately while preserving a low complexity. Solving the scattered field of electrically short slabs illuminated by a plane wave tends to be a more difficult problem than solving problems where only current sources or electrically small dipoles in free space are involved.

For the case of electromagnetic problems of sources in free space, there is a variety of different alternatives to solve them. One of the alternatives is finding an intermediate vector that leads to the desired field similar to the use of auxiliary variables when solving integrals.

The calculation of electric fields is often simplified by this "intermediate vector" which is named magnetic vector potential. The models presented in the current chapter are formulated based on this vector. For this reason, the theory of the magnetic vector potential (\mathbf{A}) is presented here. The formulation of the vector \mathbf{A} is based on the following vector identity,

$$\nabla \cdot (\nabla \times \mathbf{a}) = 0 \quad (4.1)$$

In Maxwell equations, the curl of the magnetic induction does not vanish, but its divergence does. Given the identity in equation (4.1); then, it is possible to assume that the magnetic field \mathbf{H} be represented by [57, 58],

$$\mathbf{H} = \nabla \times \mathbf{A} \quad (4.2)$$

where \mathbf{A} is the magnetic vector potential. This vector has no physical interpretation by itself. Instead, it is a mean to find the electric or magnetic field.

Then, by Maxwell equations it can be found that,

$$\nabla \times \mathbf{H} = \nabla \times \nabla \times \mathbf{A} = \mathbf{J} + j\omega\epsilon\mathbf{E} \quad (4.3)$$

where \mathbf{J} is the source or impressed current, \mathbf{E} is the electric field, μ is the permeability and ϵ is the permittivity.

Considering Faraday's law,

$$\nabla \times \mathbf{E} = -j\omega\mu\mathbf{H} \quad (4.4)$$

Substituting the magnetic field from equation (4.2) into equation (4.4), then,

$$\nabla \times (\mathbf{E} + j\omega\mu\mathbf{A}) = 0 \quad (4.5)$$

Considering and comparing the following identity to equation (4.5),

$$\nabla \times (\nabla a) = 0 \quad (4.6)$$

In words, a curl free vector is the gradient of a scalar. Then, it is possible to define $\mathbf{E} + j\omega\mu\mathbf{A}$ of equation (4.5) as a gradient of a scalar,

$$\mathbf{E} + j\omega\mu\mathbf{A} = -\nabla\Phi \quad (4.7)$$

where Φ is the electric scalar potential.

Substituting equations (4.2) and (4.7) into Ampere's law, leads to [57],

$$\nabla \times \nabla \times \mathbf{A} - k^2\mathbf{A} = \mathbf{J} - j\omega\epsilon\nabla\Phi \quad (4.8)$$

where Ampere's law is given by $\nabla \times \mathbf{H} = j\omega\epsilon\mathbf{E} + \mathbf{J}$ and k is the wave number.

By vector identity, equation (4.8) becomes,

$$\nabla(\nabla \cdot \mathbf{A}) - \nabla^2\mathbf{A} - k^2\mathbf{A} = \mathbf{J} - j\omega\epsilon\nabla\Phi \quad (4.9)$$

By choosing,

$$\nabla \cdot \mathbf{A} = -j\omega\epsilon\Phi \quad (4.10)$$

Then, equation (4.9) simplifies to the so called Helmholtz equation,

$$\nabla^2\mathbf{A} + k^2\mathbf{A} = -\mathbf{J} \quad (4.11)$$

Finally, rewriting the magnetic field and finding the electric field solved in terms of the magnetic vector potential [57],

$$\mathbf{E} = -j\omega\mu\mathbf{A} + \frac{1}{j\omega\epsilon}\nabla(\nabla\cdot\mathbf{A}) \quad (4.12)$$

$$\mathbf{H} = \nabla \times \mathbf{A} \quad (4.13)$$

For the case of a 2D electrically-thin flat slab (slab located in the x-z plane with refractive index variation in \hat{y} direction only), the scattered field of a wave illuminating the slab can be modeled by two dimensional sources of cylindrical waves as will be discussed in the next section. These waves are independent of the z-coordinate, i.e. infinite current sources. The solution to equation 4.11 that represent outward-traveling waves is a Hankel function zeroth-order, second kind,

$$A_z = CH_0^{(2)}(k\rho) \quad (4.14)$$

where ρ is the distance from the source to the observation point and C is a constant determined by,

$$H_\phi = -\frac{\partial A_z}{\partial \rho} = -C\frac{\partial}{\partial \rho}H_0^{(2)}(k\rho) \quad (4.15)$$

where $\lim_{\rho \rightarrow 0} \oint H_\phi \rho d\phi = I$

Solving equation (4.15) for $k\rho \rightarrow 0$, the constant C yields,

$$C = \frac{I}{4j} \quad (4.16)$$

Then, the magnetic vector potential of an infinite current line on the z-axis is given by [57],

$$A_z = \frac{I}{4j}H_0^{(2)}(k\rho) \quad (4.17)$$

Although infinite current lines are useful for modeling 2D inhomogeneous media, they are not suitable to model 3D cases (electrically-thin in \hat{y} with refractive index variation in \hat{x} and \hat{z} slab). A more convenient source to be use in 3D cases is an infinitesimal electric dipole. Small dipoles can account for variations in the refractive index of a slab or film. The x-z plane can be discretized to allocate dipoles in order to calculate the scattered fields. The solution for \mathbf{A} in equation (4.11) corresponds to the solution a second order partial differential equation. Given that this equation is linear, its solution can be expressed as a

linear superposition of point sources' solutions. Therefore, the solution of equation (4.11) is given by,

$$\mathbf{A}(\mathbf{r}) = \iiint_V \mathbf{J}(\mathbf{r}') G(\mathbf{r}, \mathbf{r}') dV' \quad (4.18)$$

where $G(\mathbf{r}, \mathbf{r}') = \frac{e^{-jk|\mathbf{r}-\mathbf{r}'|}}{4\pi|\mathbf{r}-\mathbf{r}'|}$ is the Green's function for free space.

Then, the magnetic vector potential for infinitesimal electric dipoles can be expressed as [57, 58],

$$\mathbf{A}(\mathbf{r}) = \frac{1}{4\pi} \iiint_V \mathbf{J}(\mathbf{r}') \frac{e^{-jk|\mathbf{r}-\mathbf{r}'|}}{|\mathbf{r}-\mathbf{r}'|} dV' = \frac{1}{4\pi} \int_{-l/2}^{l/2} I \hat{z} \frac{e^{-jk|\mathbf{r}-\mathbf{r}'|}}{|\mathbf{r}-\mathbf{r}'|} dz' = \frac{I l e^{-jk|\mathbf{r}-\mathbf{r}'|}}{4\pi r} \hat{z} \quad (4.19)$$

In the next section, magnetic vector potential of cylindrical current sources infinite in \hat{z} and infinitesimal current sources are used to find the electric field distribution of the scattered field due to a perpendicularly incident plane wave.

4.3 Model for 2D lenses and reflectors

Considering slabs in two-dimensional space. Figure 4.1(a) shows a thin slab of inhomogeneous material illuminated by a plane wave that is incident normally on the flat surface. The phase of the incident plane wave at the left side of the slab is uniform as shown in figure 4.1(a). As the incident wave propagates through each layer, it experiences a phase shift proportional to the refractive index of each layer. These phase shifts translate into proportional delays in time domain. In other words, the peak of the wave exits different layers at different times. Figure 4.1(a) shows a generic phase profile of the incident plane wave at the right hand side of a slab composed of M dielectric layers. The assumption that the slab depth (or thickness) d is much smaller than the wavelength of the incident field results in minimal coupling between the dielectric layers (see section 3.2). Minimal or negligible coupling between the dielectric layers indicates that the emerging incident field from each dielectric layer can be considered as an independent source in a manner similar to the application of Huygen's theory to the problem of scattering from electrically-small apertures. Therefore, each layer can be modeled as an independent line source (infinite current source in two-dimensional space) as shown in figure 4.1(b)). The line sources are polarized in the \hat{z} direction. Each current source is assigned a phase shift corresponding

to the distance d multiplied by the wave number of the respective dielectric layer. The phase shifts or phase differences between current lines are presented as a time difference of the expanding wave fronts (in red) shown in Fig 4.1(b). The time difference is expressed in the different radii of the propagating wavefronts (peak values of the waves) diverging from the current filaments. Since each current source is independent, its field can be calculated using cylindrical waves. For normal plane wave incidence (in the \hat{y} direction (see Fig 4.1(a)) the amplitude of each current source is kept uniform.

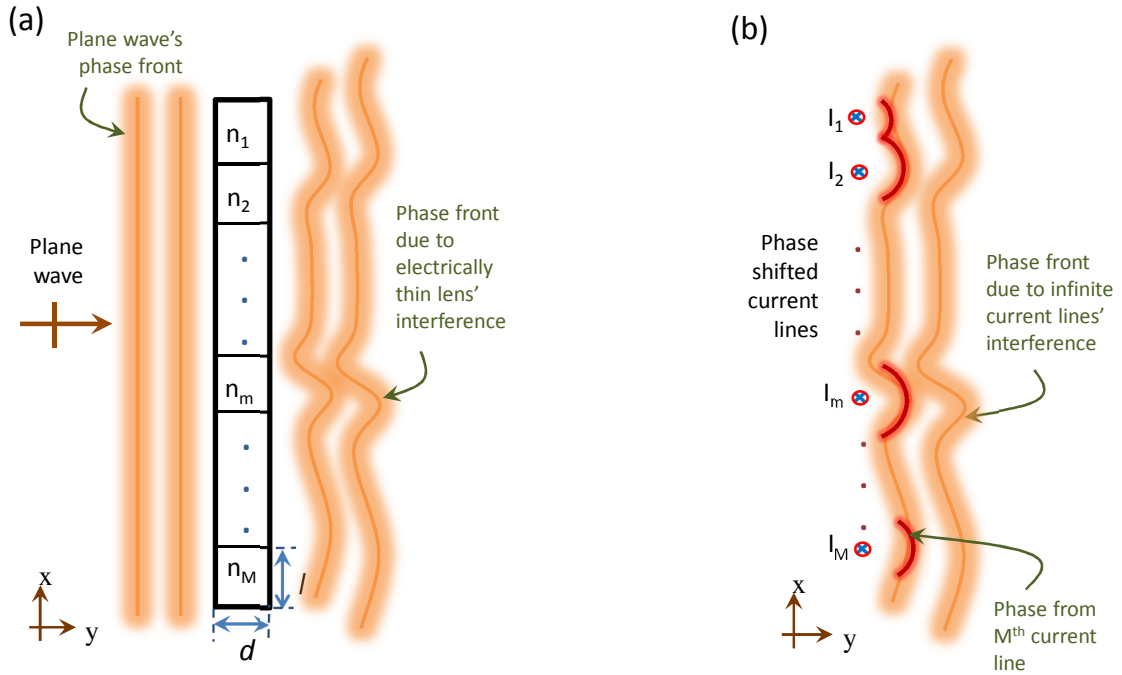


Figure 4.1: Electrically-thin inhomogeneous slab illuminated by a plane wave (a). Infinite current line model (b).

For a slab with M dielectric layers, the solution of one current filament (which models one layer), can be constructed using the magnetic vector potential (see equation 4.17),

$$A_z = \frac{I e^{-j d k_m}}{4j} H_0^{(2)}(k_0 | \vec{\rho} - \vec{\rho}' |) \quad (4.20)$$

where $H_0^{(2)}$ is the zeroth order Hankel function of the second kind, k_0 is the wave number in free space, I is the current magnitude, $e^{-j d k_m}$ is the phase of the wave at the exit side of

the slab (phase of the current in the model), d is the slab's thickness, k_m is the wavenumber of the m^{th} layer and $|\vec{\rho} - \vec{\rho}'|$ corresponds to the radial distance between the source and the observation point in the cylindrical coordinate system. The electric and magnetic fields can then be derived from the magnetic potential using equations (4.12) and (4.13),

$$E_z = \frac{-k_0^2 I e^{-j d k_m}}{4 \omega \epsilon_0} H_0^{(2)}(k_0 |\vec{\rho} - \vec{\rho}'|) \quad (4.21)$$

$$H_\phi = \frac{-k_0 I e^{-j d k_m}}{4 j} H_0^{(2)'}(k_0 |\vec{\rho} - \vec{\rho}'|) \quad (4.22)$$

Equations (4.21) and (4.22) represent the fields on the right-hand-side of the slab due to the m^{th} current filament that corresponds to a single electrically-thin dielectric layer of refractive index n_m .

To obtain the total field contribution of all layers, the coordinates of equation (4.21) have to be transformed to the m^{th} layer position. Therefore, the field contribution due to all layers is the sum over all layers

$$E_{Tz} = \sum_{i=1}^M \frac{-k_0^2 I e^{-j d k_m}}{4 \omega \epsilon_0} H_0^{(2)}(k_0 |\vec{\rho} - \vec{\rho}'_i|) \quad (4.23)$$

where $\vec{\rho}'_i$ is the location of the i^{th} current source, $\vec{\rho}$ is the location of an arbitrary observation point located on the right-hand-side of the slab. This formulation was programmed using Matlab to find the field at each observation point of interest.

Three different examples are presented here. A random refractive index profile is used with the solely purpose of validating the analytical model, whereas the two other examples are applications: a 2D flat converging lens and a 2D Off-axis reflector.

2D Random Inhomogeneous Medium

In order to validate this model, a 2D inhomogeneous flat slab was considered as an example. The slab has a dimension of 6λ and divided into 60 dielectric layers of thickness $\lambda/10$. In this particular example, for the purpose of validation *only* and not any useful objective, the refractive index profile was selected randomly and is shown in figure 4.2.

Figure 4.3 shows the z-polarized electric field obtained from the full-wave numerical simulation of the slab (full-wave simulation was performed using CST MICROWAVE STUDIO ®(CST MWS) [50]) and the electric field obtained using the analytic formulation presented here. Strong agreement is found between the two solutions except in the region very close

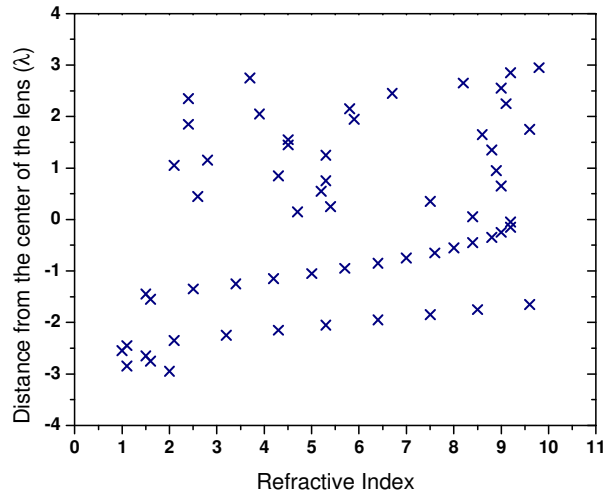


Figure 4.2: Randomly chosen refractive index profile of the dielectric layers comprising a flat slab.

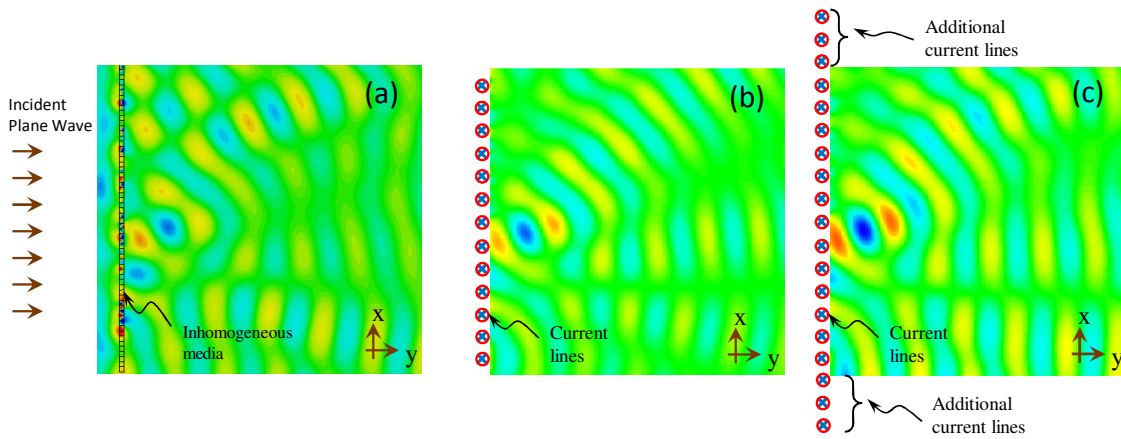


Figure 4.3: Two-dimensional distribution of the electric field on the right-hand-side of a 6λ inhomogeneous slab with a refractive index profile shown in figure 4.2 obtained using full-wave simulation (a), current line model without additional current line sources (b), and current line model with additional current line sources (c).

to the slab. The discrepancies in the near-field region is attributed to the fact that the model considers a finite number of current lines corresponding to the number of dielectric layers, while the simulation considers a continuous medium and a plane wave that

propagates everywhere in space.

For this particular example with arbitrary dielectric profile, the objective was not to achieve any particular convergence of the waves and, thus, spreading of the waves across the entire space to the right of the slab is expected. Notice that in this case, the incident plane waves that do not impact the slab will contribute to the total field value. Additional current lines were added at the top and bottom of the lens in order to account for these plane waves that do not impact the slab. However, these additional current lines did not improve significantly the total field. Figure 4.3 shows the z-polarized electric field distribution to the right of the slab for the full-wave simulation.

2D Flat Converging Lens

The 2D current model can be used to predict the performance of a 2D flat converging lens significantly much faster than full-wave simulation. As an example, a 2D lens with a height of 6λ is considered. The thickness and width of each layer is $\lambda/10$. The design formulation (equation (3.2)) results in the refractive index profile shown in figure 4.4.

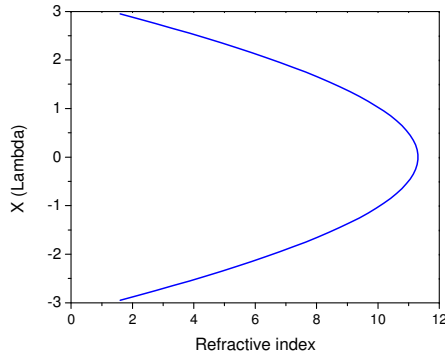


Figure 4.4: Refractive index design profile.

Figure 4.5 shows the electric field of the converging lens using full-wave numerical simulation and the current lines model in equation (4.23). Figure 4.6 shows the electric field along an axis parallel to x at $y=4\lambda$. Notice that adding additional line sources improved the accuracy of the analytical model. Strong agreement is found between the full-wave numerical simulation and the analytic solution. In fact, the strong agreement further validates the assumption that the coupling between the layers of different materials is negligible provided that the lens is electrically thin. Notice that all currents in the model have the same amplitude but defer in phase. The converging phase front is a consequence of the designed phase profile assigned to each line. Remind that current lines model

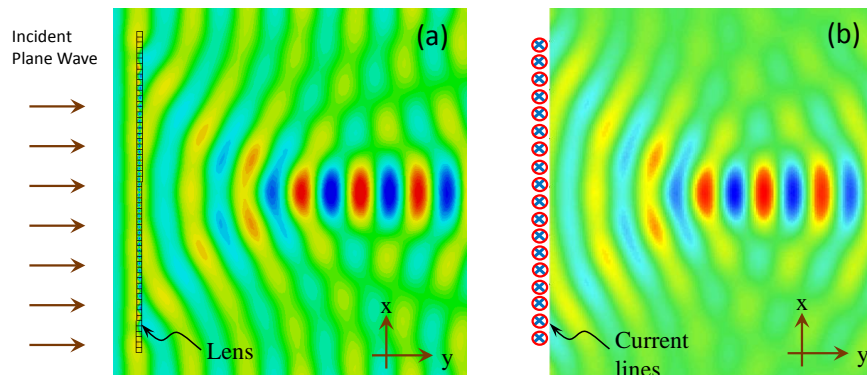


Figure 4.5: Two-dimensional distribution in the x - y plane of the electric field for a 6λ lens obtained using full-wave simulation (a) and the current line model (b).

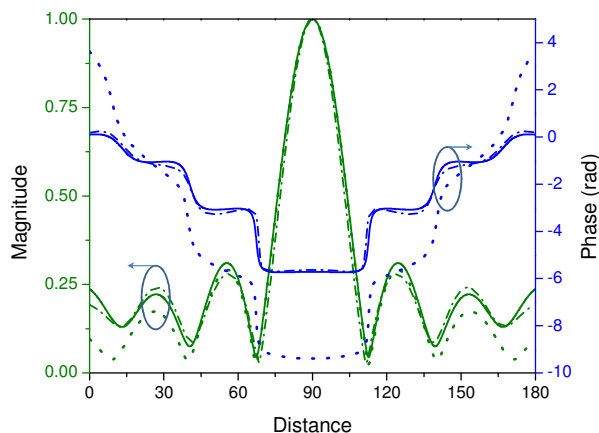


Figure 4.6: One-dimensional distribution of the normalized magnitude and phase of the electric field for a 6λ lens along a line parallel to the x -axis and at $y=4\lambda$ obtained using full-wave simulation (solid line), current line model employing 60 line currents (dotted lines) and current line model employing 120 uniformly distributed line currents (dashed-dotted lines).

assumes no coupling between the sources. Although the numerical simulation accounts for any possible coupling, the strong agreement between the two solutions indeed validate the assumption of low coupling between adjacent dielectric layers. Naturally, the effectiveness of the analytical model decreases if the lens becomes thicker. In figure 4.7, the magnitude

and phase of the electric field is shown for two lenses having thickness of 1λ and 2λ , where λ is the wavelength in free space. It is interesting that the line currents model still gives a reasonable approximation for the magnitude of the field even for a 2λ -thick lens. The deterioration in the phase, however, seems to be more pronounced with thickness.

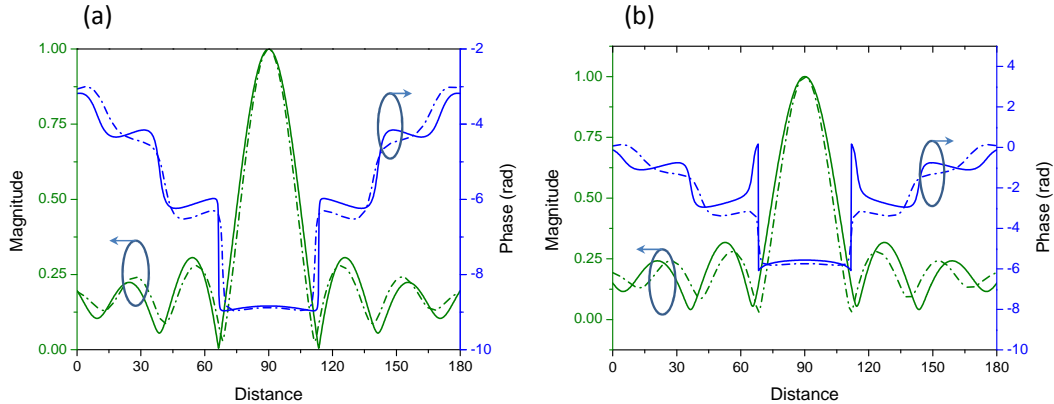


Figure 4.7: One-dimensional distribution of the normalized magnitude and phase of the electric field for a 6λ lens along a line parallel to the x-axis and at $z=4\lambda$, where $z=0$ is at the exiting side of the lens, for thickness of 1λ (a) and 2λ (b). Full-wave simulation (solid line), current line model employing 120 uniformly distributed line currents (dashed-dotted lines).

2D Off-axis reflector

A flat reflector's design is dictated by equation (3.2) with half the thickness of the lens design. Rewriting the equation for convenience,

$$n_f d/2 + F = n_m d/2 + h_m \quad (4.24)$$

where n_f is the refractive index at the focal axis, h_m is the distance from the focal point to the middle of the m^{th} layer, n_m is the refractive index of such layer, F is the distance from the reflector to the focal point, and $d/2$ is the thickness of the reflector's dielectrics (see Fig 4.8).

The layers of the reflector are numbered from $m=1$ to $m=M$ (see Fig 4.8). The focal axis is considered to be at layer $m = f$ (with refractive index of n_f), where $f < M/2$. The refractive index of the region extending from $m=f$ up to $m=M$ is calculated first. Vacuum is considered as layer $m = M$. The reason for designing the dielectrics from $m = f$ to

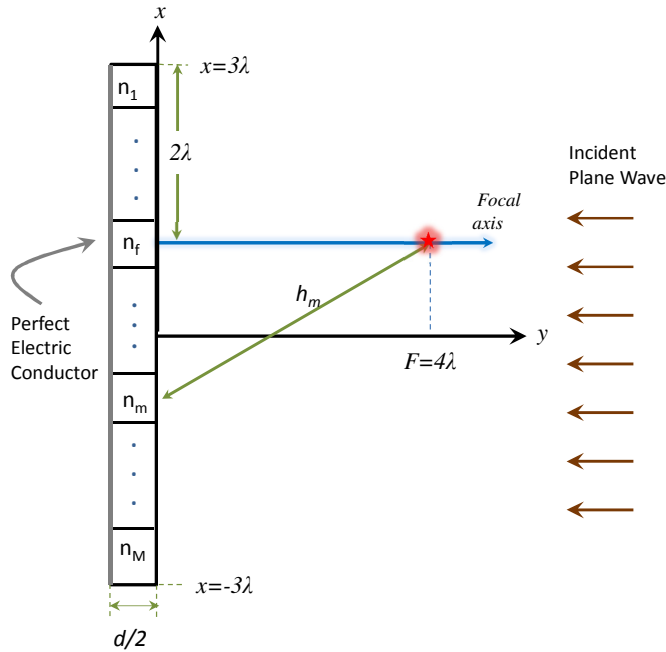


Figure 4.8: Off-axis flat reflector schematic.

$m = M$ is for maintaining low dielectric values as practically possible. Equation (4.24) shows that the refractive index increases monotonically until the maximum is reached at $m=f$. According to (4.24), if the region $m = 1 < i < m = f$ is chosen first and the first refractive index is chosen to be 1, then negative refractive index materials would be needed at some point in the region $m = f < i < m = M$. In order to avoid the use of negative refractive index materials, (4.24) is solved by calculating the refractive index of each layer with vacuum as the reference for the first region. For the second region which includes the layers from $m=f$ to $m=M$, the refractive index m_f is set as a reference to calculate the remaining values.

Figure 4.9 shows the scattered z-polarized electric field of a 6-lambda flat reflector. The reflector is $\lambda/20$ thick. The focal point is at $F = 4\lambda$ and the focal axis was chosen 2λ from the top of the reflector (see Fig 4.8). Notice that for the case of the scattered field there is no need to add additional current lines at the top and bottom of the reflector as was done in the case of the random refractive index flat lens since only the reflected (scattered) wave is calculated.

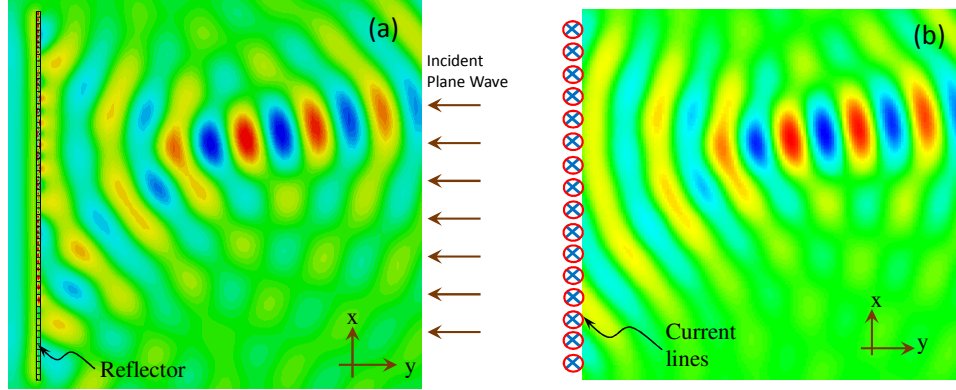


Figure 4.9: Two-dimensional distribution of the scattered electric field from a 6λ off-axis reflector obtained using full-wave simulation (a) and the current line model (b).

4.4 Model for 3D lenses and reflectors

In contrast to the 2D case where the lens and reflector are made of rectangular layers (infinite in the third dimension), the 3D lens is formed by concentric annular rings of different refractive indexes. In addition to the primary feature of a 3D lens in converging energy in three-dimensional space, the 3D lens has dual polarization property. The 3D lens is able to receive any polarization as long as the lens is illuminated by a normally incident plane wave (normal to the plane of the lens).

The analytic model for the 3D lens is formed by replacing the concentric rings in Figure 4.10(a) by infinitesimal electric dipoles as shown in Figure 4.10(b). The phase of the infinitesimal dipoles corresponds to the phase of the wave at the exit side of the lens for each ring. This phase represents the delay the wave experiences as it propagates through the dielectric medium of each ring. The dipoles are aligned and polarized according to the polarization of the incident plane wave (selected to be in \hat{z} direction). The field due to each dipole is derived using the magnetic vector potential (equation 4.19) and then the electric field is calculated from the potential function. The vector potential is given by [58],

$$A_z = \frac{\mu_0 I l e^{-j d k_m}}{4\pi r} e^{-j k_0 |\mathbf{r} - \mathbf{r}'|} \quad (4.25)$$

where μ_0 is the permeability of free space, I is the current magnitude, $d k_m$ is the phase of the wave at the exit side of the lens (same as the phase of the current in the model), k_m is the wave number of the m^{th} ring, d is the thickness of the lens, l is the length of

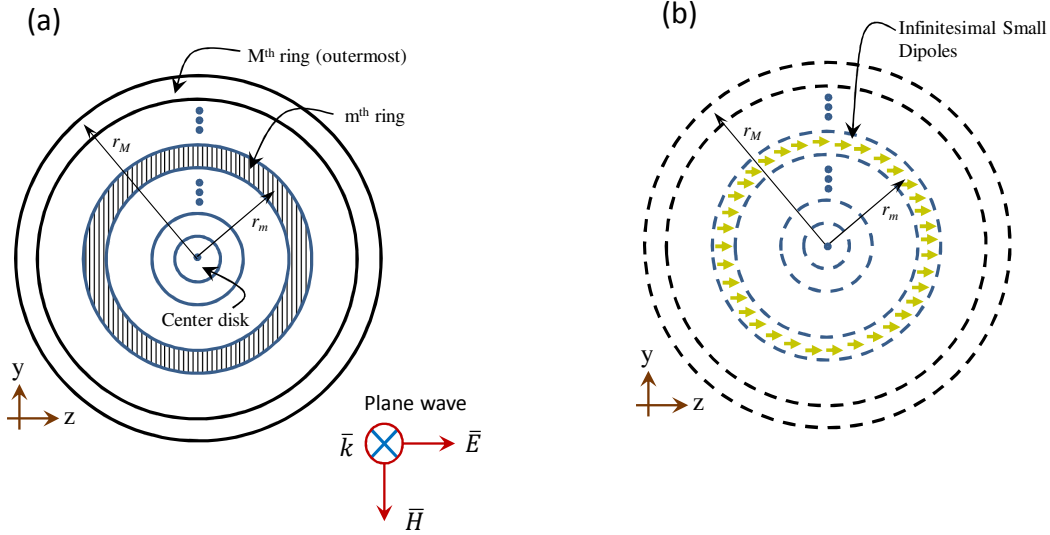


Figure 4.10: Electrically-thin lens illuminated by a plane wave (a). Infinitesimally electric dipole model (dipoles are shown for the m^{th} layer only) (b).

the filament, r is the distance from the filament to an observation point and k_0 is the wavenumber of free space.

The electric field in the same direction of the current is given by [58],

$$E_z = -j\omega\mu A + \frac{1}{j\omega\epsilon} \nabla(\nabla \cdot A) \quad (4.26)$$

Equations (4.25) and (4.26) correspond to a single infinitesimal dipole. To obtain the total contribution of all positions, the coordinates of equation (4.26) have to be transformed to the m^{th} position. Then, the contributions of the M-layers must be summed to find the total electric field distribution.

$$E_{Tz} = \sum_{i=1}^D -j\omega\mu \left(\frac{\mu_0 I e^{-j k_m l}}{4\pi |\vec{r} - \vec{r}'_i|} e^{-j k_0 |\vec{r} - \vec{r}'_i|} \right) + \frac{1}{j\omega\epsilon} \nabla \left(\nabla \cdot \left(\frac{\mu_0 I e^{-j k_m l}}{4\pi |\vec{r} - \vec{r}'_i|} e^{-j k_0 |\vec{r} - \vec{r}'_i|} \right) \right) \quad (4.27)$$

where $|\vec{r} - \vec{r}'_i|$ is the distance between the observation point \vec{r} and the i^{th} infinitesimal dipole \vec{r}'_i .

In order to validate the 3D model, the lens example from section (3.2) is used here to validate the analytical model. A total of 4515 dipoles were used in the analytical model. The central disc was replaced by 5 dipoles, whereas the rest of the rings were replaced by a number of dipoles proportional to the circumference of the m th ring such that all dipoles were uniformly spaced. Note that for the particular lens example considered here (8λ diameter and ring width of $\frac{\lambda}{10}$), the lower limit on the number of dipoles for the analytical model would be 903 based on using one dipole for the central disc and incrementally increasing the number of dipole by one for each consecutive larger ring. In figure 4.11, the one-dimensional normalized (with respect to the maximum value) distribution for the z -polarized electric field for the lens using full-wave simulation, analytical model using 903 dipole and analytical model using 4510 dipoles is presented. It can be noticed that lower number of dipoles break the symmetry in the solution. Clearly, the higher the number of dipoles used in the analytic model, the higher the solution accuracy; however, the trade-off is higher computational cost.

Figure 4.12 shows the z -polarized electric field obtained using the full-wave simulation and the infinitesimal dipole model. Strong agreement is observed between the two solutions. The slight differences are because the model considers a finite number of infinitesimal dipoles while the full-wave simulation considers an incident plane wave that illuminates the entire space. In comparison to the 2D slab of randomly chosen dielectric layers where 40 additional current lines were added to account for the incident plane wave, the 3D lens required only 2 additional rings of infinitesimal dipoles (with no phase shift).

Figure 4.13 shows the Poynting vector profile over the designed focal point plane at $x = 4\lambda_0$ obtained using full-wave simulation (a) and using the infinitesimal dipoles model (b). The computation time was approximately 2.5 days using full-wave simulation of the 3D 8λ -diameter lens on a 4x8 core computer (2 GHz, RAM 255 GB), whereas the dipole model simulation time was approximately 2 hours on a 1x4 core computer (2.33 GHz, RAM 8 GB). The large RAM memory computer was needed to solve the 8λ lens because of the relatively electrically large dimensions needed for the computational box which should be sufficiently large to prevent any spurious reflections from the computational boundaries.

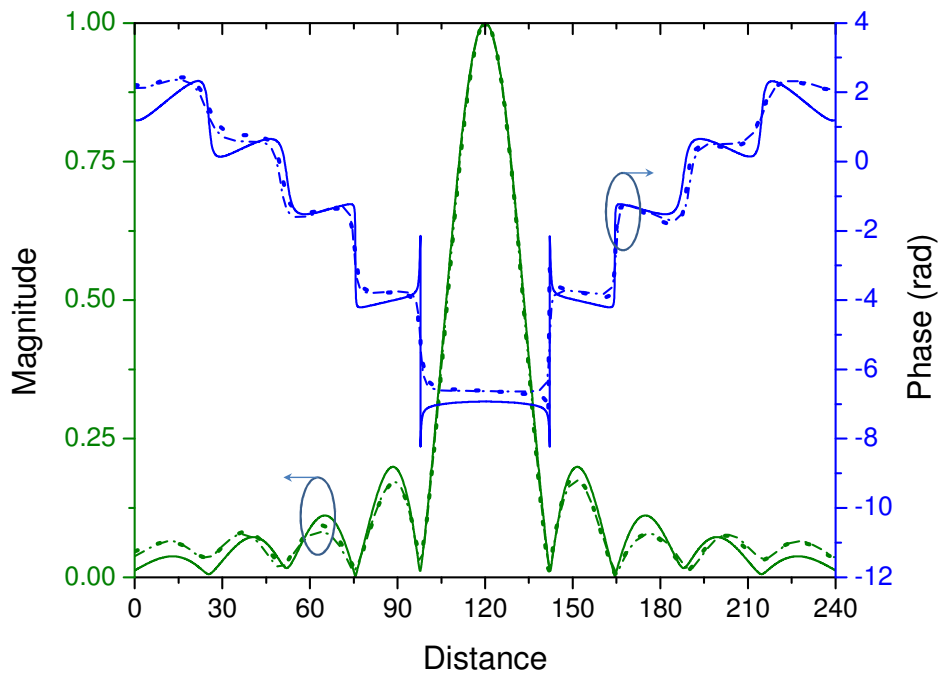


Figure 4.11: One-dimensional distribution of the normalized magnitude and phase of the electric field for a 8λ lens along a line parallel to the x-axis and at $x=3.1\lambda$ obtained using full wave simulation (solid line), dipole model employing 903 dipoles (dotted lines) and dipole model employing 4515 dipoles (dashed-dotted lines).

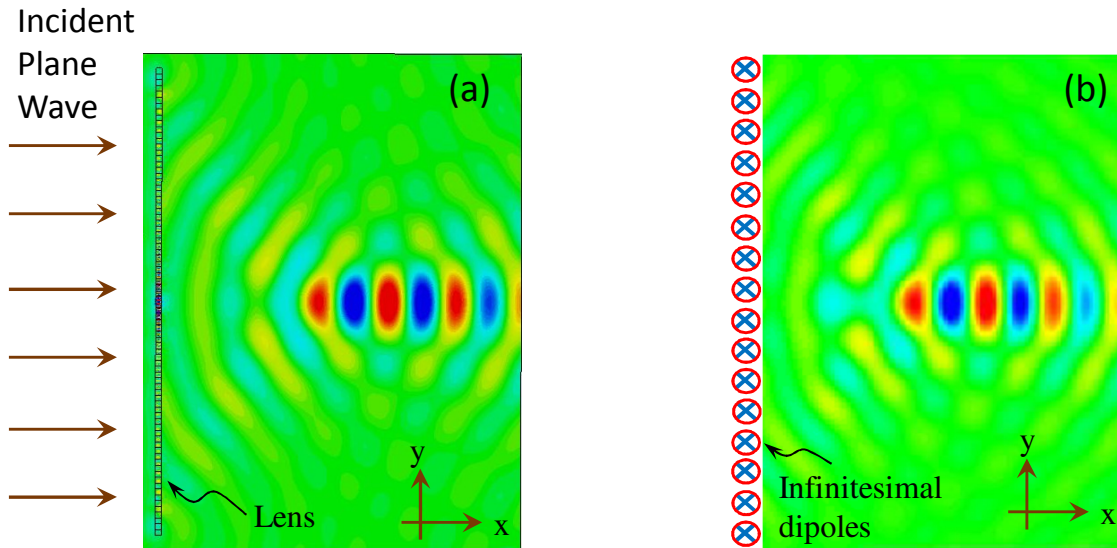


Figure 4.12: The z-polarized electric field for an 8λ electrically-thin 3D lens in the xy plane obtained using full-wave simulation (a) and the 3D infinitesimal dipoles model (b).

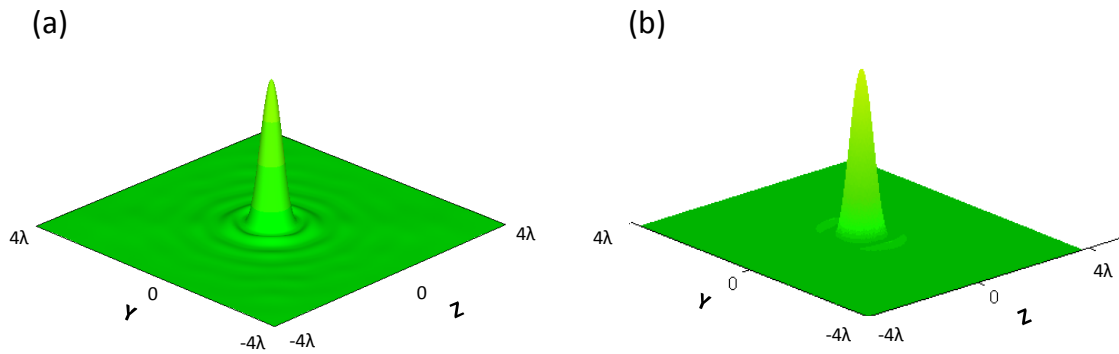


Figure 4.13: Magnitude of the normalized z-directed Poynting vector over the $x = 4\lambda_0$ plane. Using full-wave simulation (a), and using the 3D infinitesimal dipoles model (b).

4.5 Conclusion

An analytic model for a 2D and a 3D electrically thin inhomogeneous lenses and reflectors was presented. The effectiveness of the analytic models presented here is largely due to the fact that the lenses or reflectors are electrically thin which precludes any significant coupling between the dielectric layers comprising the lenses or reflectors. Several examples were presented to validate the analytic models. The advantages of the analytic models are twofold: First, flat lens or reflector design can be made possible without the need for expensive full-wave simulation tool, and, second, the analytic models provide highly efficient solution procedure that can be performed using widely available and inexpensive calculation libraries such as Matlab. In fact, the analytic models presented in this work can be highly effective for optimization of lens/reflector design.

Chapter 5

Spherical aberration in inhomogeneous lenses

5.1 Introduction

Historically, studies of lenses have focused on the quality of the image. Old and new applications of lenses continuously seek to improve imaging. Aberration of lenses, which results in blurry and distorted images, is a major concern in many applications[7, 8, 59, 60, 61, 62]. Traditionally, optical systems and improved fabrication techniques aim to minimize aberration and to increase focusing power.

Aberrations are defined as undesired image defects caused by non-converging rays at the focal point. These non-converging rays in terms of waves translate into non perfect spherical wave-fronts converging at a focal point.

Material dispersion of lenses at any optical system affects the refraction angle due to different phase velocities at different frequencies. As a result, different frequencies may have different focal points along the optical axis. This kind of distortion is named chromatic aberration (frequency band) [63]. In contrast, distortions corresponding to a single frequency are called monochromatic aberrations. Several applications such as professional cameras, typically decrease the chromatic aberrations by cascating a set of several convex and concave lenses. In this sense monochromatic aberrations are more challenging to address than that of the chromatic kind.

Primary monochromatic aberrations subdivides into spherical, coma, astigmatism, field curvature, and distortion. Special attention will be given to spherical aberration since a

complete analysis of this aberration for the electrically-thin lens is given in the following sections.

A complete analysis of monochromatic spherical aberration and a comparison of the electrically-thin flat lens and the classical GRIN rods is presented in this chapter.

5.2 Classical gradient index rods

More than a century ago, the father of electromagnetics, James Maxwell, proposed a spherical gradient index (GRIN) lens with the gradient in the radial direction [36]. The performance of Maxwell's design has been debated extensively [37]. Subwavelength resolution in Maxwell's lens was claimed by Leonhardt [64] and contested by others [37]. In 1905, Wood proposed a radially gradient index rod [9]. Inspired by the desert mirage, Wood formulated a design equation similar to the thin convex lens equation. Although Wood claimed that the formulation was suitable for both paraxial and marginal rays, the simplifications and assumptions of his formulation constrained the problem to sources and images far from the lens. In spite of the image quality [65], the class of GRIN rods developed by Wood proved to be useful in a variety of applications including photocopiers, scanners [66], fiber optics [67] and endoscopy [60] among others.

In classical gradient index rods design, incident rays are assumed to enter and exit the lens at shallow angles whereas within the gradient index material the rays are assumed to follow a circular trajectory as shown in figure 5.1. This trajectory is described by a radius r , an angle θ and an arc length s . The first approximation performed by Wood in his design formulation is given by,

$$\theta = \frac{s}{r} \approx \frac{d}{r} \quad (5.1)$$

Here, the validity of the approximation depends on the curvature of the trajectory. For cases where the curvature is comparable to the thickness of the rod the approximation holds. This approximation is used to find a relation between β and γ by applying simple geometry for triangles (see inset figure 5.1),

$$\theta = 180 - (90 - \beta) - (90 - \gamma) \quad (5.2)$$

Making use of approximation (5.1) the ray angles of the circular trajectory at the boundaries can be related by,

$$\gamma = \frac{d}{r} - \beta \quad (5.3)$$

In order to relate the angles of the ray within the rod with those outside the rod (at the boundaries), Snell law is applied. Although Snell law is valid only for homogeneous interfaces, as discussed on Chapter 2, Wood assumes that the slope of the refractive index on the lens is almost zero (small refractive index variation along electrically comparable distances of x) such that it may be considered to be locally homogeneous for incident rays.

$$\frac{\sin \alpha}{\sin \beta} = \frac{n}{n_0} \quad (5.4)$$

$$\frac{\sin \delta}{\sin \gamma} = \frac{n}{n_0} \quad (5.5)$$

where $n_0 = 1$ is the refractive index of free space.

Furthermore, another approximation is made by assuming that the rays enter and exit the lens at shallow angles such that the small angle approximation holds,

$$\sin(\beta) \approx \beta \quad (5.6)$$

$$\beta = \frac{\alpha}{n} \quad (5.7)$$

$$\gamma = \frac{\delta}{n} \quad (5.8)$$

This approximation limits the use of the formulation since the source and focal point have to be at a large distance compared to the radius of the lens. Combining equations (5.3), (5.7) and (5.8),

$$\delta = \frac{x}{f_2} = \frac{nd}{r} - \alpha = \frac{nd}{r} - \frac{x}{f_1} \quad (5.9)$$

Finally the formulation leads to a relationship similar to the curved lens equation,

$$\frac{x}{f_1} + \frac{x}{f_2} = \frac{nd}{r} \quad (5.10)$$

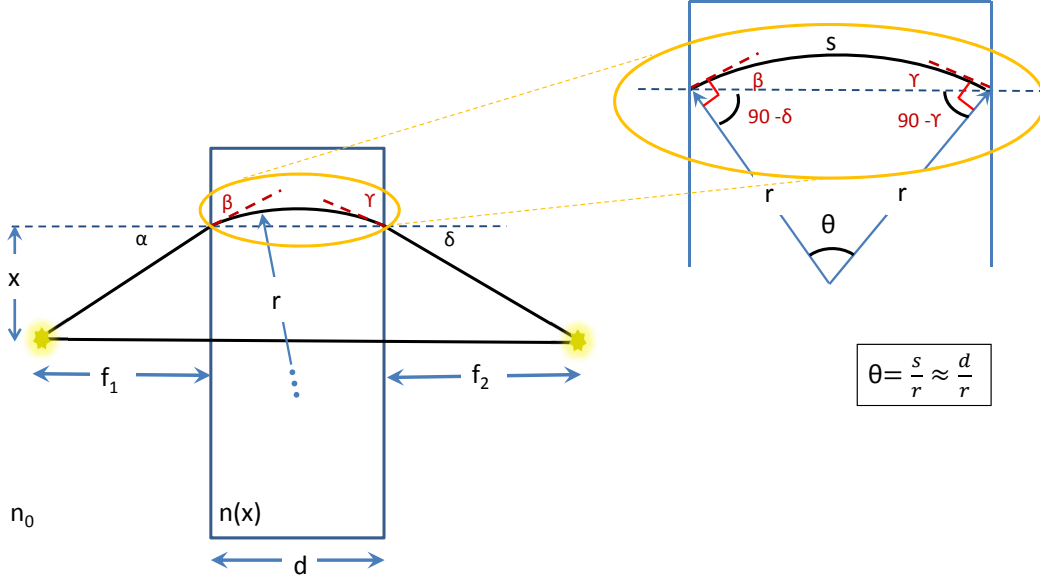


Figure 5.1: Gradient index (GRIN) lenses schematic.

In order to substitute r for a known variable, two closely spaced curved trajectories are considered and they are related by the radius of the curves and the corresponding phase velocities,

$$\frac{r}{r + dx} = \frac{v}{v'} = \frac{n + dn}{n} \quad (5.11)$$

where v is the phase velocity for the curve of radius r and v' is the phase velocity for the curve of radius $r + dx$. Notice that phase velocity is inversely proportional to the refractive index.

Then, the variation of the refractive index with respect to the radial distance is,

$$r dn = -n dx \quad (5.12)$$

This refractive index can be modeled as a polynomial of infinite order, as follows,

$$n = f(x) = n_1 + c_2 x + c_3 x^2 + c_4 x^3 + \dots \quad (5.13)$$

where n_1 corresponds to the refractive index at the axis. By symmetry (with respect to x), $c_2 = 0$, $c_4 = 0$, and so on, for the odd exponents.

As a first degree approximation, the refractive index may be expressed as,

$$n = f(x) = n_1 + c_3x^2 \quad (5.14)$$

The derivative of equation (5.14) corresponds to,

$$\frac{dn}{dx} = 2xc_3 \quad (5.15)$$

Substituting equation (5.12) in (5.10) and then using equation (5.15) ,

$$\frac{x}{f_1} + \frac{x}{f_2} = -d \frac{dn}{dx} = -2xc_3d \quad (5.16)$$

Since c_3 and d are constants, the equation can be compared to the thin convex lens' design equation of classical optics. Dividing by x on both sides of the equal sign and comparing to the thin convex lens equation,

$$\frac{1}{f_1} + \frac{1}{f_2} = \frac{-dn}{dx} \frac{d}{x} = \frac{1}{p} \quad (5.17)$$

where p corresponds to the focal length

From this relation, the right hand side (to the right of the second equal sign) and center term (between the two equal signs) of equation (5.17) can be integrated,

$$pnd = -\frac{x^2}{2} + n_1 \quad (5.18)$$

where n_1 is the constant of the integration and corresponds to the refractive index of the center of the lens as mentioned earlier.

$$n = -\frac{x^2}{2pd} + n_1 \quad (5.19)$$

It is worth mentioning that the author in [9] attempts to extend his work to a lens where the rays impinge on at large angles ("rays farther removed from the axis," [9]). However, his reasoning is problematic. He turned to equation 5.17. The problem here is that equation 5.17 was based on the approximation $\sin \beta \approx \beta$. This is a fundamental flaw in the derivation and the conclusion. In other words, Woods formula (equation 5.17) does not hold for any value of x but rather small incident and transmitted angles.

5.3 Spherical aberration

The image of a point source with aberration is usually a bright dot surrounded by a halo of light with lower contrast and higher blurriness when compared to the non-aberrated image. Spherical aberration can be defined as the variation of focus with aperture [68]. Figure 5.2 shows a schematic of a point source situated on the optical axis at a distance s to the convex surface. Formally, the analytical definition of on-axis spherical aberration is given by [69],

$$a(Q) = (PQI - POI) = (ln_0 + l'n_1) - (sn_0 + s'n_1) \quad (5.20)$$

where PQI and POI are optical paths from the source to the focal point. Aberration in a ray happens when $a(Q) \neq 0$. Strong aberration comes from having many rays with $a(Q) \neq 0$. Rays close to the optical axis converge into the so-called paraxial (rays within close proximity to the axis) focus (see figure 5.3). Typically, in classical convex lenses the distance between the paraxial focus and the intersection of an incident ray with the optical axis increases as the height of such ray increases.

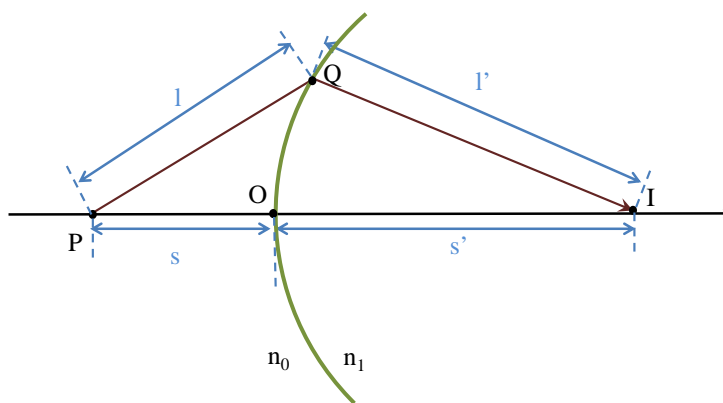


Figure 5.2: Spherical aberration definition schematic.

One of the most commonly used tools to analyze aberration is ray tracing technique [70]. In ray tracing, several rays are traced from the source, passing through the optical system to finalize at the image. Given that the magnitude of the aberration is related to the height of the ray in convex lenses, it is convenient to relate these two variables, such that the contribution of marginal (rays close to the margin or edge of the lens) and

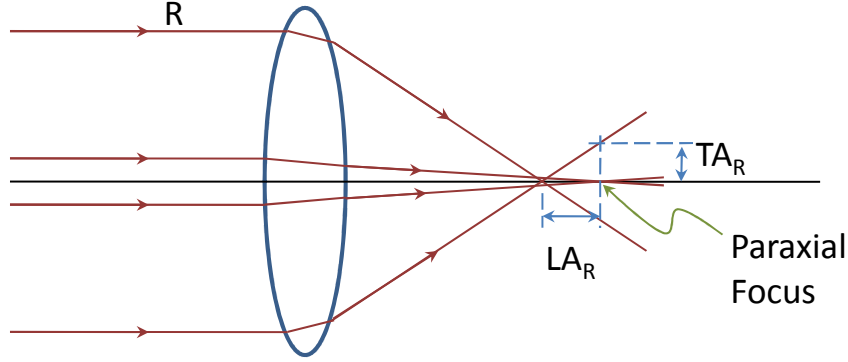


Figure 5.3: Longitudinal and transverse aberrations.

paraxial rays to aberration may be determined. This relation may be obtained by plotting the longitudinal (LA) and transverse aberrations (TA). Longitudinal aberration refers to the distance between the intersection of the ray with the optical axis and the paraxial focus, whereas transverse aberration refers to the distance between the intersection of the ray with the paraxial plane and the paraxial focus (see figure 5.3).

Aberration can also be analyzed and quantified in terms of the converging phase front by determining the optical path difference (OPD). Fig 5.4 shows the schematic of a converging wave front (solid line) obtained from an optical system and a perfectly spherical wave front used as a reference sphere. The OPD is the radial shift from the focal point given by the distance between the wave front and the reference sphere. The function that relates the OPD to the angle α , or height Y , is the wave aberration function (WAV). The root mean squared (RMS) WAV value is commonly used as a parameter to determine the quality of a lens [61, 67, 71]. This RMS value is particularly suitable for abrupt irregular wave fronts. WAV_{RMS} is defined as [61],

$$WAV_{RMS} = \langle WAV \rangle^2 - \langle WAV^2 \rangle \quad (5.21)$$

The wave nature of light limits the quality of the image that can be obtained due to diffraction. It is worth noticing that a perfect lens does not necessarily lead to a perfect image. An image is formed by the convergence of a wave and not the perfect convergence of rays. The ray model is simplification of the real physics that although it has proven its usefulness, it cannot fully describe the physics. For instance, the finite dimension of

a lens leads to a diffraction pattern which cannot be described by the ray model. This pattern is formed by an Airy disk (central bright point in the diffraction pattern) and a few noticeable surrounding rings. The difference of aberrated and non-aberrated images rests in the contrast of the Airy disk with its zeros (dark rings) and the brightness of the surrounding rings. For the case of a perfect lens, 84% of its energy is concentrated within the Airy disk [67].

In order to evaluate the overall quality of the image a criterion must be defined. As mentioned above, diffraction establishes a limit to the performance of a perfect lens. Therefore, a criterion can be defined based on the best resolution that two image points are said to be resolved limited by diffraction (the optical system in this case is comprised of two sources, one lens and the resulting two images). Each image point has its own Airy disc and surrounding rings that interfere with each other as they move closer. If they move close enough the images can only be resolved as one. The most commonly used standard for resolution is the Rayleigh Criterion that states the separation between the two maximums. (see figure 5.5).

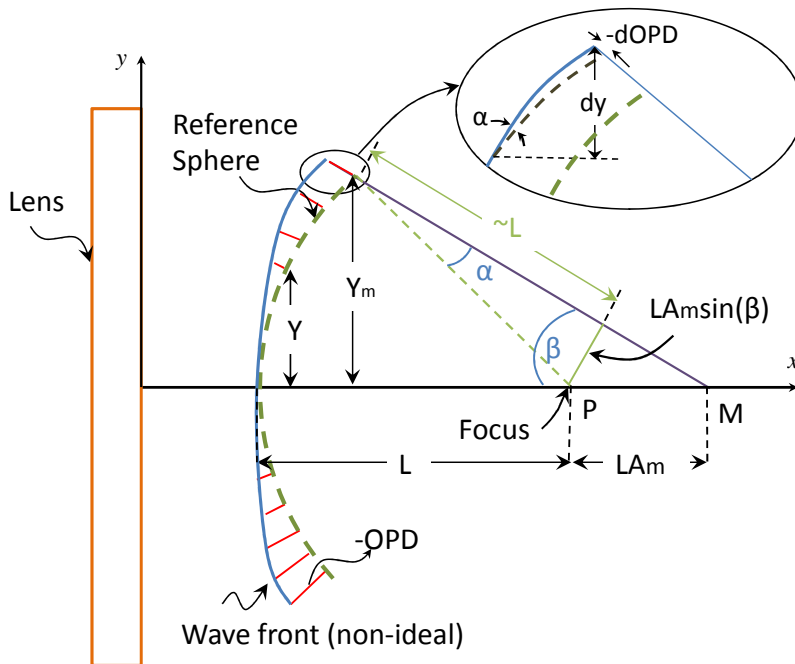


Figure 5.4: Optical path difference (OPD) in spherical aberration. M is the marginal focal point and LA is the longitudinal aberration.

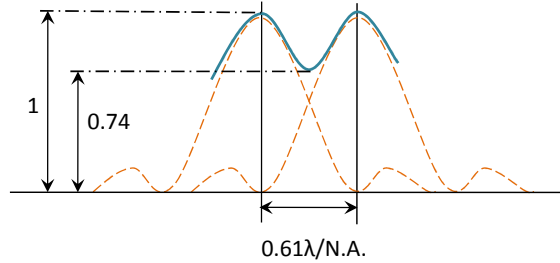


Figure 5.5: Normalized resolution schematic of Raileigh criterion. The individual images are depicted by the dashed orange lines. Solid blue line indicates the interference of the combined diffraction pattern. N.A. stands for Numerical Aperture and represents the ratio of the focal length over the diameter of the lens.

P-V OPD	WAV_{RMS}	Energy % in Airy disk
0.0	0.0	84
$\lambda/16$	0.018λ	83
$\lambda/4$	0.07λ	68

Table 5.1: Optical Path Difference relationship with WAV_{RMS} and Energy percentage in the Airy disk[67]

Under this parameters, the Rayleigh criterion for one image point allows not more than $\lambda/4$ peak-valley (P-V) OPD variation on the wavefront, such that the image is "sensibly" perfect. This $\lambda/4$ OPD variation corresponds to an Airy disk with an energy of 68 percent (see Table 5.1). Marechal criterion which is the Rayleigh limit for defocusing, states that $WAV_{RMS} < \lambda/14$ ($\approx 0.07\lambda$) leads to a small but appreciable amount of aberration (see equation 5.21). Here, the dominant term is diffraction. Then, for most applications the aberration is considered insignificant at this limit [61, 67].

5.3.1 Optical path difference (OPD) analysis

In order to evaluate the electrically-thin flat lens spherical aberration performance and to compare it with the classical GRIN rod lens, two lenses were designed. An 8λ diameter lens for each class of the two lenses considered here was designed comprising 40 concentric rings for each one. The rings have a radial thickness of $\lambda/10$. The length d of the thin

lens was $\lambda/10$ whereas the length d of the rod was 2λ (commercially available thick rods have much larger dimensions; however, because of computational limitations, in particular computer memory, the lenses designed here were limited to a thickness of 2λ and a diameter of 8λ . For the purpose of analysis, the lens was still considered electrically thick). Figure 5.6 shows the design of an electrically-thin flat lens (solid line) and a GRIN rod (dashed line). The profiles were obtained through equations (3.2) and (5.19) for the respective cases. Both lenses were designed to have a focal point 4λ from the surface of the lens at the rays exit side.

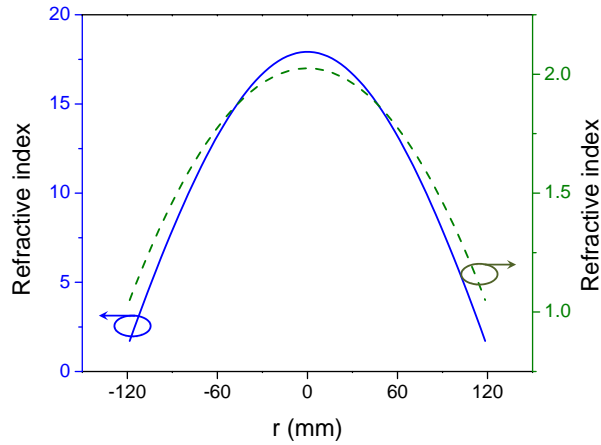


Figure 5.6: Solid line design of the refractive index for the electrically-thin lens, and dashed line the classical gradient index rod.

Notice that the thickness of the lens is electrically small (i.e., $d \ll \lambda$), which leads to minimal coupling between layers [72, 73]. Hence, aberrations are expected to be small and the designed focal point to be highly accurate for both paraxial and marginal rays [67]. I anticipate the sources of aberration to be the discretization of the gradient index and the non-zero coupling between adjacent dielectric layers (in addition another source of aberrations can be caused by fabrication tolerance limitations.) The profile for the electrically-thin lens extends from a refractive index of $n=1$ to 18. Notice that the design equation has some degrees of freedom that can decrease the refractive index if needed by changing the thickness or the focal point. In fact, a lens with the highest refractive index of $n=12.85$ was fabricated and tested at microwave frequencies using commercially available dielectric material typically used for printed circuit boards (see Section (3.4)). Recent advances in materials lead us to foresee the implementation of such lenses in higher frequency regimes [74]. Although, metamaterials are good candidates for engineering dielectrics that

are not readily available, their narrow bandwidth and high losses preclude their practical use [75].

In contrast, the classical gradient index (GRIN) rod is electrically-thick, designed by considering a number of important assumptions that can generate aberrations. First, the rays are considered to impinge on the lens from shallow angles so that the small angle approximation holds (see [9], pages 86-89). Therefore, the focal point and source should be far from the rod, contrary to the statement concluded in [9] where all rays are designed with the same approximation and claimed to be valid at any incident angle. Second, the incident and transmitted rays follow Snell law at both boundaries of the rod (see figure 5.1), which means that the rod is considered to be locally homogeneous. Consequently, the gradient refractive index should be sufficiently shallow to satisfy the local homogeneity condition such that Snell law results in refraction where the rays exit with an angle different from the incident one. Third, it is assumed that the rays within the rod follow a curve as shown in figure 5.1.

The two lenses were modeled and simulated using the full-wave three-dimensional modeling software CST MICROWAVE STUDIO (CST MWS) [50]. Figs. 5.7 and 5.8 show the \hat{z} directed electric fields of the electrically-thin lens and GRIN rod, respectively, in isoline format for easy recognition of the wave fronts. The reference spherical wavefront is also depicted on the figures for qualitative comparison.

I observe that the wavefront of the thin lens and the reference sphere are overlapping over most of the curve, whereas the wavefront of the GRIN rod differs from the reference sphere significantly. From these extracted results, the WAV_{RMS} is found to be $WAV_{RMS} \approx \frac{\lambda}{40}$ for the thin lens and $WAV_{RMS} \approx \frac{6\lambda}{10}$ for the GRIN rod. According to Marechal criterion, the spherical aberration arising from the thin lens is minimal whereas the aberration due to the GRIN rod is significant. Figure 5.9 shows a plot of the OPD as a function of the distance from the center of the lens for the electrically-thin lens and the GRIN rod. The deviation from the perfect spherical wavefront (OPD=0 mm) is clearly much larger for the rod than the thin lens.

5.3.2 Third-order aberration

Ray tracing is another method commonly used to calculate aberrations where aberrations are determined by the deviation of the rays from the paraxial image point [76]. Aberration polynomials are analytical equations based on the ray trajectory used to determine the coordinates of a ray in the image surface [67].

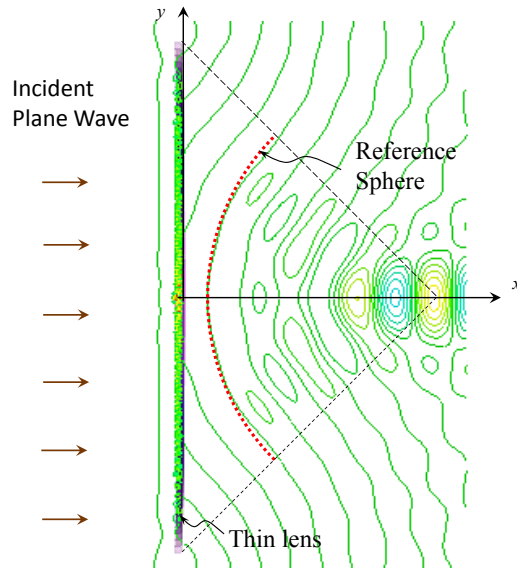


Figure 5.7: Cross section of the electric field (isoline format) of the electrically-thin lens. The lens wavefront is shown in solid lines and the reference spherical wavefront in dotted line.

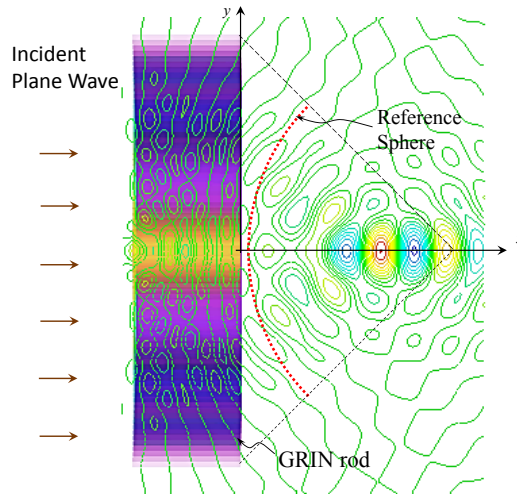


Figure 5.8: Cross section of the electric field (isoline format) of the rod. The lens wavefront is shown in solid lines and the reference spherical wavefront in dotted line.

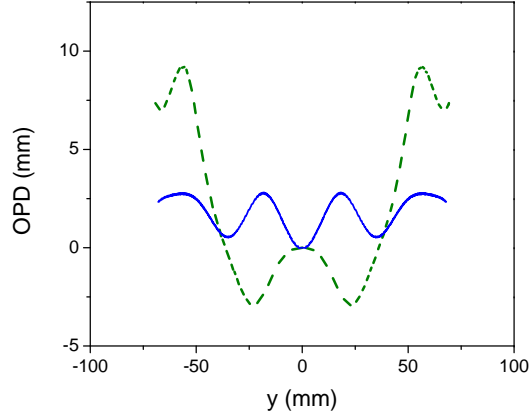


Figure 5.9: Optical path difference (OPD) as a function of the distance from the center of the lens. The solid line corresponds to the electrically-thin lens. The dashed line corresponds to the GRIN rod. (To extract the OPD, the phase in the proximity of the first zero phase wavefront immediately after the lens was computed from the numerical simulation. Since the discretized values were not exactly zero, the values were rounded and selected by a Matlab code that classified the rounded zero phase coordinates of every point on the zero phase wavefront.)

In many optical applications, the spherical aberration is dominated by the third-order term of the polynomial. The effect of the third order spherical aberration can be visualized by plotting the longitudinal aberration (LA) which corresponds to the distance between the intersection of the converging rays with the optical axis and the focal point. This term can be found by representing LA as a series[67],

$$LA = aY^2 + bY^4 + cY^6 \dots \quad (5.22)$$

where $a = \frac{LA_m}{Y_m^2}$ and $b = c = \dots = 0$ for the third order term. Additionally, the longitudinal aberration at the edge of the aperture is derived by finding the angle α (see figure 5.4),

$$\alpha = \frac{(LA_m)\sin(\beta)}{L} \quad (5.23)$$

From the inset of figure 5.4 that corresponds to a zoom of the indicated area the following relationship is found,

$$\alpha = \frac{(LA_m)\sin(\beta)}{L} \quad (5.24)$$

Then, combining equation 5.23 and 5.24 and solving for LA_m ,

$$LA_m = \frac{1}{\sin(\alpha)/L} \frac{dOPD}{dY} \quad (5.25)$$

Third-order longitudinal aberration was found by applying equation (5.25) to the OPD results (figure 5.9), LA_m was calculated to plot equation (5.24). Figure 5.10 shows the longitudinal aberration of the electrically-thin lens and the GRIN rod. Clearly, the electrically-thin lens has a superior performance. It is important to notice that this longitudinal aberration is calculated considering the designed focal point P as the reference point. However, this focal point might not be the location of highest concentration of rays along the optical axis. If another reference point was chosen, the OPD could be improved possibly leading to a decrease in the spherical aberration. The difference between the reference point and the actual focal point is typically referred to as the defocusing of the system. The third-order OPD with defocusing of δ is given by [67],

$$OPD = \frac{1}{2}n\sin^2(\alpha) \left[\delta - \frac{1}{2}LA_m \left(\frac{Y}{Y_m} \right)^2 \right] \quad (5.26)$$

where n is the refractive index of the medium where the image is reconstructed (vacuum or free-space in this work). By minimizing the RMS value of equation (5.21), δ is found to be $\delta = 4.111mm$ for the electrically-thin lens and $\delta = -28.1mm$ for the GRIN rod. Clearly, the magnitude of the defocusing is much smaller in the thin lens than the GRIN rod. Figure 5.11 shows the third-order OPD and LA for defocusing of δ as a reference point. Even at the defocusing point the thin lens shows minimal aberration.

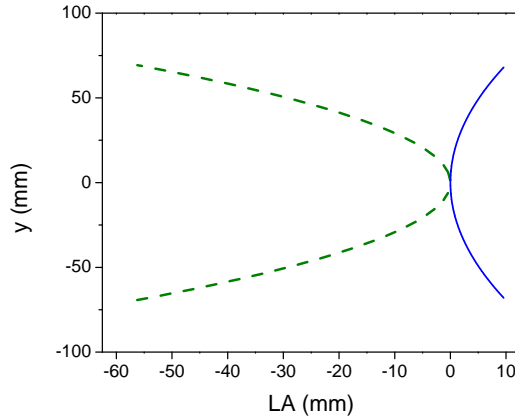


Figure 5.10: Y as a function of the longitudinal aberration (LA). Solid blue line corresponds to the electrically-thin lens. Dashed green line corresponds to the GRIN rod.

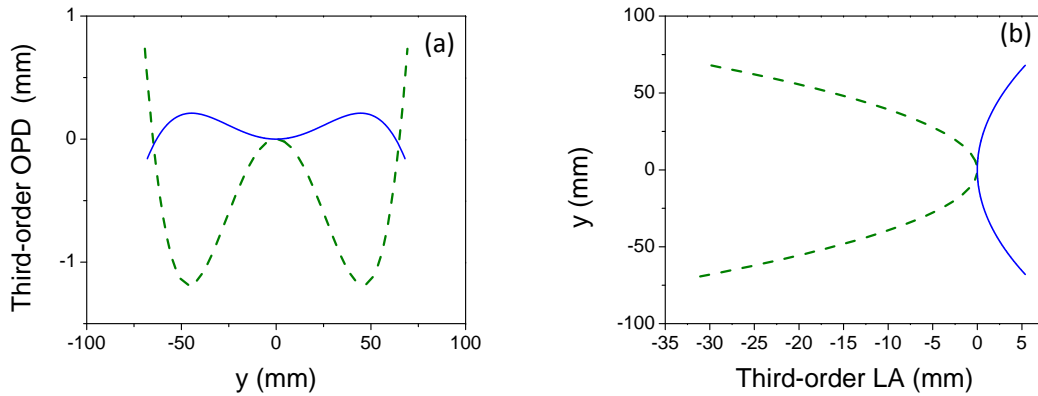


Figure 5.11: Third-order OPD with defocusing (a). Third order LA with defocusing (b). Solid blue line corresponds to the electrically-thin lens. Dashed green line corresponds to the GRIN rod. The plots were produced using the format used in [67].

5.4 Conclusions

The design of electrically-thin flat lenses aims to minimize spherical aberration by equalizing all paths from the source to the focal point. A spherical aberration analysis of the electrically-thin lens is presented here and compared to that of the classical GRIN rod. Appreciable difference in aberration was found between the two designs. One of the reasons for the poor performance of the GRIN rod is the use of small angle approximations. Although the design of the GRIN rod was derived for small angles, the rod equation was generalized to larger angles which leads to higher errors. In the GRIN rod design, the cases where a focal point and/or a source are close to the lens, the aberration due to marginal rays increases significantly. Therefore, the GRIN rod design equation proved to be inaccurate for large numerical apertures. Furthermore, Snell law was used by Wood to formulate the design equation of the GRIN rod. Snell law, however, cannot explain refraction when plane waves are incident perpendicularly. Specifically, for zero angle of incidence, Snell law predicts that the rays would exit the lens at zero angle. The reason for this contradiction is that Wood used Snell law as another approximation which again deteriorates the resulting image. For the electrically-thin lens, Snell law is not applicable to predict refraction since the medium is locally inhomogeneous. A more robust formulation that predicts refraction from inhomogeneous electrically-thin lenses is based on Huygens principle [77].

The WAV_{RMS} values quantifies the amount of spherical aberration. For the thin lens, WAV_{RMS} was lower than the Marechal criterion, thus its aberration was due mostly to diffraction. On the other hand, the GRIN rod exceeds the Marechal limit significantly, which means that diffraction has small contribution to the GRIN rod spherical aberration. Instead, other factors such as design approximations, simplifications and coupling between rings lead to a distorted and blurry image. The OPD and LA plots are consistent with the WAV_{RMS} value. Although, a decrease in aberration can be achieved by setting the defocusing as a reference, the GRIN rod maintains higher aberration than the thin lens.

Chapter 6

Monostatic cloaking

6.1 Introduction

For decades, popular culture and scientific community have been fascinated with cloaking devices for diverse applications. However, several challenges have prevented the realization of a practical device. Early research included studies on several geometrical shapes with and without dielectric coatings to decrease the Radar Cross Section (RCS) for struts. Although the RCS was improved, this stealth technology is still limited by the shapes, orientation of the materials with respect to the incident wave, polarization and electrical dimensions [78]. Transformation optics (TO) is probably the most noteworthy work on the subject [31, 32, 33, 34]. More than a decade ago, TO opened the possibility of tailoring electromagnetic fields at will. TO is based on Maxwell equations' coordinate system invariance. A Jacobian matrix relating the virtual and the physical domains leads to the transformation from which the permittivity and permeability values are calculated. TO have been applied to an important number of applications, including sensors [79], radar targets [80] and even sound waves [81]. More recently, an invisibility cloak based on complementary media was conceived to cloak objects outside the cloaking shell [82]. Nevertheless, the resulting design of the cloaking devices, whether they were designed using complementary media or not, were anisotropic and typically the design required close to zero permittivity components. With these values in mind, the initial implementations of the cloaking devices were constructed using metamaterials. The performance, however; is limited by losses and reflections of the metallic resonant structures. Furthermore, the bandwidth of such structures is narrow.

Given the challenges posed by metamaterials, many researchers have proposed different

alternatives. For instance, cloaks with homogeneous isotropic concentric (electrically thin) cylinders were designed to achieve an anisotropic behaviour that can be used to build a cloaking device [83]. Although, the design complexity is greatly reduced, every other cylinder must have a permittivity smaller than one. This implies that metamaterials or materials like silver should be used in the resonance region to achieve such requirement.

Recently, relaxations to classical cloaking approach were proposed by including amplitude-only cloaking devices. "L" shape cloaking devices, Fresnel lenses and mirror arrangements were explored [84]. Although these solutions provide cloaking, most of these solutions are bulky and the images become degraded in terms of quality and/or size. Therefore, these solutions are not practical in terms of use. More recently, paraxial ray optics cloaking was proposed [85]. This group succeeded in cloaking objects for an optical wide band using off-the-shelf lenses. The environment behind the object was reconstructed using a set of aligned lenses, whereas the cloaked region was defined around the focal points and intermediate lenses of the system. Aberrations and unwanted marginal rays in a paraxial design are among the challenges that this unidirectional system experience.

In order to increase the bandwidth of cloaking devices in the microwave range, a set of plates closely matched to free space were proposed [86, 87]. The conducting plates guided the waves around the object to be hidden. The geometry of the plates lead the wave to propagate around a central opening, hiding the object. This geometry; however, is complex and bulky.

Gradient index (GRIN) materials have also been used for cloaking. They were first proposed for "under the carpet" cloaking applications [88]. Then, broadband GRIN rods were used to hide objects around the focal point [89, 90], which is not practical in some cases.

It is important to notice that efforts have been focused on reducing both monostatic and bistatic cases. In the monostatic case, the object is invisible from the source. In other words, the monostatic setting involves a source that illuminates the cloaking device which in principle would appear as a dark spot for an observer at the same location of the source. Even if other objects are located behind the cloaked object, none of them would be detected. On the other hand, the bistatic case implies that the object is invisible for an observer at any point in space. Therefore, a wave traversing a perfect cloaking device should remain intact, which means that no reflections or losses should be noticed in any direction.

In this work, an arrangement of materials that interfere to cloak an object for radar applications (monostatic setting) is used. The concept of using interference to tailor the electromagnetic fields using electrically-thin gradient index material for focusing was intro-

duced in the previous sections as well as in [72, 73, 91]. Refraction at those electrically-thin inhomogeneous lenses and reflectors agreed with the law of refraction for inhomogeneous media [77], leading to a better understanding of the physics that are used here. A linear gradient index to refract the rays with a predetermined angle for unidirectional cloaking is used. The wave is deviated and follows a trajectory determined by the refractive index profile. The cloaking devices are made of simple inexpensive dielectrics. In addition, I demonstrate the enhancement in performance through numerical simulations and show a promising bandwidth.

6.2 Design methodology

An electrically-thin gradient index material backed up by an electric conductor was designed in [72] to refract the rays into a focal point. In contrast, here I design a gradient index material to refract the rays from a perpendicularly incident wave into a fixed angle (see figure 6.1) such that the scattered field in the direction of the source is minimized. The orthogonal rays traverse the gradient index material twice due to the perfect electric conductor (PEC) on the back of the material. If the material is chosen to follow a linear gradient index along y -axis, then a linear phase profile is created at the exit surface of the device. This phase profile results in angled rays due to constructive interference, similar to a current sheet with varying phase. Figure 6.1 shows a perpendicularly incident plane wave illuminating a 2D reflector (layers infinite in x -direction). It can be noticed that the phase of the incident wave over the left side of the lens is the same for all layers. The path of each ray traversing on a roundtrip each refractive index and reaching the desired (designed) phase front have to be equal. Therefore, the design equation to refract such wave is as follows,

$$n_M d + n_0 h_M = n_m d + n_0 h_m \quad (6.1)$$

where n_M is the refractive index of the M-layer, n_0 is the vacuum refractive index, n_m is the refractive index of the m^{th} layer, $d/2$ is the thickness of the dielectrics, h_m is the distance from the m^{th} layer to the designed wave front and h_M is the distance from the layer-M to the designed wave front. Notice that the wave within each material is assumed to be confined. The reason for this consideration is due to the electrical thinness of the reflector which results in minimal coupling between layers.

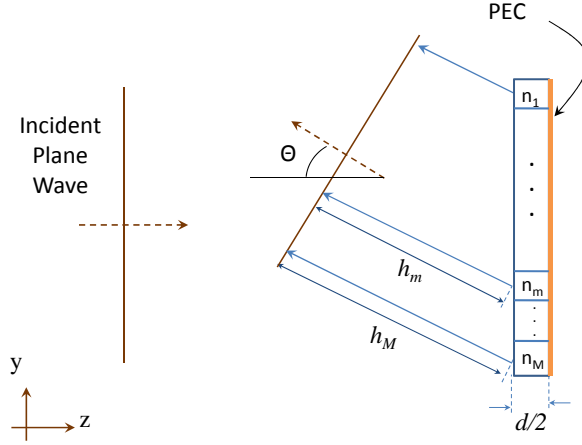


Figure 6.1: Constructive interference for an angled-refracted exiting wave over the electrically-thin flat reflector.

6.3 2D reflector

An example of a 3.5λ height, $d/2 = \lambda/20$ thick 2D-reflector composed of 35 layers was design to demonstrate that refraction of fixed angles can be used to minimize the scattered field that propagated towards the source once the wave reflects on the PEC. In the case presented here, the upper half gradient index of the reflector was designed to refract the wave with an 80 degree angle, whereas the lower half of the reflector was designed to refract the ray on a -80 degree angle. Figure 6.2 shows the design of the refractive index as a function of the $y - axis$.

Figure 6.3 shows the scattered electric field for an \hat{x} polarized incident electric field illuminating the reflector. The scattered field was obtained using the commercially available full wave numerical simulation software CST [50]. It is clear from the figure that the incident wave was splitted in two waves moving to the top and bottom of the device. The designed directions are indicated in the figure by arrows. While most power was scattered and dispersed towards the top and bottom of the reflector, the scattered field on the direction of the source was minimized to values close to zero in the far field. Figure 6.4 shows the Poynting vector of the total field. Clearly, the total power close to the reflector is deviated outwardly. Therefore, an important portion of the power is redirected around the cloaking device. Figure 6.4 shows how the scattered fields have no effect on the Poynting vector in the direction of the source.

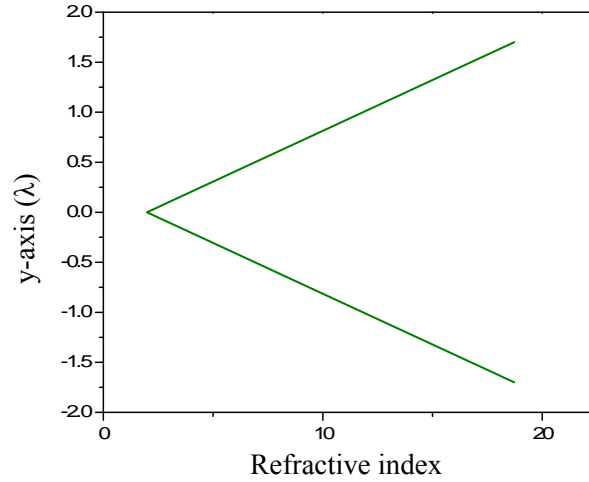


Figure 6.2: Design of the refractive index profile for a 2D cloaking device. The linear refractive index profile was designed for $\pm 80^\circ$ angle refraction.

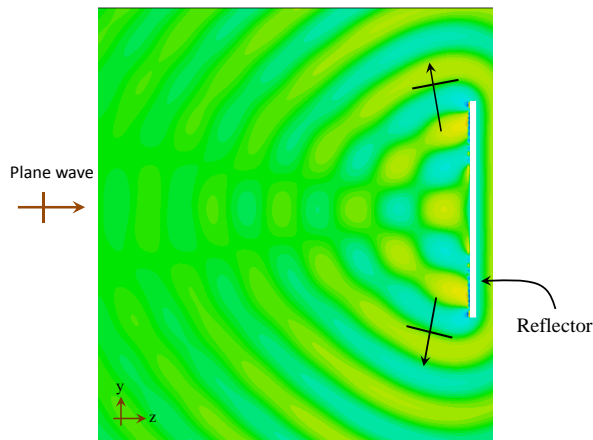


Figure 6.3: Scattered electric field for $\pm 80^\circ$ angle refraction design of a 2D reflector. The plane wave is polarized in the \hat{x} direction. Color scale extends from -10.7 V/m (deep blue) to 10.7 V/m (deep red).

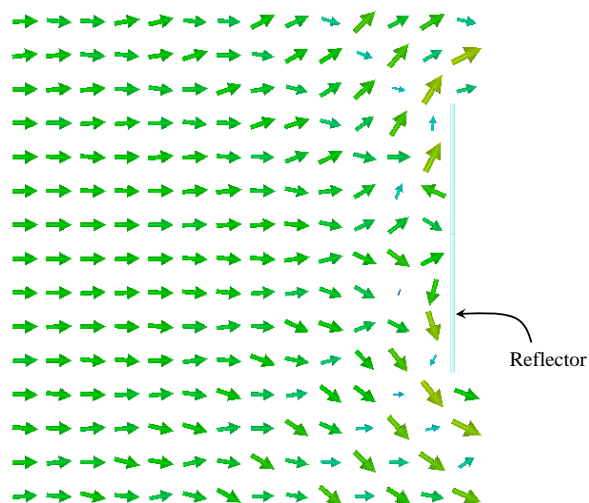


Figure 6.4: Poynting vector of the total field. The incident plane wave propagates from left to right. The left most arrows are almost perfectly horizontal. Although the scattered field is strong close to the reflector, the Poynting vector shows low reflections in the direction of the source.

6.4 3D reflector

Although, the 2D reflector concept showed promising results, the reflector has the limitation that it is polarization sensitive. Additionally, the design of the 2D reflector is meant to conceal long flat electric conductors with certain polarization. In order to address such inconvenience, the design of a squared reflector made of concentric annular squared rings (see figure 6.5) is presented. A PEC is placed on the back of the dielectric materials such that a plane wave impinges the reflector perpendicularly and the wave traverse the dielectrics and bounce back at the PEC.

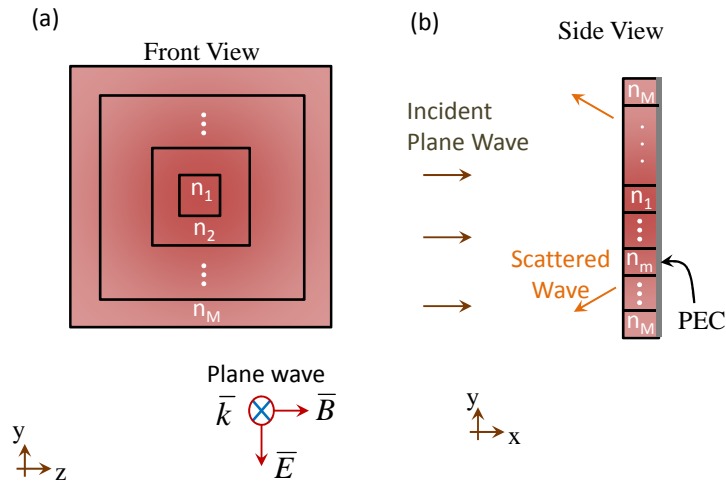


Figure 6.5: Electrically-thin flat reflector schematic front view (a). Side view (b).

The refractive index of the squared rings determine the phase front velocity as well as the phase at the exiting surface of each ring. As shown in figure 6.5(b), perpendicularly incident waves can be spread in different directions other than towards the source by properly designing the gradient index material. In the case of a unidirectional radar an insignificant fraction of power returns to the source.

The formulation (equation (6.1)) used to design the refracted angle of a 2D reflector can also be employed to design a (3D) reflector that is not sensitive to polarization. Considering a unidirectional cloak system, squared tales of gradient index material with electrically-thin concentric squares are proposed to account for any polarization. Figure 6.5 shows the schematic of the dual polarizable reflector for unidirectional cloaking. The intention with

the squared design is to have units of electrically-thin material that can cover any arbitrary electrically large geometry, such as airplanes.

The concept is validated with an example of a 2λ reflector made of 10-squared rings, $d/2 = \lambda/20$ thickness. The gradient index profile varies from 1 to 10 and it is designed according to equation (6.1) to have an angle close to ± 87 degrees with respect to the normal. The permittivity and permeability are chosen to be equal to minimize reflections in the first surface. Figure 6.6 shows results for the numerical simulation of the cloaking device concealing an electrically large PEC object ($2\lambda * 2\lambda * \lambda$). Figure 6.6(a) shows the total electric field with no cloaking device, whereas figure 6.6(b) shows the total electric field with the cloaking device. Clearly, the scattered field increases the total field in the direction of the source for the first case. For the second case, the reflected field in the direction of the source is minimal and the wave is redirected to the sides.

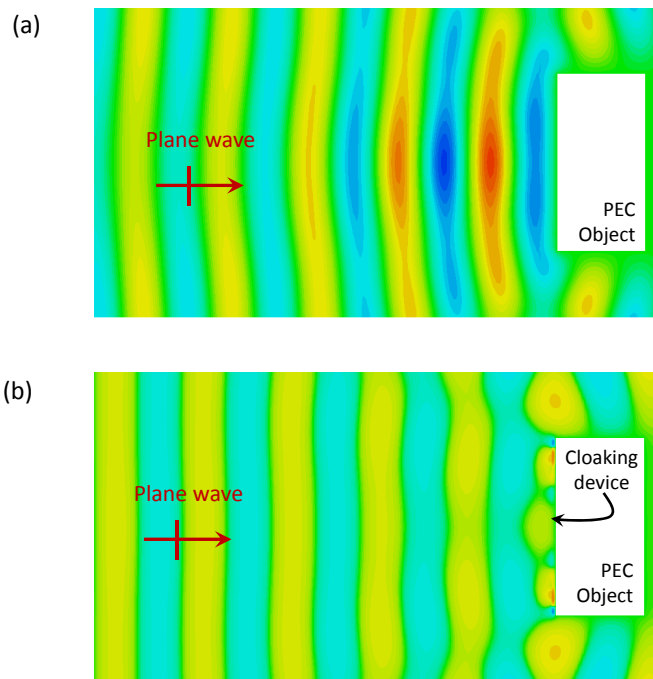


Figure 6.6: Total electric field of a 10 GHz plane wave perpendicularly incident to a PEC object (Color scale extends from $-2.59 V/m$ (deep blue) to $2.59 V/m$ (deep red)) (a). Total electric field of a plane wave perpendicularly incident to an electrically-thin cloaking (reflector) device concealing a PEC object (Color scale extends from $-20.5 V/m$ (deep blue) to $20.5 V/m$ (deep red)) (b).

The monostatic radar cross section (RCS) is plotted for both cases for frequencies between 9 GHz and 11 GHz (see figure 6.7). The best RCS was found at 10 GHz with an RCS difference of $-11dBm^2$. Figure 6.7 shows promising bandwidth for radar applications.

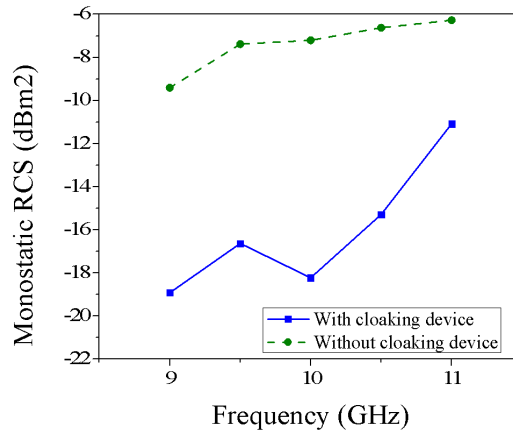


Figure 6.7: Monostatic radar cross section (RCS) of a PEC object with a cloaking device (solid blue line) and without a cloaking device (green dashed line).

6.5 Conclusion

Two designs for cloaking an electrically large object at microwave frequencies were presented. Typical cloaking applications implies expensive fabrication, geometry limitations of the object, high reflections or very narrow bandwidth. The designs are based on simple dielectric geometries and conductors which decreases costs significantly. Numerical simulations show low monostatic radar cross section and a promising bandwidth for the 3D reflector. The designs were inspired by the electrically-thin energy concentrators [72], where a phase profile can be designed to reflect the rays in the desired direction. The diverging ray cloak reflector can be envisioned as unit cell stickers or gradient index paint meant to be used in airplanes as a low cost solution.

Chapter 7

Conclusions

7.1 Contributions

The importance of Snell law is out of question. This simple equation have been a solid foundation over which a wide number of designs and optimizations are developed. However, Snell law is limited by cases where a wave travels between two homogeneous materials through a planar interface. Although, in many applications designers and researchers choose to use homogeneous materials for simplicity, recent advances in material science have led to a wider spectrum of materials broadening the possibilities in terms of applications and designs.

In this thesis, several applications and designs involving inhomogeneous materials were introduced. Here, an analytical solution based on simple boundary conditions and a carefully performed phase matching was developed to find a formulation that predicts refraction in electrically-thin flat inhomogeneous media. A wave with normal incidence to a planar electrically-thin inhomogeneous media should have a zero angle of refraction according to the classical formulation. However, as it was shown in several numerical examples and experiments, there is refraction. The formulation presented here predicts with high accuracy the refraction of rays in such materials.

Contribution on the law of refraction for electrically-thin inhomogeneous media was published in the Journal of the Optical Society of America A [77]. Also, this work was presented in the 2016 IEEE International Symposium on Antennas and Propagation and North American National Radio Science meeting (APS/URSI) [92].

In addition to this analytical formulation, an electrically-thin flat lens and reflector were proposed. An accurate and simple design formulation based on phase compensation

and Huygens principle were presented. Both designs showed high energy concentration while yielding insignificant spherical monochromatic aberration.

Contribution on the design methodology and numerical validation of flat lenses and reflectors was published in the journal Progress on Electromagnetic Research Symposium (PIERS)[72]. Also, this work was presented in the 2013 IEEE International Symposium on Antennas and Propagation and North American National Radio Science meeting (APS/URSI)[93] and the 2013 Mediterranean Microwave Symposium [73].

An analysis based on the wave aberration function (WAV_{RMS}) and optical path difference was performed. The electrically-thin lens was demonstrated to have lower (WAV_{RMS}) than the Marechal criterion which means that most aberration in the image is due to diffraction. Hence, for most applications the lens can be considered spherical aberration free.

For a better evaluation and understanding of the lens performance, the electrically-thin flat lens was compared to the classical gradient index (GRIN) rod. The rod's design was proposed more than a hundred years ago. However, the gradient index rods are found in a number of modern applications including copy machines, fiber optics and even in endoscopy. In chapter 5, the electrically-thin lens provided better performance than the GRIN rod. Several assumptions and approximations in the GRIN rod design lead to aberrated images.

Contribution to aberration analysis was submitted to the Journal of the Optical Society of America A. To date, favorable comments were received from the reviewers and the final decision is pending.

Besides the electrically-thin lens and reflector for power concentration, an off-axis electrically-thin reflector and a cloaking device were presented. Both applications showed strong performance and viability for practical applications. This work is being prepared for submission to Applied Physics Letters.

An analytical model based on infinite current lines (for 2D flat lenses and reflectors) and on infinitesimally small dipoles (for 3D flat lenses and reflectors) were introduced. Both models were validated through numerical simulation and showed accurate results. Given that the models were based on current lines and small dipoles, the close resemblance in the results indicate that the coupling between dielectric layers is not significant for electrically-thin layers. In addition, the models allow to decrease the simulation time and computer resources significantly. This work was published in the Journal of the Optical Society of America A [73].

In addition to the numerical validation, an experiment was performed to further validate the quality of the lens and the reflector. A lens and a reflector were made of commercially

available low-loss dielectrics. Both devices were tested at microwave frequencies. The gain of the lens at the focal point with respect to the power at the same point with no lens was 4.2 dB, whereas the same gain for the reflector was 7.7 dB. Even though the dielectrics were not matched to free space, they showed an image pattern similar to the one obtained through simulation.

Also, using numerical simulation the electrically-thin lens and reflector had good performance as collimators. The far-field pattern showed an important gain in the direction of the device in the case of the lens (opposite to the device in the case of the reflector).

Contribution on the experimental validation of the electrically-thin lens and reflector and directivity enhancement through full-wave simulations were published in the Journal of the Optical Society of America A[91].

In summary, the electrically-thin flat lens and reflector were validated through analytical models, numerical simulations and experiments. Furthermore, the law of refraction for electrically-thin inhomogeneous media presented here provides a physical explanation for the refraction phenomena at planar interfaces for normally incident plane waves. A number of applications proved the versatility, usefulness and quality (very low spherical aberrated images) of the devices, including lenses, reflectors, off-axis reflectors and cloaking devices.

Chapter 8

Future directions

Several applications based on the same concepts and designs presented here could be developed. Some of the applications include hyperthermia, which is microwave heating of tissues for cancer treatments. Current devices use an array of (around) four dipole antennas to focus the power within the body. Given that the dipole radiates radially ($\hat{\rho}$), the power efficiency is not optimal. Using flat or even cylindrical lenses could improve not only the power efficiency but also reducing the area of power concentration to avoid heating healthy tissue.

Another application that can be developed is decoupling closely spaced antennas or transmission lines. In the case of a lens, the design is meant to focus the waves into a single point. Instead, an inhomogeneous media could be designed to spread the waves that propagate between sources, decreasing the power received between each other. The coupling between antennas or transmission lines could potentially decrease by properly design an inhomogeneous slab between them.

From the theoretical perspective, it would be interesting to explore the extension of the refraction formulation presented here. As mentioned through-out the thesis, the refraction formulation as well as the designs are valid under the assumption of the electrical thinness of the inhomogeneous media. Understanding the validity of these formulations in electrically thick (a few free-space wavelengths thick) inhomogeneous materials could expand the applications and even the working frequency regime.

From the experimental perspective, a lens in higher frequencies could be fabricated. Some groups [74] have developed high dielectric constant materials at infrared frequencies. A possible future direction would be to fabricate a film (lens) at higher frequencies for infrared cameras that could be used in military or even rescue mission applications.

References

- [1] F. Aieta, P. Genevet, M. A. Kats, N. Yu, R. Blanchard, Z. Gaburro, and F. Capasso. Aberration-free ultrathin flat lenses and axicons at telecom wavelengths based on plasmonic metasurfaces. *Nano Lett.*, 12(9):4932–4936, Aug 2012. doi: 10.1021/nl302516v. URL <http://dx.doi.org/10.1021/nl302516v>.
- [2] N. Yu, P. Genevet, M. A. Kats, F. Aieta, J. P. Tetienne, F. Capasso, and Z. Gaburro. Light propagation with phase discontinuities: Generalized laws of reflection and refraction. *Science*, 334(6054):333–337, Oct 2011. doi: 10.1126/science.1210713. URL <http://www.sciencemag.org/content/334/6054/333.abstract>.
- [3] X. Chen, L. Huang, H. Mühlenbernd, G. Li, B. Bai, Q. Tan, G. Jin, C. W. Qiu, S. Zhang, and T. Zentgraf. Dual-polarity plasmonic metalens for visible light. *Nat. Commun.*, 3:1198, Oct 2012. URL <http://dx.doi.org/10.1038/ncomms2207>.
- [4] N. Yu and F. Capasso. Flat optics with designer metasurfaces. *Nat. mater.*, 13(2): 139–150, Jan 2014. URL <http://dx.doi.org/10.1038/nmat3839>.
- [5] Z. B. Lakhdar M. Zghal, H. E. Bouali and H. Hamam. The first steps for learning optics: Ibn sahls, al-haythams and youngs works on refraction as typical examples. In *The Education and Training in Optics and Photonics Conference (ETOP) 2007*, Ottawa, Ontario, Canada, 2007.
- [6] H. C. King. *The History of the Telescope*. Courier Dover Publications, New York, first edition, 2003.
- [7] P. J. SANDS. Third-order aberrations of inhomogeneous lenses. *J. Opt. Soc. Am.*, 60(11):1436–1443, Nov 1970. doi: 10.1364/JOSA.60.001436. URL <http://www.opticsinfobase.org/abstract.cfm?URI=josa-60-11-1436>.

- [8] P. J. SANDS. Inhomogeneous lenses, iii. paraxial optics. *J. Opt. Soc. Am.*, 61(7):879–885, Jul 1971. doi: 10.1364/JOSA.61.000879. URL <http://www.opticsinfobase.org/abstract.cfm?URI=josa-61-7-879>.
- [9] R. W. Wood. *Physical optics*. The Macmillan Company, New York, second edition, 1911.
- [10] S. Larouche and D. R. Smith. Reconciliation of generalized refraction with diffraction theory. *Opt. Lett.*, 37(12):2391–2393, Jun 2012. doi: 10.1364/OL.37.002391. URL <http://ol.osa.org/abstract.cfm?URI=ol-37-12-2391>.
- [11] J. R. Egger. Use of fresnel lenses in optical systems: some advantages and limitations. In *Proceedings SPIE*, volume 193, page 63, 1979.
- [12] K. Miyamoto. The phase fresnel lens. *J. Opt. Soc. Am.*, 51(1):17–20, Jan 1961. doi: 10.1364/JOSA.51.000017. URL <http://www.opticsinfobase.org/abstract.cfm?URI=josa-51-1-17>.
- [13] A. Davis. Raytrace assisted analytical formulation of fresnel lens transmission efficiency, Aug 2009. URL <http://dx.doi.org/10.1117/12.823742>.
- [14] A. Davis and F. Kuhnlenz. Optical design using fresnel lenses. *Optik and Photonik*, 2(4):52–55, Dec 2007. doi: 10.1002/opph.201190287. URL <http://dx.doi.org/10.1002/opph.201190287>.
- [15] B. A. Anicin, V. M. Babovic, and D. M. Davidovic. Fresnel lenses. *Am. J. Phys.*, 57(4):312–316, June 1989. doi: <http://dx.doi.org/10.1119/1.16071>. URL <http://scitation.aip.org/content/aapt/journal/ajp/57/4/10.1119/1.16071>.
- [16] RALF LEUTZ, AKIO SUZUKI, ATSUSHI AKISAWA, and TAKAO KASHIWAGI. Design of a nonimaging fresnel lens for solar concentrators. *Solar Energy*, 65(6): 379 – 387, Nov 1999. doi: [http://dx.doi.org/10.1016/S0038-092X\(98\)00143-1](http://dx.doi.org/10.1016/S0038-092X(98)00143-1). URL <http://www.sciencedirect.com/science/article/pii/S0038092X98001431>.
- [17] D. N. Black and J. C. Wiltse. Millimeter-wave characteristics of phase-correcting fresnel zone plates. *IEEE Trans. Microw. Theory Tech.*, 35(12):1122–1129, Dec 1987. doi: 10.1109/TMTT.1987.1133826. URL http://ieeexplore.ieee.org/xpls/abs_all.jsp?arnumber=1133826.
- [18] M. Sussman. Elementary diffraction theory of zone plates. *Am. J. Phys*, 28(4):994–398, July 1960. doi: <http://dx.doi.org/10.1119/1.1935811>. URL <http://scitation.aip.org/content/aapt/journal/ajp/28/4/10.1119/1.1935811>.

- [19] H. D. Hristov. Terahertz harmonic operation of microwave fresnel zone plate lens and antenna: Frequency filtering and space resolution properties. *Int J Antennas Propag*, 2011:8, Sep 2011. doi: doi:10.1155/2011/541734. URL <http://dx.doi.org/10.1155/2011/541734>.
- [20] A. Petosa. Investigation on arrays of perforated dielectric fresnel lenses. *IEE Proceedings - Microwaves, Antennas and Propagation*, 153:270–276(6), June 2006. doi: 10.1049/ip-map:20050193. URL http://digital-library.theiet.org/content/journals/10.1049/ip-map_20050193.
- [21] J. B. Pendry. Negative refraction makes a perfect lens. *Phys. Rev. Lett.*, 85:3966–3969, Oct 2000. doi: 10.1103/PhysRevLett.85.3966. URL <http://link.aps.org/doi/10.1103/PhysRevLett.85.3966>.
- [22] J. M. Williams. Some problems with negative refraction. *Phys. Rev. Lett.*, 87 (physics/0105034):249703, Oct 2001. doi: 10.1103/PhysRevLett.87.249703. URL <http://link.aps.org/doi/10.1103/PhysRevLett.87.249703>.
- [23] J. Pendry. Pendry replies:. *Phys. Rev. Lett.*, 87:249702, Nov 2001. doi: 10.1103/PhysRevLett.87.249702. URL <http://link.aps.org/doi/10.1103/PhysRevLett.87.249702>.
- [24] P. M. Valanju and R. M. Walser and A. P. Valanju. Wave refraction in negative-index media: always positive and very inhomogeneous. *Phys. Rev. Lett.*, 88(18):187401, Apr 2002. doi: 10.1103/PhysRevLett.88.187401. URL <http://link.aps.org/doi/10.1103/PhysRevLett.88.187401>.
- [25] J. B. Pendry and D. R. Smith. Comment on ” wave refraction in negative-index media: Always positive and very inhomogeneous”. *Phys. Rev. Lett.*, 90:029703, Jan 2003. doi: 10.1103/PhysRevLett.90.029703. URL <http://link.aps.org/doi/10.1103/PhysRevLett.90.029703>.
- [26] G. W. Hooft. Comment on ”negative refraction makes a perfect lens”. *Phys. Rev. Lett.*, 87:249701, Nov 2001. doi: 10.1103/PhysRevLett.87.249701. URL <http://link.aps.org/doi/10.1103/PhysRevLett.87.249701>.
- [27] G. V. Eleftheriades, A. K. Iyer, and P. C. Kremer. Planar negative refractive index media using periodically l-c loaded transmission lines. *IEEE Trans. on Micro. Th. and Tech.*, 50(12):2702–2712, Dec 2002. doi: 10.1109/TMTT.2002.805197. URL http://ieeexplore.ieee.org/xpls/abs_all.jsp?arnumber=1097986.

- [28] S. M. Rudolph and A. Grbic. The design and performance of an isotropic negative-refractive-index metamaterial lens. In *General Assembly and Scientific Symposium, 2011 XXXth URSI, Istanbul, Turkey*, pages 1–4, Aug 13-20 2011. doi: 10.1109/URSIGASS.2011.6050637.
- [29] Z. Jacob, L. V. Alekseyev, and E. Narimanov. Optical hyperlens: Far-field imaging beyond the diffraction limit. *Opt. Express*, 14(18):8247–8256, Sep 2006. doi: 10.1364/OE.14.008247. URL <http://www.opticsexpress.org/abstract.cfm?URI=oe-14-18-8247>.
- [30] H. Lee, Z. Liu, Y. Xiong, C. Sun, and X. Zhang. Development of optical hyperlens for imaging below the diffraction limit. *Opt. Express*, 15(24):15886–15891, Nov 2007. doi: 10.1364/OE.15.015886. URL <http://www.opticsexpress.org/abstract.cfm?URI=oe-15-24-15886>.
- [31] S. A. Cummer, B. I. Popa, D. Schurig, D. R. Smith, and J. Pendry. Full-wave simulations of electromagnetic cloaking structures. *Phys. Rev. E*, 74:036621, Sep 2006. doi: 10.1103/PhysRevE.74.036621. URL <http://link.aps.org/doi/10.1103/PhysRevE.74.036621>.
- [32] M. Rahm, D. A. Roberts, J. B. Pendry, and D. R. Smith. Transformation-optical design of adaptive beam bends and beam expanders. *Opt. Express*, 16(15):11555–11567, July 2008. doi: 10.1364/OE.16.011555. URL <http://www.opticsexpress.org/abstract.cfm?URI=oe-16-15-11555>.
- [33] J. B. Pendry, D. Schurig, and D. R. Smith. Controlling electromagnetic fields. *Science*, 312(5781):1780–1782, June 2006. doi: 10.1126/science.1125907. URL <http://www.sciencemag.org/content/312/5781/1780.abstract>.
- [34] D. H. Kwon and D. H. Werner. Transformation optical designs for wave collimators, flat lenses and right-angle bends. *New J. Phys.*, 10(11):115023, Nov . doi: 10.1088. URL <http://stacks.iop.org/1367-2630/10/i=11/a=115023>.
- [35] X. Chen, H. Feng Ma, X. Ying Zou, W. Xiang Jiang, and T. Jun Cui. Three-dimensional broadband and high-directivity lens antenna made of metamaterials. *J. Appl. Phys*, 110(4):044904, Aug 2011. doi: <http://dx.doi.org/10.1063/1.3622596>. URL <http://scitation.aip.org/content/aip/journal/jap/110/4/10.1063/1.3622596>.

- [36] M. Born and E. Wolf. *Principles of optics: electromagnetic theory of propagation, interference and diffraction of light*. CUP Archive, New York, 1999. ISBN 9780521642224.
- [37] R. Merlin. Maxwell’s fish-eye lens and the mirage of perfect imaging. *Journal of Optics*, 13(2):024017, Jan . doi: 10.1088/2040-8978/13/2/024017. URL <http://stacks.iop.org/2040-8986/13/i=2/a=024017>.
- [38] V. N. Nguyen, S. H. Yönak, and D. R. Smith. Millimeter-wave artificial dielectric gradient index lenses. In *2009 3rd European Conference on Antennas and Propagation*, pages 1886–1890, Mar 23-27 .
- [39] I. Awai and S. Kida. Ad hoc lens antenna made of artificial dielectrics. In *2009 IEEE 13th International Symposium on Consumer Electronics, Kyoto, Japan*, pages 416–417, May 25-28 2009. doi: 10.1109/ISCE.2009.5156978.
- [40] R. Liu, Q. Cheng, J. Y. Chin, J. J. Mock, T. J. Cui, and D. R. Smith. Broadband gradient index microwave quasi-optical elements based on non-resonant metamaterials. *Opt. Express*, 17(23):21030–21041, Nov 2009. doi: 10.1364/OE.17.021030. URL <http://www.opticsexpress.org/abstract.cfm?URI=oe-17-23-21030>.
- [41] V. Nguyen, S. Larouche, N. Landy, J. S. Lee, and D. R. Smith. Quantitative comparison of gradient index and refractive lenses. *J. Opt. Soc. Am. A*, 29(11):2479–2497, Nov 2012. doi: 10.1364/JOSAA.29.002479. URL <http://josaa.osa.org/abstract.cfm?URI=josaa-29-11-2479>.
- [42] Y. Zhang, R. Mittra, and W. Hong. On the synthesis of a flat lens using a wideband low-reflection gradient-index metamaterial. *JEWA*, 25(16):2178–2187, Apr 2011. doi: 10.1163/156939311798147015. URL <http://dx.doi.org/10.1163/156939311798147015>.
- [43] Y. Zhang, R. Mittra, and W. Hong. Systematic design of planar lenses using artificial dielectrics. In *2010 IEEE Antennas and Propagation Society International Symposium, Ontario, Canada*, pages 1–4, July 11-17 2010. doi: 10.1109/APS.2010.5561790.
- [44] A. Vakil and N. Engheta. Transformation optics using graphene. *Science*, 332(6035):1291–1294, June 2011. doi: 10.1126/science.1202691. URL <http://science.sciencemag.org/content/332/6035/1291>.
- [45] S. Jain, M. Abdel-Mageed, and R. Mittra. Flat-lens design using field transformation and its comparison with those based on transformation optics and ray optics. *IEEE*

- Antenn. Wireless Propag. Lett.*, 12:777–780, June 2013. doi: DOI:10.1109/LAWP.2013.2270946. URL http://ieeexplore.ieee.org/xpls/abs_all.jsp?arnumber=6547186.
- [46] R. Yang, W. Tang, Y. Hao, and I. Youngs. A coordinate transformation-based broadband flat lens via microstrip array. *IEEE Antenn. Wireless Propag. Lett.*, 10:99–102, Feb 2011. doi: 10.1109/LAWP.2011.2112328. URL http://ieeexplore.ieee.org/xpls/abs_all.jsp?arnumber=5715850.
- [47] R. Yang, W. Tang, and Y. Hao. A broadband zone plate lens from transformation optics. *Opt. Express*, 19(13):12348–12355, June 2011. doi: 10.1364/OE.19.012348. URL <http://www.opticsexpress.org/abstract.cfm?URI=oe-19-13-12348>.
- [48] D. R. Smith, J. J. Mock, A. F. Starr, and D. Schurig. Gradient index metamaterials. *Phys. Rev. E*, 71:036609, Mar 2005. doi: 10.1103/PhysRevE.71.036609. URL <http://link.aps.org/doi/10.1103/PhysRevE.71.036609>.
- [49] D. Wilkins F. G. Smith, T. A. King. *Optics and Photonics: An Introduction*. John Wiley & Sons Ltd, West Sussex, England, second edition, 2007.
- [50] CST CST STUDIO SUITE. Computer simulation technology ag. URL <http://www.cst.com>.
- [51] M. C. Golt, S. Yarlagadda, and J.W. Gillespie. Magnetic and dielectric properties of materials consisting of oriented, iron flake filler within a thermoplastic host: Part i. material fabrication and electromagnetic characterization. *Journal of Thermoplastic Composite Materials*, 22(6):551–567, Nov 2009. doi: 10.1177/0892705709099695. URL <http://jtc.sagepub.com/content/22/6/551.abstract>.
- [52] M.C. Golt, S. Yarlagadda, and J. W. Gillespie. Magnetic and dielectric properties of materials consisting of oriented, iron flake filler within a thermoplastic host: Part ii transport model review and evaluation. *Journal of Thermoplastic Composite Materials*, 22(6):569–583, Nov 2009. doi: 10.1177/0892705709099696. URL <http://jtc.sagepub.com/content/22/6/569.abstract>.
- [53] H. F. Ma, X. Chen, H. S. Xu, X. M. Yang, W. X. Jiang, and T. J. Cui. Experiments on high-performance beam-scanning antennas made of gradient-index metamaterials. *Appl. Phys. Lett.*, 95(9):094107, Sep 2009. doi: <http://dx.doi.org/10.1063/1.3223608>. URL <http://scitation.aip.org/content/aip/journal/apl/95/9/10.1063/1.3223608>.

- [54] H. F. Ma, X. Chen, X. M. Yang, W. X. Jiang, and T. J. Cui. Design of multibeam scanning antennas with high gains and low sidelobes using gradient-index metamaterials. *J. Appl. Phys*, 107(1):014902, Jan 2010. doi: <http://dx.doi.org/10.1063/1.3275505>. URL <http://scitation.aip.org/content/aip/journal/jap/107/1/10.1063/1.3275505>.
- [55] H. Bakoglu. *Circuits, Interconnections, and Packaging for VLSI*. Addison-Wesley, New York, 1990.
- [56] A. Kabiri, Q. He, M. H. Kermani, and O. M. Ramah. Design of a controllable delay line. *Advanced Packaging, IEEE Transactions on*, 33(4):1080–1087, Nov 2010. doi: 10.1109/TADVDP.2010.2064166. URL http://ieeexplore.ieee.org/xpls/abs_all.jsp?arnumber=5549954.
- [57] R. F. Harrington. *Time-Harmonic Electromagnetic Fields*. IEEE press series on electromagnetic wave theory. J. Wiley and sons New York Chichester Weinheim, Piscataway, NJ, second edition, 2001.
- [58] J. M. Jin. *Theory and computation of electromagnetic fields*. IEEE press series. John Wiley & Sons, Hoboken, NJ, first edition, 2011.
- [59] J. H. Burge, C. Zhao, and M. B. Dubin. Use of the abbe sine condition to quantify alignment aberrations in optical imaging systems, wyoming, usa. In *International Optical Design Conference 2010, Wyoming, USA*, volume 7652, pages 765219–765219–9, Sep 2010. doi: 10.1117/12.871959. URL <http://dx.doi.org/10.1117/12.871959>.
- [60] W. M. Lee and S. H. Yun. Adaptive aberration correction of grin lenses for confocal endomicroscopy. *Opt. Lett.*, 36(23):4608–4610, Dec 2011. doi: 10.1364/OL.36.004608. URL <http://ol.osa.org/abstract.cfm?URI=ol-36-23-4608>.
- [61] F. Aieta, P. Genevet, M. Kats, and F. Capasso. Aberrations of flat lenses and aplanatic metasurfaces. *Opt. Express*, 21(25):31530–31539, Dec 2013. doi: 10.1364/OE.21.031530. URL <http://www.opticsexpress.org/abstract.cfm?URI=oe-21-25-31530>.
- [62] J. Birkenfeld, A. Castro, S. Ortiz, D. Pascual, and S. Marcos. Contribution of the gradient refractive index and shape to the crystalline lens spherical aberration and astigmatism. *Vision Research*, 86:27 – 34, Dec 2013. doi: <http://dx.doi.org/10.1016/j.visres.2013.04.004>. URL <http://www.sciencedirect.com/science/article/pii/S0042698913000953>.

- [63] P. J. Sands. Inhomogeneous lenses, ii. chromatic paraxial aberrations. *J. Opt. Soc. Am.*, 61(6):777–783, Jun 1971. doi: 10.1364/JOSA.61.000777. URL <http://www.osapublishing.org/abstract.cfm?URI=josa-61-6-777>.
- [64] U. Leonhardt. Perfect imaging without negative refraction. *New Journal of Physics*, 11(9):093040, Sep 2009. doi: 10.1088/1367-2630/11/9/093040. URL <http://stacks.iop.org/1367-2630/11/i=9/a=093040>.
- [65] I. Kitano, M. Toyama, and H. Nishi. Spherical aberration of gradient-index rod lenses. *Appl. Opt.*, 22(3):396–399, Feb 1983. doi: 10.1364/AO.22.000396. URL <http://ao.osa.org/abstract.cfm?URI=ao-22-3-396>.
- [66] E. Hecht. *Optics*. Addison Wesley. Addison Wesley, California, 2002. ISBN 0-321-18878-0.
- [67] W. Smith. *Modern Optical Engineering, 4th Ed*. McGraw Hill. McGraw- Hill Education, New York, 2007. ISBN 9780071593755.
- [68] J. Wyant. *Applied Optics and Optical Engineering, Vol. XI., Chapter 1*. Academic Press, Inc. Academic Press, Inc, New York, 1992. ISBN 0-12-408611-X.
- [69] F. G. Smith and D. Wilkins T. A. King. *Optics and Photonics: An Introduction*. Manchester physics series. Wiley, Chichester, England, 2007. ISBN 97804700 17838.
- [70] E. W. Marchand. Ray tracing in gradient-index media. *J. Opt. Soc. Am.*, 60(1):1–7, Jan 1970. doi: 10.1364/JOSA.60.000001. URL <http://www.osapublishing.org/abstract.cfm?URI=josa-60-1-1>.
- [71] T. W. Cline and R. B. Jander. Wave-front aberration measurements on grin-rod lenses. *Appl. Opt.*, 21(6):1035–1041, Mar 1982. doi: 10.1364/AO.21.001035. URL <http://ao.osa.org/abstract.cfm?URI=ao-21-6-1035>.
- [72] Miguel Ruphuy, Zhao Ren, and Omar M Ramahi. Flat far field lenses and reflectors. *PIER-M*, 34:163–170, Jan 2014. doi: 10.2528/PIERM13122607. URL <http://www.jpier.org/pierm/pier.php?paper=13122607>.
- [73] Miguel Ruphuy and Omar M. Ramahi. Analytical models for electrically thin flat lenses and reflectors. *J. Opt. Soc. Am. A*, 32(4):507–513, Apr 2015. doi: 10.1364/JOSAA.32.000507. URL <http://josaa.osa.org/abstract.cfm?URI=josaa-32-4-507>.

- [74] T. Vogt C. Homes, S. Shapiro, S.i Wakimoto, and A. Ramirez. Optical response of high-dielectric-constant perovskite-related oxide. *Science*, 293(5530):673–676, July 2001. doi: 10.1126/science.1061655. URL <http://ivanik3.narod.ru/EMagnitizm/JornalPape/Epsilon/673Homes2001.pdf>.
- [75] S. Tan, F. Yan, L. Singh, W. Cao, N. Xu, X. Hu, R. Singh, M. Wang, and W. Zhang. Terahertz metasurfaces with a high refractive index enhanced by the strong nearest neighbor coupling. *Opt. Express*, 23(22):29222–29230, Nov 2015. doi: 10.1364/OE.23.029222. URL <http://www.opticsexpress.org/abstract.cfm?URI=oe-23-22-29222>.
- [76] P. J. Sands. Inhomogeneous lenses, iv. aberrations of lenses with axial index distributions. *J. Opt. Soc. Am.*, 61(8):1086–1091, Aug 1971. doi: 10.1364/JOSA.61.001086. URL <http://www.osapublishing.org/abstract.cfm?URI=josa-61-8-1086>.
- [77] M. Ruphuy and O. M. Ramahi. Refraction in electrically-thin inhomogeneous media. *J. Opt. Soc. Am. A*, Feb 2016. doi: 10.1364/JOSAA.33.000538. URL <http://josaa.osa.org/abstract.cfm?URI=josaa-33-4-538>.
- [78] P. S. Kildal and A. Tengs. Super-stealth and how to apply it to struts and masts. In Olof Dahlsjo, editor, *Nordic Antenna Conference ANTENN94*, pages 339–346, May 31-June 2 1994.
- [79] A. Alù and N. Engheta. Cloaking a sensor. *Phys. Rev. Lett.*, 102:233901, June 2009. doi: 10.1103/PhysRevLett.102.233901. URL <http://link.aps.org/doi/10.1103/PhysRevLett.102.233901>.
- [80] R. Mittra and Y. Zhou. Application of transformation electromagnetics to cloak design and reduction of radar cross section. *Journal of Electromagnetic Engineering and Science*, 2(2), June 2013. doi: 10.5515/JKIEES.2013.13.2.73. URL <http://dx.doi.org/10.5515/JKIEES.2013.13.2.73>.
- [81] N. Stenger, M. Wilhelm, and M. Wegener. Experiments on elastic cloaking in thin plates. *Phys. Rev. Lett.*, 108:014301, Jan 2012. doi: 10.1103/PhysRevLett.108.014301. URL <http://link.aps.org/doi/10.1103/PhysRevLett.108.014301>.
- [82] Y. Lai, H. Chen, Z. Q. Zhang, and C. T. Chan. Complementary media invisibility cloak that cloaks objects at a distance outside the cloaking shell. *Phys. Rev. Lett.*, 102:093901, Mar 2009. doi: 10.1103/PhysRevLett.102.093901. URL <http://link.aps.org/doi/10.1103/PhysRevLett.102.093901>.

- [83] Y. Huang, Y. Feng, and T. Jiang. Electromagnetic cloaking by layered structure of homogeneous isotropic materials. *Opt. Express*, 15(18):11133–11141, Sep 2007. doi: 10.1364/OE.15.011133. URL <http://www.opticsexpress.org/abstract.cfm?URI=oe-15-18-11133>.
- [84] J. C. Howell, J. B. Howell, and J. S. Choi. Amplitude-only, passive, broadband, optical spatial cloaking of very large objects. *Appl. Opt.*, 53(9):1958–1963, Mar 2014. doi: 10.1364/AO.53.001958. URL <http://ao.osa.org/abstract.cfm?URI=ao-53-9-1958>.
- [85] J. S. Choi and J. C. Howell. Paraxial ray optics cloaking. *Opt. Express*, 22(24):29465–29478, Dec 2014. doi: 10.1364/OE.22.029465. URL <http://www.opticsexpress.org/abstract.cfm?URI=oe-22-24-29465>.
- [86] S. Tretyakov, P. Alitalo, O. Luukkonen, and C. Simovski. Broadband electromagnetic cloaking of long cylindrical objects. *Phys. Rev. Lett.*, 103:103905, Sep 2009. doi: 10.1103/PhysRevLett.103.103905. URL <http://link.aps.org/doi/10.1103/PhysRevLett.103.103905>.
- [87] I. I. Smolyaninov, V. N. Smolyaninova, A. V. Kildishev, and V. M. Shalaev. Anisotropic metamaterials emulated by tapered waveguides: Application to optical cloaking. *Phys. Rev. Lett.*, 102:213901, May 2009. doi: 10.1103/PhysRevLett.102.213901. URL <http://link.aps.org/doi/10.1103/PhysRevLett.102.213901>.
- [88] J. Li and J. B. Pendry. Hiding under the carpet: A new strategy for cloaking. *Phys. Rev. Lett.*, 101:203901, Nov 2008. doi: 10.1103/PhysRevLett.101.203901. URL <http://link.aps.org/doi/10.1103/PhysRevLett.101.203901>.
- [89] B. B. Oner, M. G. Can, and H. Kurt. Dual polarized broadband and all dielectric partial cloaking using stacked graded index structures. *Opt. Express*, 22(17):20457–20462, Aug 2014. doi: 10.1364/OE.22.020457. URL <http://www.opticsexpress.org/abstract.cfm?URI=oe-22-17-20457>.
- [90] B.B. Oner, M. G. Can, and H. Kurt. Broadband directional cloaking using graded index structures. In *2014 16th International Conference on Transparent Optical Networks (ICTON)*, pages 1–4, July 6-10 2014. doi: 10.1109/ICTON.2014.6876589.
- [91] Miguel Ruphuy, Omar Siddiqui, and Omar M. Ramahi. Electrically thin flat lenses and reflectors. *J. Opt. Soc. Am. A*, 32(9):1700–1706, Sep 2015. doi: 10.1364/JOSAA.32.001700. URL <http://josaa.osa.org/abstract.cfm?URI=josaa-32-9-1700>.

- [92] M. Ruphuy and O. M. Ramahi. Flat lenses for microwave applications. In *2016 IEEE International Symposium on Antennas and Propagation and USNC-URSI National Radio Science Meeting, Fajardo, Puerto Rico*, June 26 - July 1 2016.
- [93] M. Ruphuy O. M. Ramahi and Z. Ren. The design and performance of an isotropic negative-refractive-index metamaterial lens. In *2013 IEEE International Symposium on Antennas and Propagation and USNC-URSI National Radio Science Meeting, Florida, USA*, July 7-12 2013.
- [94] P. J. Sands. Inhomogeneous lenses, vi. derivatives of paraxial coefficients*. *J. Opt. Soc. Am.*, 63(10):1210–1216, Oct 1973. doi: 10.1364/JOSA.63.001210. URL <http://www.osapublishing.org/abstract.cfm?URI=josa-63-10-1210>.
- [95] T. Driscoll, D. N. Basov, A. F. Starr, P. M. Rye, S. Nemat-Nasser, D. Schurig, and D. R. Smith. Free-space microwave focusing by a negative-index gradient lens. *Appl. Phys. Lett.*, 88(8):081101, Feb 2006. doi: <http://dx.doi.org/10.1063/1.2174088>. URL <http://scitation.aip.org/content/aip/journal/apl/88/8/10.1063/1.2174088>.
- [96] S. Ilyas. and M. Gal. Gradient refractive index planar microlens in si using porous silicon. *Appl. Phys. Lett.*, 89(21):211123, Nov 2006. doi: <http://dx.doi.org/10.1063/1.2396929>. URL <http://scitation.aip.org/content/aip/journal/apl/89/21/10.1063/1.2396929>.
- [97] D. J. van Manen, J. O. A. Robertsson, and A. Curtis. Modeling of wave propagation in inhomogeneous media. *Phys. Rev. Lett.*, 94:164301, Apr 2005. doi: 10.1103/PhysRevLett.94.164301. URL <http://link.aps.org/doi/10.1103/PhysRevLett.94.164301>.
- [98] C. Dorme and M. Fink. Focusing in transmit receive mode through inhomogeneous media: The time reversal matched filter approach. *J. Acoust. Soc. Am.*, 98(2):1155–1162, Mar 1995. doi: <http://dx.doi.org/10.1121/1.413614>. URL <http://scitation.aip.org/content/asa/journal/jasa/98/2/10.1121/1.413614>.
- [99] M. Ruphuy and O. M. Ramahi. Flat lenses for microwave applications. In *2013 Mediterranean Microwave Symposium, Saida, Lebanon*, Sep 2-5 2013.

APPENDICES

Appendix A

MATLAB Script to model the Electromagnetic fields of a flat 2D lens with infinite current lines

```
\begin{verbatim}
clc
clear all

%% Based on Harrington page 223
%% currents flowing in z direction -> Az. Beta in x direction
%%%%%%%%%%%%%%%%%%%%%%%%%%%%%%%%%%%%%%%%%%%%%%%%%%%%%%%%%%%%%%%%%%%%%%%% Data %%%%%%%%%%%%%%%%%%%%%%%%%%%%%%%%%%%%%%%%%%%%%%%%%%%%%%%%%%%%%%%%%%%%%%%%%
[rd1,er] = textread('profile6Lv1.txt', '%f%f'); %er dielectric
    cte each ring (CHECK FILE)
sizer=size(er);

%%%%%%%%%%%%%%%%%%%%%%%%%%%%%%%%%%%%%%%%%%%%%%%%%%%%%%%%%%%%%%%%%%%%%%%% Constants %%%%%%%%%%%%%%%%%%%%%%%%%%%%%%%%%%%%%%%%%%%%%%%%%%%%%%%%%%%%%%%%%%%%%%%%%
J0=10/sizer(1,1);
f=10e9; u0=4*pi*10^(-7); e0=8.854187817*10^(-12);
    c0=1/sqrt(u0*e0); w=2*pi*f; k0=w/c0; lambda=c0/f;
d=lambda/10; % thickness of the lens
Layer_height=rd1(sizer(1,1))-rd1(sizer(1,1)-1);
add_space=2*Layer_height; % additional space on the top and
    bottom (added on each) of the lens to be plotted
if add_space>0 %% to automatically add a free space on the top

```

```

    and bottom of the lens (0 phase shift currents)
rdp=((rd1(sizer(1,1))+ Layer_height): Layer_height:
    (rd1(sizer(1,1))+ add_space))';
rdn=((rd1(1,1)- add_space): Layer_height: (rd1(1,1)-
    Layer_height))';
sizdrp=size(rdp);
rd1=[rdn;rd1;rdp];
erp=ones(sizdrp(1,1),1);
er=[erp;er;erp];
end
kd=w.*sqrt(er.*e0*u0); %wavenumber of each layer
rd=rd1*0.001; %radius at the center of each layer
JS=J0*exp(-j.*kd*d); %
sizer=size(er);

%%%%%%%%%% temporal angle for testing
ang=pi/2;

%%%%%%%%% Evaluation in r %%%%%%%%%%
rdel=1/25*lambda; %resolution in focal axis direction
resy=0.0005; %resolution (perpendicular to F axis)
rf=6*lambda;
r=rdel:rdel:rf; % magnitude from rdel to rf FOCAL AXIS [x]
sr=size(r);
ry=(-3*lambda-add_space*0.001):resy:(3*lambda+add_space*0.001); %
    number of evaluated points in y
sy=size(ry);

%%%%%%%%%%%%%%%%%%%%%%%%%%%%%%%%%%%%%%%%% VECTOR-Az %%%%%%%%%%%%%%%%%%%%%%%%%%%%%%%%%%%%%%%%%%
%%%%%%%%%%%%%%%%%%%%%%%%%%%%%%%%%%%%%%%%%
At=zeros(sr(1,2), sy(1,2));
for yAxisL=1:sy(1,2)

for xAxisL=1:sr(1,2)
    %% vector-Az Integration %%
for layer=1:sizer(1,1)

```

```

R(xAxisL, layer)=sqrt((r(xAxisL))^2 +(rd(layer)- ry(yAxisL))^2-
    2* (rd(layer)- ry(yAxisL))* r(xAxisL)* cos(ang));
Hv2_0(xAxisL)=besselh(0,2,k0*R(xAxisL, layer));% %% Hankel
    function%%  besselj(0,k0*R(xAxisL,
        layer))-j*bessely(0,k0*R(xAxisL, layer));
Az(xAxisL)=Hv2_0(xAxisL)*JS(layer)/(4*j);

At(xAxisL, yAxisL)=At(xAxisL, yAxisL)+ Az(xAxisL);

end

end

end

clf

%%%%%%%%%%%%%%%%%%%%%%%%%%%%%%%%%%%%%%%%%%%%%%%%%%%%%%%%%%%%%%%%%%%%%%%% VECTOR-Az ends %%%%%%%%%%%%%%%

%%%%%%%%%%%%%%%%%%%%%%%%%%%%%%%%%%%%%%%%%%%%%%%%%%%%%%%%%%%%%%%%%%%%%%%% H=curl Az %%%%%%%%%%%%%%%
for yAxisL=1:sy(1,2)
for xAxisL=1:sr(1,2)

if xAxisL~=sr(1,2)
Hy(yAxisL, xAxisL)=-(At(xAxisL,yAxisL)- At(xAxisL+1,yAxisL))/
    (r(xAxisL)- r(xAxisL+1)); %%
end
if xAxisL==sr(1,2)
Hy(yAxisL, xAxisL)=Hy(xAxisL-1);
end

end

end

%% plot H

[Y,X] = meshgrid(ry,r);
mesh(real(Hy));
axis([0.003 6 -0.120 0.120 -80 80]);

```

```

figure (1)
surf(real(Hy), 'EdgeColor', 'None');
xlabel('x')
ylabel('y')
view(2);
%%%%%%%%%%%%%%%%%%%%%%%%%%%%%%%%%%%%%%%%%%%%%%%%%%%%%%%%%%%%%%%%%%%%%%%% H=curl ends %%%%%%%%%%%%%%%%%%%%%%%%%%%%%%%%%%%%%%%%%%%%%%%%%%%%%%%%%%%%%%%%%%%%%%%%%

%%%%%%%%%%%%%%%%%%%%%%%%%%%%%%%%%%%%%%%%%%%%%%%%%%%%%%%%%%%%%%%%%%%%%%%% E field %%%%%%%%%%%%%%%%%%%%%%%%%%%%%%%%%%%%%%%%%%%%%%%%%%%%%%%%%%%%%%%%%%%%%%%%%

Ez=-j*k0^2/(w*e0)*(At); %%
[Y,X] = meshgrid(ry,r);
mesh(real(Ez));
figure (2)
surf(real(Hy), 'EdgeColor', 'None');
xlabel('x')
ylabel('y')
view(2);

\end{verbatim}

```